Experimental Aspects of Plasma Wakefields Driven in the Linear Regime



Christopher Richard Thornton

Merton College, Oxford

Thesis submitted in fulfilment of the requirements for the degree of Doctor of Philosophy at the University of Oxford supervised by Professor Simon M. Hooker & Professor Andrei Seryi

Michaelmas Term, 2016

Dedicated to those in the pursuit of knowledge.

Acknowledgements

I am sure there are almost as many written pages out there about the stress and strain of completing a DPhil as there are DPhil theses but despite all this seemingly good advice, I, like many, decided to pursue knowledge and try to understand and improve the world around me rather than following a more traditional well-paid career path. However, I would not be the researcher I am today without the support, friendship and love of so many friends and family members who I now wish to thank.

First of all I would like to thank Simon - or should that be the author wishes to thank Professor S. M. Hooker? - whose constant support throughout my DPhil has made it all possible and his attention to scientific rigour has made me the researcher I am today. I would also like to thank Simon for all the late nights and weekends on ASTRA; he was always there to the last and I still have no idea how he manages to juggle so many things at once. Perhaps such juggling is a secret kept between professors, as my co-supervisor, Andrei, is also always very busy, but has also made time for me, with encouraging words, enthusiasm and helpful advice for which I am very grateful.

Of course it is not just Simon who had the pleasure of working late

at night with me. I would like to thank Rob, Chris and Gavin for all their help while on experiments; I could not have done it without your in-put. Although I'm sure your lives would have been more fun without our time together, I would like to think that they wouldn't have been as interesting. Best of luck with writing your own theses: I hope I will be here with a beer and an ear like you were for me. I would also like to thank those who taught me all I know: James, Wolf, Laura and Nicolas and for being so patient at the start of my DPhil. I would like to thank Dave and Kevin, for their constant help and advice over tea and their warm social welcome, even if they do work on the other side of the group. I would like to mention the CLF staff, particularly all those that I came in contact with at ASTRA/Gemini, for your hard work and good humour. To my friends in the Simon room: thanks for the coffee breaks and understanding Physics chat.

Over the years I have also had a good social life in college, meeting people from all over the world. I would like to thank Diane, Gustav and Inyoung for being such great house mates in my first year and helping to make the introduction into college just that little bit more fun! Throughout the subsequent years so many people seemed to come and go but the core of Tristan, Mary, Ant, Alistair and Anne were always there for a quiet drink or less quiet party. Thanks to Charlie, Cat and Alexander for the long bike rides to make sure I didn't fare too badly with over-consumption! Thank you to Rob, Michael and Alexandra for being there in the last stretch.

Finally, my last paragraph of acknowledgements must go to my parents, Richard and Wendy, and little sister, Ellie. Thank you so much for your continued support and belief in me through my many years of study.

Abstract

This thesis describes two main pieces of experimental work and a piece of development work that aims to advance laser wakefield accelerators that use lower intensity, high repetition rate lasers. The first piece of experimental work looked at developing further the capillary discharge waveguide by changing the key parameters that form the plasma channel and measuring the electron density profile by transverse interferometry. The first change was from a capacitor discharge circuit to the Compact Marx Bank system. This achieved a reduction in electrical noise but also delivered a driving current pulse which was better matched to the plasma channel and so had less current bounce. The circuit delivered a guiding window of around 200 ns and created an electron density channel profile which supported a laser spot size of 35 µm over 15 mm. A further change was the use of helium gas rather than hydrogen gas; it was found that helium also formed an electron density profile that could support a focal spot size of 35 µm over 15 mm. Finally, the material of the capillary was changed from sapphire to diamond and whilst it was not possible to measure the plasma channel formed in this material, it was found that even after 10 000 plasma discharges there was no noticeable effect on the material, whereas sapphire under the same conditions had 0.7 µm of material ablated.

The developmental work focussed on the design of the targets to be used in laser wakefield experiments. The capillary discharge waveguide and housing were re-designed for the specific geometry of an experiment on the ASTRA-Gemini laser at the Rutherford Appleton Laboratory (RAL) and to accommodate a gas cell in the housing of the capillary discharge waveguide. It also raised questions concerning the gas density profile present in the capillary discharge waveguide and so this was modelled using OpenFOAM. It was found that the modifications had no effect on the initial gas density profile in the simulations. The combined knowledge of the OpenFOAM software and the capillary discharge waveguide for Gemini were used to create a gas cell for the multi-pulse ASTRA experiment. This gas cell maintained a flat gas density profile ideal for creating the interaction region required in this experiment. The robust design and manufacture of this target proved itself during the experiment in which it was at times taken apart daily but could always be reassembled easily.

The second experiment undertaken was the driving of a multi-pulse wakefield using the ASTRA laser at RAL. Here, a low amplitude wakefield was driven by a 55 fs duration, 2.6×10^{21} Wm^{-2} peak intensity single pulse; a train of seven pulses, 50 fs each in duration and peak intensity of 0.3×10^{21} Wm^{-2} and by two fully compressed pulses each 65 fs in duration and with a peak intensity of 1.3×10^{21} Wm^{-2}. These wakefields were measured using Frequency Domain Hologra-

phy (FDH) and Temporarily Encoded Spectral Shifting (TESS) to deduce wakefield amplitudes of 1 % variation of the plasma density. As well as driving a wakefield, the double pulse experiment suggests the possibility of energy recovery from the wakefield structure.

Thesis Outline

The work described in this thesis focuses on two main areas: the further development of a capillary discharge waveguide, probed using transverse interferometry, and the use of the ASTRA laser to generate multiple pulses for driving a laser wakefield, measured using Frequency Domain Holography.

Chapter 1 presents a general history of the accelerator, with specific details given on the history of the multi-pulse laser wakefield of particular interest in this thesis. General theory that is relevant to the rest of the thesis is then introduced.

Chapter 2 gives a detailed description of the set-up and analysis technique of transverse interferometry. This is then used to measure the effect of changing the three main elements of the capillary discharge waveguide: the gas, the driving circuit and the capillary material.

Chapter 3 details the development of the waveguide housing and how the parameters of the target were modelled, using a two-dimensional, computational fluid dynamics software called OpenFOAM before being used in the experiment. It was this knowledge that was applied to make a new target design for the gas cell used in the multiple pulse wakefield experiment.

Chapter 4 describes the set-up of the ASTRA laser to generate multiple pulses and the wakefields that are then driven using a pulse train and measured by Frequency Domain Holography.

Chapter 5 summarises the results of this thesis and potential future work is described.

Role of the Author

The transverse interferometry measurements, used to explore different elements of the capillary discharge waveguide, were performed by the author, using data analysis code that was written by the author but adapted from T. Ibbotson [1] and T. Gonsalves [2], with T. Gonsalves [2] providing the original work and theory that these measurements are based upon. The initial optical set-up was designed by W. Rittershofer but built and calibrated by the author. The theory of mode matching in a plasma channel was deduced by S. M. Hooker and applied by the author to different plasma channel shapes.

The original capillary waveguide housing was designed by A. Walker, but the re-design of the capillary waveguide housing is all the author's own work. The modelling of the initial conditions inside the capillary were undertaken by the author in OpenFOAM, but the input deck for these simulations was taken and adapted from W. Rittershofer. The design of the gas cell for use in the multi-pulse experiment is all the author's own work.

The ASTRA experiment was carried out from June 2015 to December 2015 and focussed on the generation of multiple pulses to drive a wakefield. The author had the role of target area operator and led the experiment with his colleague J. Cowley. The set-up of the probe line was designed and implemented by the author, and the pulse train

generation and assurance was done by L. Corner and R. Shalloo. The Frequency Domain Holography analysis was performed by the author alongside C. Arran who also undertook the Temporally Encoded Spectral Shifting analysis, the results of which are presented in this thesis. All figures are the author's own work, unless credited otherwise.

Thesis Output

In addition to the papers listed below, it is expected that the work of this thesis should form the basis of at least one more publication on the plasma channels formed in Helium. A further publication based on the theoretical work of TESS/FDH is in preparation.

From interferometry experiments:

A. E. Dyson, C. Thornton, and S. M. Hooker. **A compact, low cost Marx bank for generating capillary discharge plasmas**. *Review of Scientic Instruments*, pages 16, 2016. 50

From the Astra experiment:

R. J. Shalloo, L. Corner, C. Arran, J. Cowley, G. Cheung, C. Thornton, R. Walczak, and S. M. Hooker. **Generation of laser pulse trains for tests of multi-pulse laser wakeeld acceleration**, *Nuclear Instruments and Methods in Physics Research, Section A: Accelerators, Spectrometers, Detectors and Associated Equipment*, pages 13, 2015. 107, 108

J. Cowley, C. Thornton, C. Arran, R. J. Shalloo, L. Corner, G. Cheung, C.D. Gregory, S.P.D. Mangles, N. H. Matlis, D. R. Symes, R. Walczak, and S. M. Hooker. **Excitation and Control of Plasma Wakefields by Multiple Laser Pulses**, *Physical Review Letters*, pages 44802-44808, 2017. 119 (**PRL Highlighted Article)**

Contents

Contents ix

List of Figures xiv

1 Introduction 1

1.1 Accelerators 1

1.1.1 Conventional Accelerators 1

1.1.2 Plasma Accelerators 3

1.1.3 Plasma Beat Wave Accelerators 3

1.2 Basic Plasma Theory 5

1.2.1 Definition of a Plasma 5

1.2.2 Plasma Formation 5

1.2.3 Plasma Oscillation 6

1.2.4 The Ponderomotive Force 8

1.2.5 Laser Plasma Accelerators 9

1.2.6 Plasma Instabilities 10

1.3 Non-linear Effects 11

1.3.1 Non-linear Plasma Waves 11

1.3.2 Self-focussing . . . 12
1.3.3 Self-guiding . . . 13
1.4 Limitations . . . 13
1.4.1 Diffraction . . . 14
1.4.2 De-phasing . . . 14
1.4.3 Depletion . . . 15
1.4.4 Beam Loading . . . 16
1.5 Guiding Intense Laser Pulses with Waveguides . . . 16
1.5.1 Gradient Refractive Index Guiding . . . 17
1.5.2 Plasma Discharges . . . 19

2 Transverse Interferometry of Capillary Discharge Waveguides 22
2.1 Motivation . . . 22
2.2 Experimental Set-Up . . . 23
2.3 Method of Analysis . . . 31
2.3.1 Phase Retrieval Process . . . 31
2.3.1.1 Contributions to Φ_m . . . 33
2.3.2 Phase Unwrapping . . . 34
2.3.3 Overview . . . 36
2.3.4 Calculating the Electron Density Profile . . . 39
2.3.4.1 Calculating the Degree of Ionisation of the Gas . . . 40
2.3.5 Calculating the Matched Spot Size . . . 40
2.3.5.1 Curve Fitting . . . 44
2.3.6 Accounting for Errors on the Measurements . . . 46

2.4 Results . . . 47
2.4.1 Benchmark Experiments . . . 47
2.4.2 Change of Circuit Design Used to Produce Plasma Channel Experiments . . . 52
2.4.3 Change of Gas Experiments . . . 60
2.4.4 Change of Capillary Material Experiments . . . 64
2.4.4.1 Lifetime Study of Diamond . . . 66
2.5 Conclusion . . . 70

3 Target Development **72**
3.1 Introduction . . . 72
3.2 Gemini Target Design . . . 73
3.2.1 Waveguide Design . . . 74
3.2.1.1 Laser Machining of the Sapphire . . . 75
3.2.2 Waveguide Housing . . . 77
3.2.2.1 Design Considerations . . . 77
3.2.2.2 Implementation . . . 78
3.2.2.3 Experimental Improvements . . . 81
3.2.3 Alignment Technique . . . 83
3.3 OpenFOAM . . . 84
3.3.1 Introduction . . . 84
3.3.2 Simulation Parameters . . . 86
3.3.3 Geometry Parameters . . . 88
3.3.4 Results . . . 91
3.3.4.1 2014 Gemini Capillary Waveguide . . . 91

3.3.4.2 2015 ASTRA Gas Cell 92
3.3.5 Conclusion 98
3.4 ASTRA Target Design 98
3.4.1 Design Considerations 98
3.4.2 Implementation 99
3.4.3 Experimental Improvements 102

4 Measurements of Wakefields Driven by Multiple Laser Pulses 105
4.1 Motivation 105
4.2 Experimental Set-Up 106
4.2.1 ASTRA Laser 106
4.2.1.1 Methods for Measuring the Amplitude & Phase of a Pulse 112
4.2.2 Drive Beam Line 113
4.2.3 Generation of Pulse Trains 115
4.2.3.1 Multi-order Wave Plate 115
4.2.3.2 Michelson Interferometer 117
4.2.3.3 Different Operating Regimes 119
4.2.3.4 Pulse Train Characterisation 120
4.2.4 Probe Beam Line 123
4.2.5 Beam Alignment 126
4.3 Analysis Method 126
4.3.1 Commonalities of the Analysis Methods 126
4.3.2 Temporarily Encoded Spectral Shifting (TESS) 129
4.3.3 Frequency Domain Holography (FDH) 132

4.4 Results from ASTRA Experiment 135
4.4.1 Measurement of Probe and Reference GDD 135
4.4.2 Results of TESS Analysis 139
4.4.3 Results of FDH Analysis 147
4.5 Conclusion 150

5 Conclusion **152**
5.1 Summary 152
5.2 Future Improvements 155

Bibliography **158**

List of Figures

1.1 Bulk electron displacement 7

1.2 Paschen curve 21

2.1 Interferometry set up 24

2.2 Trigger network 26

2.3 Sapphire blocks arrangement 27

2.4 Lens arrangement 29

2.5 USAFT 30

2.6 Wrapped phase space 35

2.7 Key steps of the interferometry analysis 37

2.8 Matched channel mode 42

2.9 Spot size matching of channels 43

2.10 Curve fitting equations 45

2.11 Standard temporal evolution of the corrected transverse electron density profile 48

2.12 Standard temporal evolution of the deduced percentage ionisation 49

2.13 Standard temporal evolution of the matched spot size 50

2.14 Circuit diagrams of the two supply circuits 53

2.15 Change in circuit temporal evolution of the corrected transverse electron density profile 55
2.16 Change in circuit temporal evolution of the deduced percentage ionisation 56
2.17 Charge delivered by the two different discharge systems 58
2.18 Change in circuit temporal evolution of the matched spot size . . 59
2.19 Change of gas temporal evolution of the corrected transverse electron density profile 61
2.20 Change of gas, temporal evolution of the deduced percentage ionisation 62
2.21 Change of gas temporal evolution of the deduced matched spot size 63
2.22 Diamond blocks arrangement 65
2.23 Recorded fringe pattern 66
2.24 Measured surface profile before discharge 68
2.25 Measured surface profile after discharge 69

3.1 Diagonal gas slots in sapphire 74
3.2 Machining rig 76
3.3 Capillary discharge waveguide housing 79
3.4 Capillary discharge waveguide housing parts 80
3.5 Pin design 81
3.6 Knife edge reference 83
3.7 Alignment marks in sapphire 84
3.8 OpenFOAM, blockMesh of Gemini target 89
3.9 OpenFOAM, hydrogen electron number density of Gemini target . 92

3.10 OpenFOAM, blockMesh of ASTRA target 93
3.11 OpenFOAM, longitudinal density profile of ASTRA target 94
3.12 OpenFOAM, longitudinal density profile of ASTRA target with change in pinhole diameter 96
3.13 OpenFOAM, longitudinal density profile of ASTRA target with change in pinhole thickness 97
3.14 ASTRA gas cell 99
3.15 ASTRA gas cell parts 101
3.16 Improved ASTRA gas cell 102
3.17 ASTRA pinhole foils 103

4.1 Focal spot 111
4.2 ASTRA experimental layout 114
4.3 Multi-order wave plate set-up 117
4.4 Michelson interferometer set-up 118
4.5 Measurement of pulse train 121
4.6 Experimental layout of ASTRA probe beam 124
4.7 Key steps in the FDH analysis 128
4.8 Analysis map 129
4.9 Initial steps for the FDH analysis 133
4.10 Key steps in the FDH analysis 134
4.11 Modulated spectrum 137
4.12 Fit of the wavelength against separation 138
4.13 Measured single pulse wakefield 141
4.14 Measurement of pulse train 143

4.15 Measurement of double pulse wakefield 146
4.16 FDH of single pulse 147
4.17 FDH of pulse train 148
4.18 FDH of double pulse 149
4.19 FDH double pulse curves 150

Chapter 1

Introduction

1.1 Accelerators

1.1.1 Conventional Accelerators

Accelerators play a significant role in modern science and technology with over 30 000 accelerators being used daily across the world [3], in a wide variety of disciplines including biology, advanced material science, medicine, national security, industrial processing and fundamental physics [4]. All conventional accelerators involve the acceleration of a charged particle in an evacuated cavity within which an electric field is generated. The first version of an accelerator in 1855 was in the form of two plates which supported a negative electric field that could accelerate electrons supplied by a cathode element. At that time, the breakthrough came with the improvement of the vacuum pump achieved by H. Geissler [5], but it was in collaboration with J. Plucker [5] who utilised the Geissler tube to apply a magnetic field to the fluorescent glow that moved, suggesting the gas had an

electric charge, today known to be electrons. However, a change in the Geissler tube design by W. Crookes enabled J. J. Thomson [6] to give the fluorescent glow a mass and a charge. These basic accelerators went on to form the basis of the x-ray tubes that were developed by W. Röntgen [7, 8] at the end of the 19th century. In order to reach ever higher energies, new methods of accelerating particles, which avoided the electrical break down of the accelerating cavities, had to be explored. The first form of linear accelerator was developed by G. Ising [9] in the early 1920's, and used an alternating electric field in which drift spaces were placed in the accelerating cavities to shield the charged particles from the decelerating field, generated in the next half-cycle, to allow higher energies to be reached; this really began to take off in the 1950's due to advances in the production of radio frequencies. Also in the late 1920's many research scientists such as E. Lawrence, M. Livingston and S. Gaál [10] were exploring the use of cyclotrons, charged particles which travel in a circle drifting slowly outwards, rather than in a straight line. Cyclotrons were very successful and are still used today in many medical applications for the acceleration of protons. However, larger accelerating structures were required to reach ever higher energies, the cost of which became prohibitive. So a new method, was developed by V. Veksler and E. McMillan [10], called the synchrotron, in which cavities with alternating electric fields are used, much as in a linear accelerator, but where the accelerating structure forms a ring. This allows for the use of the same accelerating infrastructure to be used in multiple circuits of the ring. It was this kind of accelerator that pushed the energy frontier to TeV beams and forms the basis for machines such as Large Hadron Collider (LHC) at CERN, Switzerland.

1.1.2 Plasma Accelerators

This thesis will look at one area of ongoing research which aims to create accelerators which are smaller, cheaper and more efficient; or which have enhanced parameters such as ultrashort particle bunches [11]. This novel method, called Laser Wakefield Acceleration (LWFA), is where strong electric fields formed within laser-driven plasma waves are used to accelerate electrons [12]. The advantage of LWFA is that accelerating gradients thousands of times larger than conventional accelerator cavities can be achieved, enabling high energy gains to be made over short distances, reducing the size of the accelerator. The reason for this is that the plasma in which the particles are accelerated is no longer subject to the Kirkpatrick limit of breakdown, which is the upper experimental limit before an electrical discharge occurs inside a copper cavity. Therefore, electric accelerating fields in the order of $\mathrm{GV\,m^{-1}}$, rather than the $\mathrm{MV\,m^{-1}}$, can be supported inside the plasma. Another advantage of LWFA is that the bunch length of the particles being accelerated is short, in the region of femtoseconds, because the plasma period creating the accelerating structure is on the same time scale [13]. Thus, plasma accelerators offer the potential to provide a new tool for ultrafast science.

1.1.3 Plasma Beat Wave Accelerators

Before chirped pulse amplification lasers had become as wide spread as they are today, the method for producing plasma accelerators was to use two laser pulses, much larger than the plasma period of the wakefield (typically on the order of picoseconds), which had a difference in their frequencies ($\Delta\omega$) that matched that of the plasma frequency (ω_p) of the laser wakefield, such that $\Delta\omega = \omega_1 - \omega_2 \approx$

ω_p. This causes a plasma wave to be resonantly excited. This was proposed theoretically by Tajima *et al.* [12] and proved experimentally by Everett [14] and others [15, 16]. This is referred to as the 'plasma beat wave' method and in effect the two pulses combine to act as a series of short laser pulses, each with an amplitude of a_1 and a_2, and a duration of $\Delta\tau = 2\pi/\Delta\omega$. Each of these low amplitude but short duration pulses generate a wakefield with an amplitude of $E_{max}/E_0 = a_1 a_2/2$. If the timing separation of the pulses matches the resonant conditions, i.e. the correct plasma density, then these small pulses add together coherently to drive a plasma wave with a total amplitude, for a beat wave of length $L = N\lambda_p$, of $E_{max}/E_0 = N a_1 a_2/2$, where N refers to the number of discrete pulses in the beat wave. This technique of using two laser pulses to generate a beat wave that resonantly excite a wakefield is explored again in section 4 of this thesis. The concept is extended in order to drive a wakefield not with two pulses that create a beat wave but with two trains of discrete pulses to create a multi-pulse laser wakefield accelerator (MP-LWFA) as described by Hooker *et al.* [17]. The generation of a wakefield in this way would allow access to emerging technologies, like fibre and thin disk lasers, which can run with kilohertz repetition rates and efficiencies orders of magnitude higher than current Ti:Sapphire laser systems which are typically 0.1 % efficient and run at 10 Hz, but which produce lower energy laser pulses. This methodology also leads to a possible route of energy recovery, where a trailing pulse can be delayed such that it dampens the plasma wave driven by an earlier pulse.

1.2 Basic Plasma Theory

1.2.1 Definition of a Plasma

A plasma, often called the fourth state of matter, is a state in which the number of free electrons is approximately equal to the number of positive ions [18]. These electrons can be liberated in many ways, but the two methods of interest in this thesis are by the bombardment of other electrons achieved through electrical break down as explored in section 1.5.2 and ionisation by the laser.

1.2.2 Plasma Formation

The formation of a plasma from a laser can happen in a number of different ways but this section will focus on short pulse (fs) laser interactions with matter. The two main ionisation process of interest in this section are multi-photon ionisation and tunnelling ionisation.

An example of multi-photon ionisation is a laser interacting with a solid (e.g. section 3.2.1.1). In this process an electron is liberated from its bound state by absorbing several photons and escaping the electric field of the atom. The likelihood of this process depends on the intensity of the light, the rate (R) being given by,

$$R_n = \rho_n I^n \tag{1.1}$$

where n is the number of photons, ρ the cross-section and I the intensity of the light. Although the cross-section decreases with n, the scaling by I^n ensures that ionisation will occur. Multi-photon ionisation is seen at intensities $> 10^{10} W cm^{-2}$.

Tunnel ionisation can happen when the intensity of the light begins to become comparable to the binding strength of the electron to the atom, at around intensities $> 10^{14} W cm^{-2}$. For a short laser pulse interacting with a gas, the strong electric field of the laser pulse distorts the coulomb potential barrier of the atom, allowing electrons to tunnel the barrier with some finite probability. A detailed mathematical description of these processes is given by Gibbon [19]. If the intensity of the pulse is increased further to match that of the binding energy of the electron to the atom, then over the barrier ionisation will occur, where the coulomb potential barrier of the atom is completely suppressed by the laser pulse and the electron is able to escape spontaneously. This happens at intensities $\geq 10^{16} W cm^{-2}$.

1.2.3 Plasma Oscillation

A plasma oscillation is a collective motion of electrons in a plasma which occurs when the electrons are displaced from the positive background; it is assumed that initially the ions are stationary on the time scale of these oscillations. As a result, the plasma is no longer locally neutral and electric fields are formed in the plasma. The electrons move in this field to counter the positive charge density. The electrons tend to overshoot their resting place and oscillate, with the result that the charge density is described by a simple harmonic motion, which has a frequency called the Langmuir frequency or plasma frequency ω_p.

To derive ω_p it is necessary to imagine a body of electrons displaced by some distance X, as shown in figure 1.1. This sets up an electric potential, which is governed by Gauss's law 1.2,

$$\bigtriangledown \cdot E = \frac{\rho}{\epsilon_0} \tag{1.2}$$

where $\bigtriangledown \cdot E$ is the divergence of the electric field, ρ is the total electric charge density and ϵ_0 is the electric constant. The force can be considered as only acting in 1D and so the equation can be simplified to the planar case 1.3. Assuming no initial electric field this becomes,

$$\frac{dE_x}{dx} = \frac{\rho}{\epsilon_0} \tag{1.3}$$

$$E_x - E_x(0) = \frac{1}{\epsilon_0}\int_0^X \rho(x')dx' = \frac{e}{\epsilon_0} n_e X \tag{1.4}$$

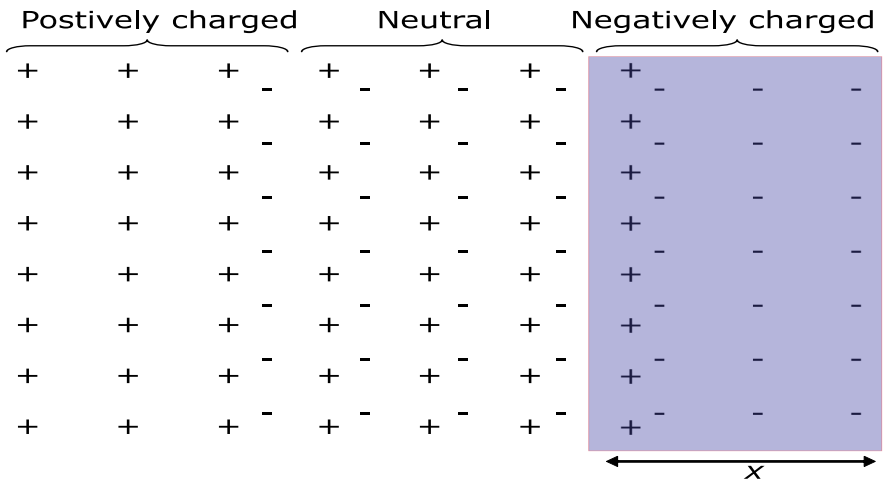


Figure 1.1: Schematic diagram showing the local displacement of electrons in a bulk plasma.

where E_x is the electric field in the direction of displacement, $E_x(0)$ is the initial electric field, e is the charge of the electron and n_e is the plasma electron density. It is now possible to use Newton's Second Law of motion to find the displacement of this charge density. It is assumed in this case that no damping of the electrons motion occurs. Assuming some external force F on the electrons and the electrons to have a mass m_e, Newton's Second Law of motion can be written as,

$$F = m_e \frac{d^2X}{dt^2} = -eE = -\frac{e^2 n_e}{\epsilon_0} X \tag{1.5}$$

$$\frac{d^2X}{dt^2} + \frac{e^2 n_e}{\epsilon_0 m_e} X = 0 \tag{1.6}$$

Solving this second-order linear differential equation,

$$F = cos(\omega_p^2 X) \tag{1.7}$$

where,

$$\omega_p = \sqrt{\frac{e^2 n_e}{\epsilon_0 m_e}} \tag{1.8}$$

it is seen that the force acting on the electrons is periodic, which is the plasma frequency ω_p.

1.2.4 The Ponderomotive Force

In these experiments the plasma wave described above is driven by the electric field of a high intensity laser by a force referred to as the ponderomotive force.

When a laser interacts with a plasma it causes the electrons in the plasma to be displaced from the nuclei; the electrons then oscillate around their former position at the frequency ω_p described in section 1.2.3. A full derivation of the pondermotive force was shown by Esarey *et al.* [13] but only the key result is shown,

$$F_p = -\frac{1}{2} m_e c^2 \nabla a^2 \tag{1.9}$$

where m_e is the electron mass and a the normalised vector potential $a = eA/m_e c$ of the laser electric field. This force is a manifestation of the Lorentz force experienced by a particle interacting with a *non-uniform* electric field; it can be seen that the ponderomotive force expels electrons from regions of high gradients in the laser intensity, forming the plasma wave in its wake.

1.2.5 Laser Plasma Accelerators

Laser plasma accelerators exploit the region behind the laser pulses, which has a large electric field caused by the expulsion of the electrons, and effectively forms an accelerating cavity. By considering the momentum of the electrons $p_x(t) = F\Delta t \times cos(\omega_p t)$ caused by the pondermotive force F the strength of the electric field can be written as,

$$E_x = -\frac{1}{e}\frac{dp_x}{dt} = -\frac{m_e c}{2e} a_0^2 \omega_p sin(\omega_p t) \tag{1.10}$$

this is for the limit of the linear wakefield, where a square pulse has been used to drive the wakefield and the electric field is calculated in the direction of the

propagating laser. Dawson in 1995 [20] considered the limitation of this equation when the electric fluid velocity of the plasma approaches the velocity of the plasma wave, referred to as the cold non-relativistic wave-breaking field, and is defined as,

$$E_0^{WB} = \frac{m_e c \omega_p}{2e} \simeq 0.1\sqrt{n_e[m^{-3}]} \tag{1.11}$$

which means that for a typical plasma density of 1×10^{24} m^{-3}, fields of 100 GV m^{-1} can be created to accelerate negatively charged particles.

1.2.6 Plasma Instabilities

In the basic model of a plasma wakefield acceleration, described in section 1.2.5, the motion of the ions in the plasma are ignored. This holds true for most short pulse (fs) laser plasma interactions. However, for plasma beat wave acceleration a more careful examination of the subject needs to be undertaken. A particular instability of concern is the modulation instability caused by energy being transferred from the amplitude envelope of the laser pulse to the ions. This provides an effective way to pass energy to the ions via a higher frequency wave which would normally not have an effect. This causes the electric field of the wakefield to become modulated as the ions move to cancel out the electric field potential. A full mathematical description of this process is given in Chen [21].

According to Mora [22] *et al.* this happens to be the case when the intensity of the laser field is below 10^{16} Wcm^{-2}, this is not the case for the experiments described in chapter 4. However, this may be an important consideration if a longer pulse train than explored in this thesis was to be used.

1.3 Non-linear Effects

The refractive index of the plasma varies with the intensity of the laser pulse. This causes non-linear effects on the laser pulse which have an effect on the laser wakefield generated.

1.3.1 Non-linear Plasma Waves

The interaction of a laser pulse with a plasma is conveniently described by the normalised vector potential $a_0 = e\mathbf{A}/m_e c^2$, where $\mathbf{A}$ is the peak value of the vector potential of the pulse. A convenient 'engineering' formula is [13],

$$a_0^2 \backsimeq 7.3 \times 10^{-19} [\lambda(\mu\mathrm{m})]^2 I_0(\mathrm{Wcm}^{-2}) \tag{1.12}$$

where the laser wavelength, expressed in micrometers, is λ and I_0 is the laser intensity in units of $\mathrm{W/cm}^{-2}$. When $a_0 \leq 1$, a linear wake is driven. In this regime the plasma wakefield is sinusoidal, with an amplitude which increases linearly with the laser intensity. When $a_0 > 1$ then a quasi-linear wake is driven, in which the front of the sine wave begins to tilt forward and the field develops a saw-tooth profile. Finally, if the a_0 is increased to $a_0 > 4$, and the spot is tightly focussed to tens of micron, then the bubble regime is reached [23]; in this regime all the plasma electrons are expelled from a near-spherical region immediately behind the laser pulse.

There are many advantages and disadvantages to the different regimes. The bubble regime has the advantage of it being possible to inject electrons by self-trapping, a process in which electrons fall backwards around the bubble cavity

and gain enough momentum to become trapped and accelerated. In other regimes this is not possible as the electrons do not gain enough momentum to become trapped inside the wakefield structure and so a separate injection method has to be used. However, the energy spread of the electrons tends to be large as electrons are continually injected into the wake. Another advantage of the bubble regime is that the electric field inside the bubble is very high and so electrons can be accelerated to high energies over smaller distances than in the linear regime. This work, however, is concerned with the driving of linear or quasi-linear wakes as these require a lower peak laser power, avoid unwanted self-injection and provide an accelerating structure that has phases which can accelerate positive and negative particles.

1.3.2 Self-focussing

In a non-linear plasma wave, diffraction is often countered by refraction when the power of the laser is above a self-focussing threshold. Consider the refractive index of a plasma given by,

$$\eta \backsimeq 1 - \frac{n_e e^2}{2\gamma m_e \epsilon_0 \omega_0^2} \tag{1.13}$$

where n_e is the electron density, ω_0 is the angular frequency of the laser and $\gamma = \frac{1}{\sqrt{1-\frac{v^2}{c^2}}}$ is the relativistic factor of the electrons oscillating in the laser field at a relative velocity v. For a laser beam peaked on-axis the transverse variation of the γ value causes the refractive index to be largest on-axis; this is exactly what is required to guide the laser pulse, see section 1.5.1. Hence this so-called relativistic self-focussing can extend the laser-plasma interaction length beyond the Rayleigh

range, the distance from which the minimum beam radius has increased by the square root of two. The laser power to just balance diffraction is required to be above a critical laser power P_c [24] expressed by equation 1.14,

$$P_c = 17.4 \frac{\omega_0^2}{\omega_p^2} \ [GW] \tag{1.14}$$

1.3.3 Self-guiding

The self-focussing of a laser pulse as shown in equation 1.13 is valid in cases where the pulses are longer than the plasma period. For 'short' femtosecond pulses, the change in the refractive index of the plasma, due to the electron density n_e, is counteracted by the effect on the refractive index change, due to the relativistic mass increase γ of the electrons; this can be seen in equation 1.13. This means that the leading edge of the laser pulse diffracts freely, when not guided by an external structure. However, Lu *et al.* [25] defined a new regime called self-guiding where more laser energy is transferred into the wakefield than is lost to the diffraction of the leading edge of the laser pulse. The equation 1.15 is defined in terms of the critical laser power and shows that self-guiding requires a higher peak power than the self-focussing regime,

$$P_c^{diff} = \frac{1}{8} \frac{\omega_0}{\omega_p}^{\frac{6}{5}} P_c \tag{1.15}$$

1.4 Limitations

There are three major limitations to the distance over which acceleration may be maintained by a plasma wakefield that affect the final electron energy: diffraction

of the laser pulse; depletion of the laser pulse; and the de-phasing of the electron bunch with the laser pulse. Some of these effects, such as diffraction, can be partly mitigated by waveguiding methods, as explored in section 1.5. As well as a limit to the energy of the electrons produced, there is an upper limit to the bunch charge that can be sustained by the accelerating structure, referred to as beam loading.

1.4.1 Diffraction

The use of high laser intensities to drive laser wakefields is achieved by having very tight focal spots ~ 20 µm. This spot size W_0 (defined as the radius at which the laser intensity falls to $1/e^2$ of its value on-axis) can only be maintained over a short Rayleigh Range, which is the distance where the spot size has increased by a square root of two; and is a convenient measure of the distance over which the wakefield amplitude will be significant. For a Gaussian beam the Rayleigh length is given by,

$$Z_R = \frac{\pi W_0^2}{\lambda} \tag{1.16}$$

where W_0 is the Gaussian beam diameter. This interaction length can be increased by using self-guiding or optical guiding techniques as will be explored in section 1.5.

1.4.2 De-phasing

The plasma wave propagates at the group velocity $v_g = \eta c < c$ of the laser pulse, which is less than c, whereas the electrons are accelerated to velocities

which closely approach c. As a consequence, the accelerated electrons overtake the plasma wave and after some distance, known as the de-phasing length L_d, move from a region of acceleration to deceleration. The difference in velocity ΔV of the electrons and the laser can be expressed as,

$$\Delta V = c - c\sqrt{1 - \frac{\omega_p^2}{\omega_0^2}} \approx \frac{c\omega_p^2}{2\omega_0} \tag{1.17}$$

where ω_p is the plasma frequency and ω_0 is the angular frequency of the laser pulse. The electron bunch is accelerated in the $\lambda_p/2$ of a linear plasma wave and so the time spent in the accelerating region before running into the decelerating part of the plasma wave is defined as,

$$t_d = \frac{\lambda_p/2}{\Delta V} \tag{1.18}$$

by considering this in terms of a distance, the de-phasing length L_d can be found,

$$L_d = ct_d = \frac{c\lambda_p/2}{\Delta V} = \frac{\lambda_p^3}{\lambda_0^2}. \tag{1.19}$$

1.4.3 Depletion

Excitation of the plasma wave removes energy from the laser pulse, leading to depletion of the pulse energy in a characteristic distance L_{pd}, a point where the laser pulse loses one-half of its initial energy to a plasma wave. Gordon *et al.* [26] derive an expression in terms of a de-phasing length of a linear wakefield,

$$L_{pd} = \frac{L_d}{2a_0^2} \tag{1.20}$$

where L_{pd} stands for pump depletion. Esarey *et al.* [13] have derived equations for the depletion length of many different wakefield regimes; these will however not be explored here.

1.4.4 Beam Loading

The electric field of the trapped electrons in the wakefield, has an effect on the accelerating electric field of the plasma wave, causing it to become weaker. Katsouleas *et al.* [27] put a limit on the number of electrons that can be accelerated in a linear wakefield as,

$$N_{max} = 5 \times 10^5 \frac{E_z}{E_0} A\sqrt{n_e} \tag{1.21}$$

where A is the cross sectional area of the electron bunch in cm^2, n_e is in cm^{-3} and $\frac{E_z}{E_0}$ is the normalised axial electric field.

1.5 Guiding Intense Laser Pulses with Waveguides

The limitations of diffraction can potentially be overcome by using a waveguide. This structure allows for the maintenance of high intensity over distances longer than the Rayleigh range and thus allows the acceleration of electrons up to an order of magnitude higher in energy for the same laser parameters. Several techniques have been explored to guide laser pulses. A detailed summary of waveguides is available in [2] but here follows a brief overview of the gradi-

ent refractive index method of guiding before describing in detail the capillary discharge waveguide and the basics of plasma discharge.

1.5.1 Gradient Refractive Index Guiding

In a gradient refractive index fibre (GRIN), the refractive index decreases with distance from the axis of the fibre. This means that the fibre continually counteracts a diffracting laser, by causing the wavefronts to bend inward due to the slower phase velocity on-axis, guiding many times the original Rayleigh range. Clearly, solid materials could not withstand the high laser intensities needed to guide 1×10^{21} Wm^{-2}. However, by forming a plasma that has a slowly varying density gradient where the plasma density is lower at the centre of the laser axis, the refractive index increases with distance from the centre of the channel axis. This forms a GRIN capable of guiding a high intensity laser pulse [28].

The form of the plasma channel required to guide a Gaussian laser pulse is,

$$\Delta n_e = \frac{1}{\pi r_e r_{ch}^2} \tag{1.22}$$

where Δn_e is the increase in electron density above the axial value at a radial distance $r = r_{ch}$, r_{ch} is the radius of the channel and r_e is the classic electron radius (2.82×10^{-15} m). This equation is for a parabolic channel; work later in this thesis, in section 2.3.5.1, considers non-parabolic channels.

The plasma channels can be created in a number of different ways:

Laser Produced Plasma Channels: uses more than one laser pulse to separate

plasma formation from plasma heating and forms a channel. This methodology was first explored by Dunfee *et al.* [29] in 1995 and Volfbeyn *et al.* [30] in 1999 with Geddes *et al.* [31] adopting an igniter heater approach in 2004.

The Discharge Ablated Capillary: this method involves a current of approximately 200 A and 500 ns being pulsed through an acrylic resin 2 cm long capillary, with 500 µm diameter, so that the walls of the capillary ablates to form the plasma channel when trigged by a separate 40 mJ laser. In 2008, Kameshima *et al.* [32] used this technique to demonstrate electron acceleration above 0.3 GeV with a laser pulse of 1 J and a pulse length of 26 fs. In a channel that had a minimum on axis density of 1×10^{24} m^{-3} and radius of 500 µm.

Fast Discharge Gas Cell: in 2008 Bendoyro *et al.* [33] used a structured gas cell, which has a sequence of 250 µm thick alumina plates with 300 µm diameter holes located on the laser axis, to create a defined path for the plasma discharge. A plasma is ignited through these dielectric plates by two hollow, conical electrodes located at either end of the gas cell. Related to the hydrodynamic expansion channel invented by H. M. Milchberg [29], it is 'fast' because the current pulse is short compared to the plasma expansion time. More recently at the ASTRA-Gemini laser facility, N. Lopez [34] led a group using this methodology to produce electron beams of 400-700 MeV, from a 40 mm gas cell, and observed energy gains of up to 2 GeV.

The Capillary Discharge Waveguide: was developed by the Oxford group [35] in 2001. In this device, a capillary tube of diameter 200 to 400 µm, is filled with hydrogen gas, which, when broken down into a plasma by an electrical discharge, forms a plasma confined within a structure. A slowly varying density gradient is produced as the hot dense plasma on-axis expands outwards and is

cooled on the walls of the confining structure. This causes a smooth density gradient to be formed where the plasma density is lower at the centre of the structure than at the walls, generating a refractive index that increases with distance from the plasma channel axis. This forms a GRIN capable of guiding a high intensity laser pulse [28]. By carefully matching the density profile of the gas-filled capillary discharge waveguide to the high intensity laser spot size, the problem of diffraction is eliminated over the guiding length of the capillary as has been successfully shown by Butler *et al.* [36]. Later, this waveguide method was used to extend the acceleration length of a laser wakefield generating 1 GeV electron beams. In 2007, Gonsalves *et al.* [37] published scaling laws of the axial plasma electron density and the matched spot size of the plasma channel calculated by interferometric measurements. Further measurements in this thesis in section 2.4.1 show how the matched spot size changes during the discharge pulse.

1.5.2 Plasma Discharges

The Oxford capillary discharge waveguide relies on an electrical discharge to form the plasma channel, and so it is useful, very briefly, to outline the physics of high voltage direct current discharges; further information on the subject can be found in Fridman *et al* [38]. When a high voltage is applied to a pair of parallel electrodes in a gas, free electrons present in the gas created with ionising radiation (from for example cosmic rays) are accelerated towards the anode. In doing so, the electrons can strike other neutral particles and if sufficiently energetic liberate additional electrons, causing an exponential increase of electrons which

is described as the avalanche effect [38]. The required breakdown voltage V_b is expressed by [38],

$$V_b = \frac{B(pd)}{\ln(pdA) - \ln[\ln(1+\gamma^{-1})]} \tag{1.23}$$

which gives the combination of gas pressure (p) and electrode separation (d) that is required for an electrical breakdown to occur. A plot of V_b against pd is shown in figure 1.2, referred to as the Paschen curve. It can be seen that for high values of pd, the breakdown voltage increases; this corresponds to collisions happening between electrons and neutral particles to soon for the electrons to have gained sufficient energy to liberate a second electron from a neutral particle. The breakdown voltage also increases for low values of pd; this behaviour arises because electrons may collide with the anode before colliding with another particle to create secondary electrons.

Equation 1.23 only holds true for breakdowns between two infinite planar electrodes, in contrast to a plasma formed in a capillary discharge, where the two electrodes are constrained by the narrow capillary between them. The capillary has the added effect of changing the initial break down in the plasma as a surface current runs along the wall of the capillary. Intuitively it is tempting to think this would lower the required voltage break down however this is not the case. The finite diameter of the capillary means that the break down voltage of the discharge is above what would be predicted by the Paschen curve because electrons collide with the capillary wall, rather than generating secondary electrons. This effect dominates far above any advantage of the wall effects and stifles the avalanche

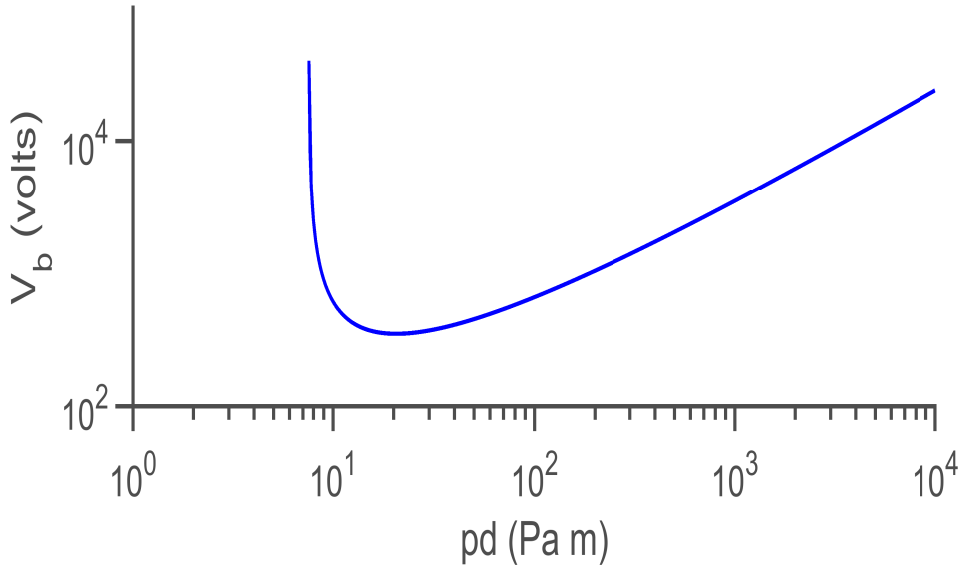


Figure 1.2: Paschen's curve of hydrogen, giving the breakdown voltage V_b as a function of pressure and electrode separation pd. Where the values of A & B are taken to be 7 $\mathrm{Pa^{-1}\,m^{-1}}$ and 173 $\mathrm{V\,Pa^{-1}\,m^{-1}}$ respectively [38].

process meaning a break down voltage increase of approximately a factor of 10 times than that given by the theory is required to achieve a plasma break down in a capillary.

Chapter 2

Transverse Interferometry of Capillary Discharge Waveguides

2.1 Motivation

Guiding high-intensity laser beams in plasma channels is a well-established method of overcoming the depletion and diffraction limits of laser driven plasma accelerators [36, 39, 40]. In a plasma channel, the laser pulse is guided by a transverse electron density profile and the shape of this profile determines the behaviour of the guiding.

Previous work has explored how the diameter of the capillary and the initial hydrogen density impact the on-axis electron density and the laser spot size that can be supported by the guiding channel. In this chapter, the results of further work are presented. The aim of this work was to compare the plasma channels produced by two different driving circuits; examine the effect of changing the gas

from hydrogen to helium and to alter the material plates that the capillaries were made from to observe the effect on the density profile and thus the guiding of the laser pulse.

2.2 Experimental Set-Up

A Mach-Zehnder interferometer was chosen for this study because it is easy to set up, has a large working space and has the advantage that the probe beam only passes through the sample once. The general layout is shown in figure 2.1. The plasma channel was probed by laser pulses from a small Nd:YAG laser (Continuum Minilite). This provided pulses of approximately 5-7 ns duration, at a wavelength of 1064 nm, and an energy of up to 28 mJ. For this work the pulse energy was reduced to approximately 2-4 mJ using an adjustable attenuator located within the laser housing. A portion of the 1064 nm radiation was frequency doubled using a Potassium Dideuterium Phosphate (KDP) crystal to generate a second co-propagating beam of wavelength 532 nm.

These two beams of different wavelengths were separated to create independent interferograms of the plasma channel, that could be compared and used to account for heating of the plates over the duration of the discharge pulse. During the initial plasma channel development ($\sim$ 50 ns) this is not a problem, but as the plasma channel develops, the energy in the plasma dissipates into the plates causing a thermal expansion of the material; this changes the refractive index and therefore the path difference of the reference and sample.

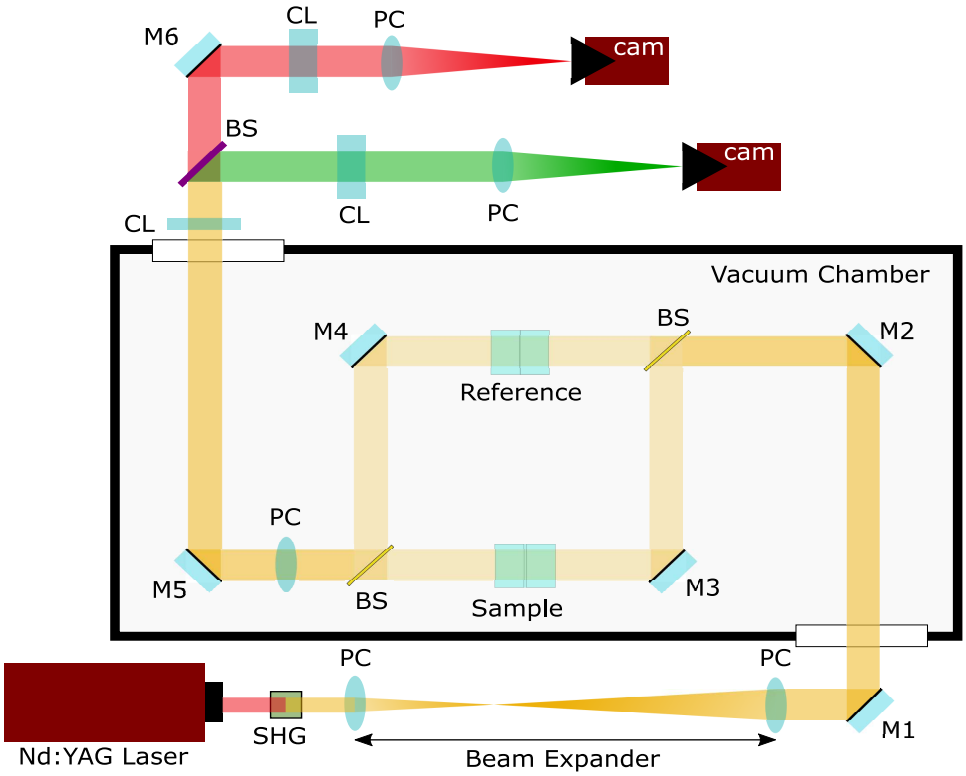


Figure 2.1: Schematic diagram of the interferometry experiment. Here, BS is the beam splitter; M# represent mirrors with nominally total reflection; SHG is the second harmonic generating crystal, PC are the plano-convex lenses and CL are the cylindrical lenses. The red line represents the 1064 nm light; the green line the 532 nm light and the yellow line the common path of both the 1064 nm & 532 nm. Also shown are the reference and sample plates.

During the day-to-day optimisation of optical alignment, the laser was run at 10 Hz. When generating data, however, the flash lamps were kept running at 10 Hz to provide thermal stability for the system and an external trigger was used to trigger the Q-switch of the laser to provide a single laser pulse output. The relative timing delay between the plasma channel formation and laser probe provided time 'slices' of the plasma channel development. This was achieved with a number of digital delay generators (Stanford 4 channel DG535) and logic gates as shown in figure 2.2. Delay box A was used to supply a 2-second trigger to open a gas valve, which produced a uniform gas density profile. After this a 100 ms transistor-transistor logic (TTL) signal was sent to a gated switch. This switch was linked up with the internal clock of the laser that maintained the flash lamps at 10 Hz and gave out 50 ms triggers from the back laser panel marked F/L. Once triggered by delay box A at the falling edge of the flash lamp signal, the gated switch triggered the external trigger on the front of the laser panel and delay boxes B & C. Delay box B then sent 100 µs TTL triggers to the cameras. Delay box C sent a 20 µs TTL signal to the discharge unit, with relative timing between the laser and the discharge being altered by using the delay on delay box C. Finally, delay box C triggered the Q-switch of the laser.

The probe laser beam was expanded to 30 mm from its original diameter of 3 mm by a Keplarian telescope and directed through a 100 mm fused silica window into a vacuum chamber. Each of the two probe beams was split by a 50:50 thin-film pellicle (Thorlabs BP233) to form the probe and reference arms of the interferometer. The reference arm of the interferometer was sent through two plates, with the same material thickness as the plates used to form the capillary in the probe

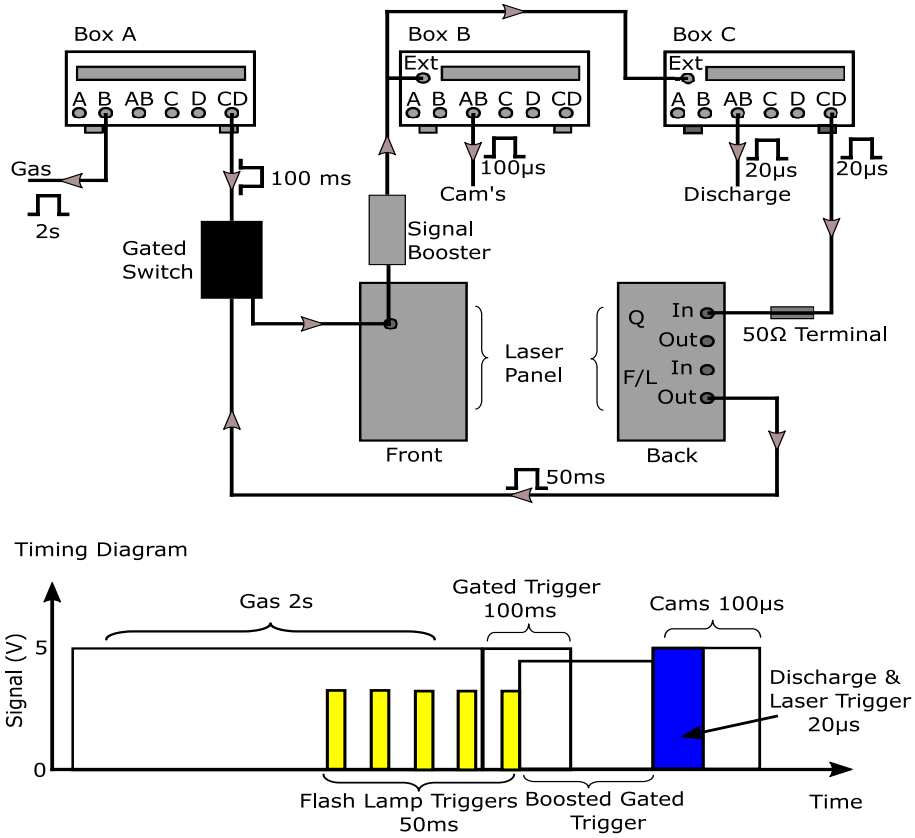


Figure 2.2: Schematic diagram of the trigger network (Top) and timing diagram of the trigger network (Bottom). Box A acts as the master control unit and sets off the other triggers. The gated switch means that Box B and C are in time with the laser flash lamps. Box C can be used to control the time between the discharge and the probe laser and thus by altering the timing can be used to measure different time 'slices' of the plasma channel development.

arm of the interferometer. The two arms of the Mach-Zehnder interferometer were then recombined on a second thin-film pellicle (Thorlabs BP233).

In the work described here, the channel in a capillary discharge waveguide was usually laser machined into two sapphire blocks which were glued together to form a single channel. The plasma is then formed by applying a large potential differ-

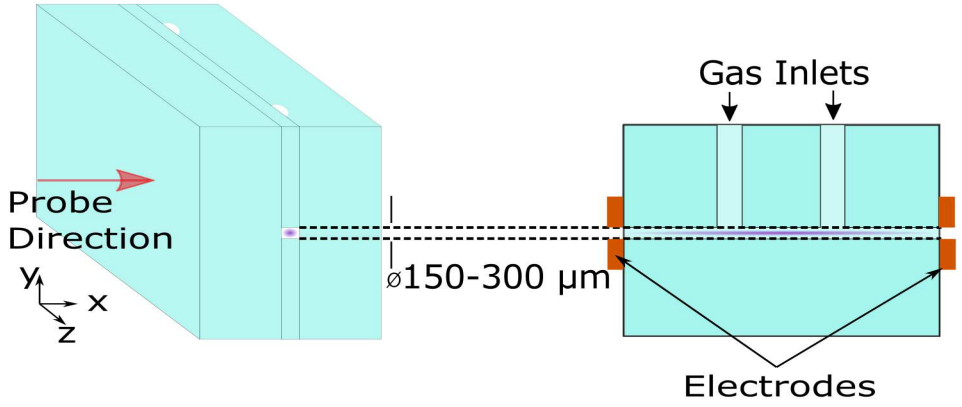


Figure 2.3: Construction of a plasma channel using sapphire blocks and spacer plates. A copper wire of varying diameters from 200 to 300 µm was used to set the correct spacing of the channel.

ence across this channel, provided by two electrodes at either end, which causes an electrical breakdown of the gas contained within the capillary, as described in section 1.5.2. However, when performing interferometric measurements, a transverse optical path through the plasma channel is required. This is not normally possible with channels that have been machined into sapphire blocks as the finish is opaque and therefore scatters the probe light. To circumvent this, square cross-section capillaries of size 200 µm, 250 µm & 300 µm were created.

This was achieved by using two polished sapphire blocks of dimensions 20 mm by 15 mm by 4 mm and two sapphire spacer plates of 20 mm by 15 mm, with a varying thickness that was used to control the size of the capillary channel being formed. This is diagrammatically shown in figure 2.3. The spacer plates were separated by a copper wire with a diameter equal to 200 µm, 250 µm & 300 µm, depending on the capillary channel being formed. This could then be removed to

ensure that the size of the channel that was being created was correct. Broks *et al.* [41] found that the plasma channels formed in square capillaries are similar to those formed in capillaries of circular cross-sections.

Two sapphire blocks made of two 20 mm by 15 mm by 4 mm thick plates, held together by compression, were placed in the reference beam to compensate for the phase shift introduced by the sapphire blocks forming the capillary channel. This ensured any extra phase picked up by the probe beam was mainly the contribution from the formation of a plasma channel.

The sapphire blocks that form the capillary channel are etched by the hot plasma which roughens the inner walls after several shots and makes imagining the channel impossible, limiting the number of shots for which interferometry can be performed. The use of c-cut sapphire, as described in Ibbotson's [1] thesis, reduces the rate of this plasma etching on the polished sapphire surface and enabled ten times more data to be collected with the same set of sapphire blocks.

The probe laser beam was collimated using a plano-convex $f = 300$ mm lens. The lens was positioned with its front focal plane coincident with the plasma channel. The beam was then expanded by a pair of cylindrical lenses focussing in the horizontal plane of the beam to magnify the image vertically, giving greater resolution of the plasma channel. A diagrammatic set-up is shown in figure 2.4. This acted as a telescope to magnify the image in the vertical plane. The focal length of the lenses used were $+500$ mm and -100 mm. This gave a theoretical magnification ratio of 1:5. To confirm this, a United States Air Resolution Grid

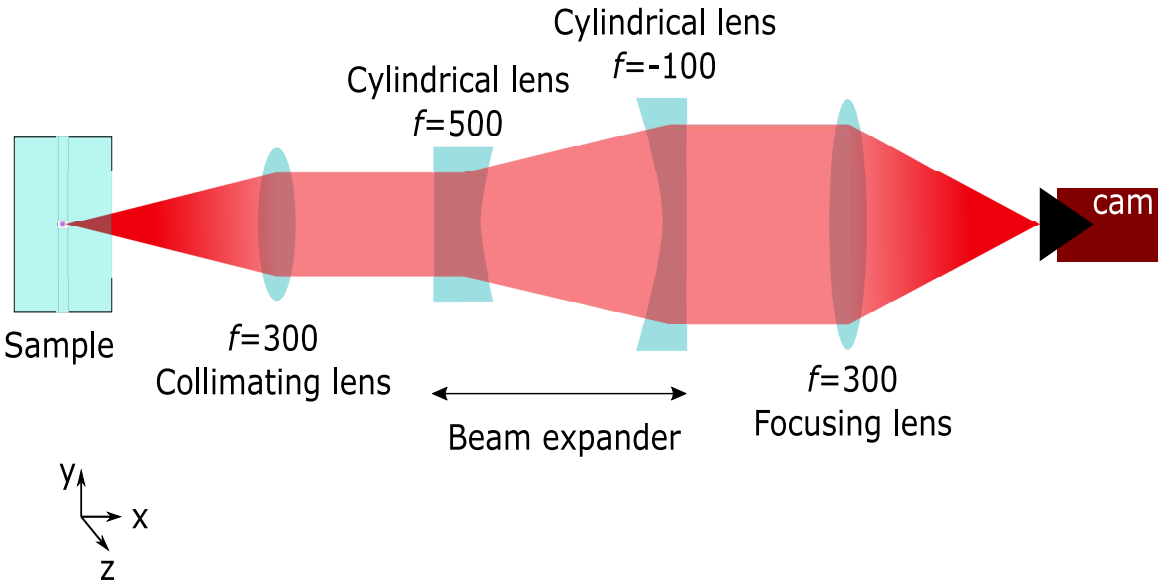
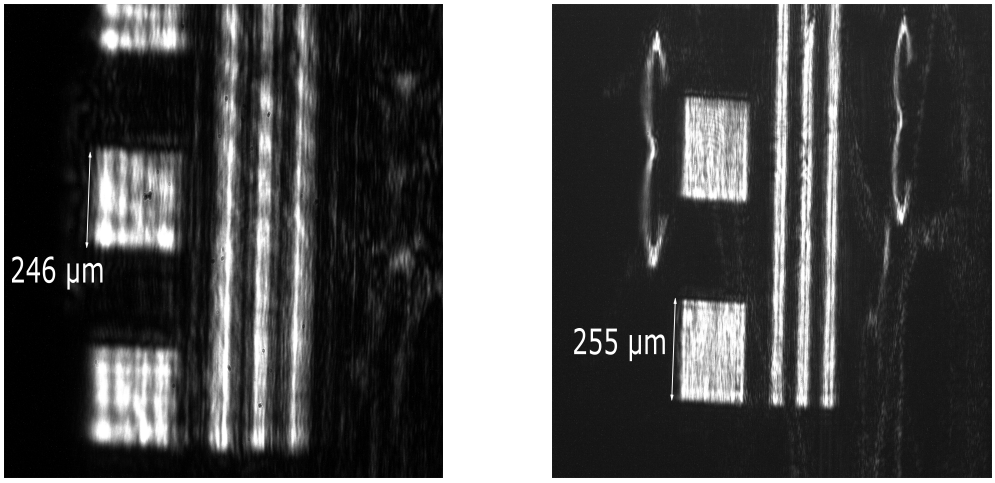


Figure 2.4: Schematic diagram of the lens arrangement, viewed from the horizontal plane. The light from the sample is collimated. The collimated light is then expanded to achieve the correct magnification of the image. The image is then formed on a camera using the focusing lens.

1951 (USAFT1951) was used, as shown in figure 2.5. By measuring the size of a feature on the resolution grid, the magnification of the lens system was determined. It was found that the actual magnification ratio was approximately 1:4.5

Figure 2.5 shows a shear on the image, this is because the resolution grid is not level to the probe beam. This could be corrected by adjusting the tilt of resolution grid until the shear is removed from the image, although this was difficult to achieve in this case as the resolution grid was confined inside the sapphire holder making its manipulation difficult. The blurring in figure 2.5a, is caused by the image being out of focus. This is because the collimating lens was adjusted to achieve the best collimation for 532 nm wavelength light and so some chromatic



(a) (b)

Figure 2.5: Images of the USAFT used to calibrate the imaging system. 2.5a shows the AFT illuminated by the 1064 nm wavelength and 2.5b shows the 532 nm wavelength illumination.

aberration is present in the 1064 nm image. Both images in figure 2.5 show some structure, this is caused by structure in the probe beam.

The two probe wavelengths were separated by a two-inch dichroic beam splitter (Thorlabs DMLP950L), and each wavelength was then refocused by a $f = 300$ mm plano-convex lens onto the active area of a charge-coupled camera. The cameras used were 12-bit CMOS sensors, with a resolution of 2592×1944 pixels. A filter was placed between the lens and the camera to ensure that each camera detected only one of the two probe beams.

For each time 'slice', a 'data' interferogram at some time delay t after the onset of the discharge; and a reference' interferogram with no discharge or gas were recorded.

2.3 Method of Analysis

A method of analysis for extraction of the phases from an interferogram was developed by Takeda *et al.* [42]. This was later adapted by Gonsalves [2] to apply specifically to gas-filled capillary discharge waveguides used in LWFA. There follows a brief outline of the two key pieces of theory that were used to convert the raw data from these experiments into plasma density measurements.

2.3.1 Phase Retrieval Process

A probe beam that travels through the plasma channel will pick up an additional phase contribution given by the refractive index of the plasma. This additional phase is encoded into the interference pattern that was recorded. This interference pattern intensity is represented by,

$$i(y,z) = a(y,z) + b(y,z)cos[2\pi f_0 z + \Phi_m(y,z)] \tag{2.1}$$

where $a(y,z)$ represents background noise attributed mainly to the imaging optics, $b(y,z)$ represents the varying fringe intensity, f_0 is the spatial frequency of the fringe pattern and Φ_m represents the measured phase shift. The co-ordinate system is shown in figure 2.3.

When there is no plasma channel, Φ_m becomes zero and the recorded fringes should be straight and uniformly spaced. However, as a plasma channel develops, an extra phase contribution is added and Φ_m begins to play a role, causing a bending of the fringe pattern; this varies across the capillary diameter and shows a spatial development of the plasma channel.

The measured phase component Φ_m of this equation can be retrieved using the Takeda [42] method. A brief outline of this follows. Initially, the fringe pattern recorded was converted into Fourier space using a 2D fast-Fourier transform algorithm. To do this, equation 2.1 was re-written in complex exponential form,

$$i(y,z) = a(y,z) + c(y,z)\exp^{2\pi i f_0 z} + c^*(y,z)\exp^{-2\pi i f_0 z} \tag{2.2}$$

where $c(y,z)$ is,

$$c(y,z) = \frac{1}{2}b(y,z)\exp^{i\Phi_m(y,z)} \tag{2.3}$$

taking the 2D Fourier transform gives,

$$I(f_y,f_z) = \underbrace{A(f_y,f_z)}_{\text{DC term}} + \underbrace{C(f_y,f_z-f_0)}_{\text{side band}} + \underbrace{C^*(f_y,f_z+f_0)}_{\text{side band}} \tag{2.4}$$

where the lower-case quantities denote the direction of the Fourier transform. In Fourier space, a central DC term made from $A(f_y,f_z)$ and the components $C(f)$ will be present. Two peaks either side of this central DC term at $\pm f_0$ can be seen, referred to as the side bands, at the fundamental frequency of the fringe pattern. Either side band can be selected and set as the zero frequency, in effect shifting the side band to the position of the DC term. A 2D window function is then taken around the side band and all other signals in the Fourier space are then set to zero. Inverse Fourier transforming the data back into real space isolates the $c(y,z)$ which, by taking the argument, provides us with the phase Φ_m. It is from this phase map that the electron plasma density is calculated.

2.3.1.1 Contributions to Φ_m

The measured phase shift Φ_m is made up of a number of contributing factors, as defined by the following equation,

$$\Phi_m(x,y) = \Phi_p(x,y) + \Phi_w(x,y) + \Phi_a(x,y) \tag{2.5}$$

here, the phase shift due to the plasma is Φ_p, which is assumed to be mainly caused by the free electrons present in the plasma. Aberrations of the phase Φ_a due to the imaging could be removed by subtracting the reference region of the background shot from the data shot.

If Φ_p is the only contribution to Φ_m then the phase shifts measured by the 1064 nm probe should be twice that measured by the 532 nm probe. However, the phase contribution due to the wall Φ_w is significant. As previously demonstrated by Gonsalves [2], the heating of the sapphire wall during the discharge pulse changes the phase shift that is measured. Assuming that the main contributing factors to the measured phase shift Φ_m are the electron density and the wall heating, equation 2.5 can be re-written for each probe wavelength,

$$\Phi_m^{\lambda_1}(x,y) = \Phi_p^{\lambda_1}(x,y) + \Phi_w^{\lambda_1}(x,y) \tag{2.6}$$

$$\Phi_m^{\lambda_2}(x,y) = \Phi_p^{\lambda_2}(x,y) + \Phi_w^{\lambda_2}(x,y) \tag{2.7}$$

where λ_1 and λ_2 represent the two different wavelengths. These two equations can be solved simultaneously, using $\Phi_p \propto \lambda$ and assuming that $\Phi_w \propto \lambda^{-1}$. Given

that $\lambda_1 = 2\lambda_2$, an expression can be found for the phase shift of one of the probes due to the plasma,

$$\Phi_p^{\lambda_1}(x,y) = \frac{4}{3}\Phi_m^{\lambda_1}(x,y) - \frac{2}{3}\Phi_m^{\lambda_2}(x,y) \tag{2.8}$$

2.3.2 Phase Unwrapping

Phase unwrapping is sometimes necessary since the phase returned by the procedure outlined in section 2.3.1 returns a phase constrained to lie in the region $-\pi$ to π. If, for example, the true phase increases with position y from just below π to just above it, the retrieved phase will jump from just below π to just above $-\pi$. This is relatively easy to observe by eye but requires a special class of algorithms to find computationally. The problem is further complicated when transformed into two dimensions, because the discontinuities often do not span the entire two dimensions and so give rise to singularities or residues, which seemingly come from nowhere. These are difficult to unwrap computationally because, depending on the path taken, a different number of cycles between $-\pi$ and π is possible. The phase unwrapping algorithm chosen to eliminate this problem is called the Goldstein algorithm [43], outlined in 'Two-dimensional Phase Unwrapping: Theory, Algorithms and Software' by Dennis Ghiglia and Mark Pritt [44] which has been successfully implemented in previous work by Ibbotson [1]. This algorithm was chosen over the many available described in [44] because of its efficiency and speed.

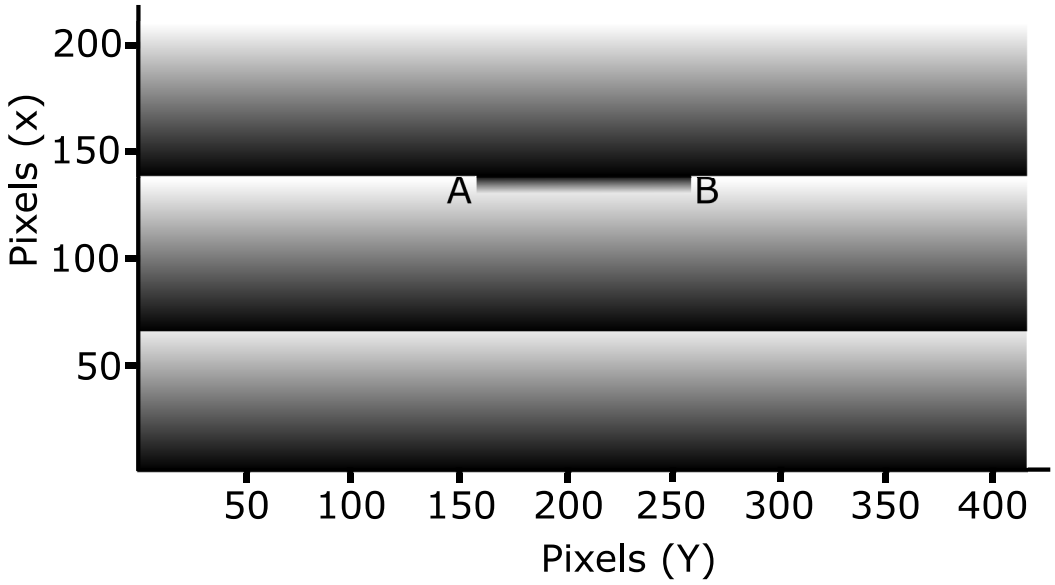


Figure 2.6: An example of a wrapped phase space, where points A & B represent residues that are discontinuities in the phase map that have to be isolated.

In the case where there are no residues, any path can be taken to unwrap the phase. This is called 'path independence' and is governed by the following condition,

$$\oint F(r) \cdot dr = 0 \tag{2.9}$$

where F is a vector function around a path r, the integral around the closed path should be zero. However, this condition is no longer true if residues are present, as the two paths are not the same. At this point the Goldstein algorithm was used to introduce branch cuts, which are lines that cannot be crossed, to force the unwrapping to meet this condition. An example of these singularities is shown in figure 2.6 where A & B represent residues. The algorithm finds residues and marks them as positive or negative according to the sign of the integral in equation 2.9, in which the path is followed in a clockwise direction. Such an example

would be point B in figure 2.6. Branch cuts are defined by drawing the shortest possible lines between pairs of positive and negative residues. Phase unwrapping is then achieved using a path which avoids branch cuts.

The Goldstein method was found by Ibbotson [1] to be very effective for two dimensions but was difficult to extend to phase-unwrapping along a third dimension (time). In his work, therefore, he performed 2D unwrapping for each point in time, then unwrapped in the temporal direction by assuming that the phase at the centre of the channel should be only slightly different from that recorded for the previous time point. This methodology was also adopted in this thesis.

2.3.3 Overview

Figure 2.7 shows the key steps in the data analysis. Figure 2.7a shows a typical interferogram obtained when the probe pulse arrived during the discharge. The first step in the analysis routine, written in MATLAB, was to crop the image and select the plasma channel. A region was also selected to be used to determine the phase background which is to be subtracted once the phase of the image had been recovered. This was taken from the image where no plasma channel formed and so purely accounted for noise. These regions are shown in figure 2.7a. A hamming window was then applied horizontally across the image, this window was chosen as it effectively reduces the ringing in the signal when a Fourier transform to the image is applied. Figure 2.7b shows the Fourier transformed image, which is a 2D transform into frequency space, that has been padded to bring the record length up to 2^n, where n is an integer. This increased the resolution of the features

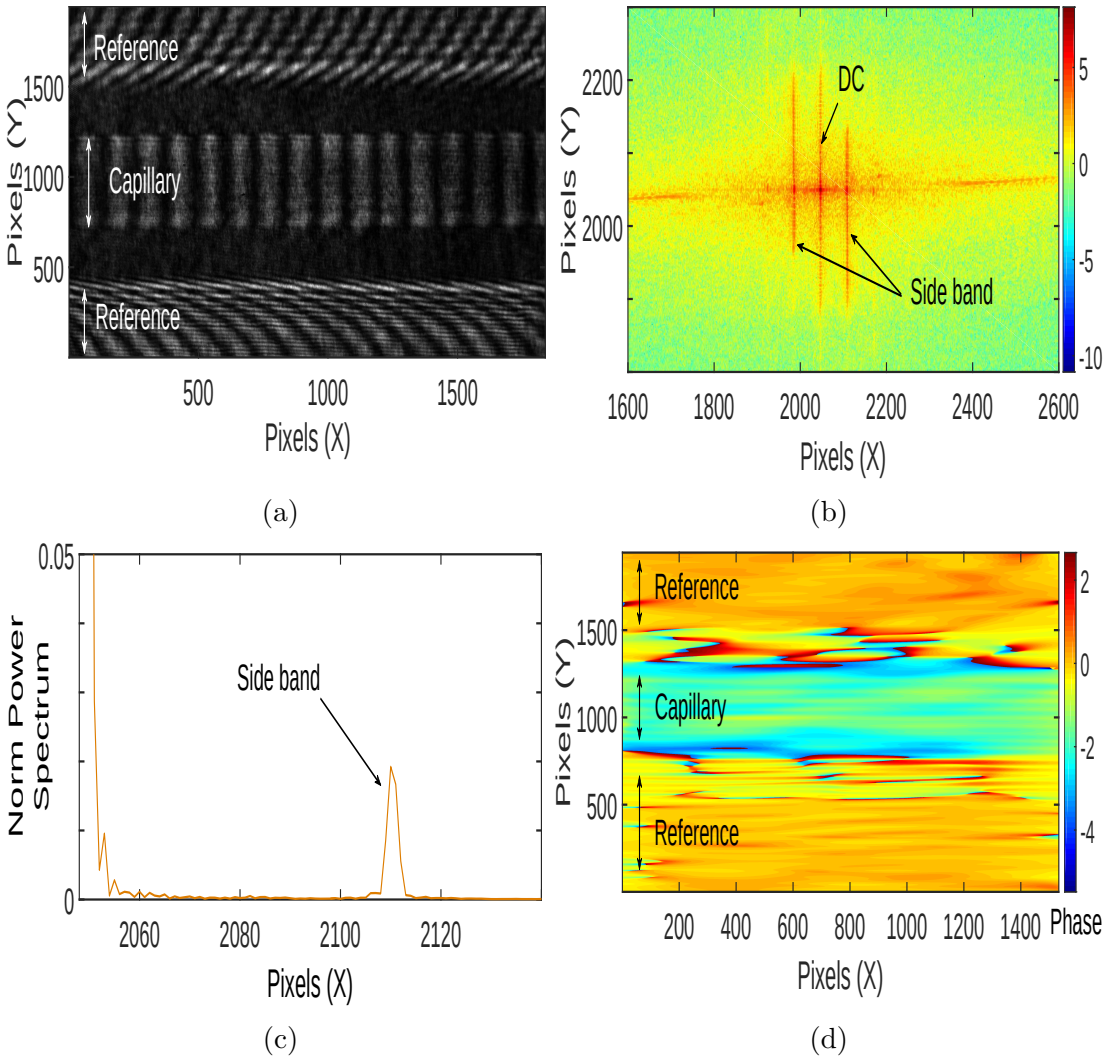


Figure 2.7: The key steps in the analysis of the data. 2.7a shows the cropped fringes. 2.7b shows the fringes in Fourier space. 2.7c shows a power spectrum of the Fourier space taken along the y-axis, cropped to show the central DC term and the right-hand side band. 2.7d shows the wrapped phase map that is produced at the end of the analysis.

in frequency by interpolating the data onto the larger grid size. The side band show some asymmetry, this is caused by the asymmetry in the references of the raw data. The side band of the image was then selected. This was most easily done by taking the two-dimensional image and creating a power spectrum, as shown in figure 2.7c. By selecting just the side band, all the phase information of interest is retained, as shown in section 2.3.1. After finding the centre of the side band, it was isolated and a square window with a Gaussian edge in the horizontal direction was applied around this region, with anything outside of this region set to zero. The side band was then shifted to the centre of the image and an inverse Fourier transform was performed, with an example of the recovered phase shown in figure 2.7d. The 'streaks' in figure 2.7d is noise in the recovered phase.

This process was performed for both the data and reference interferograms. The reference was then subtracted from the data. This gave a single image of the phase shift due to the plasma channel. At this point, the phase may require unwrapping, using the Goldstein algorithm as necessary. This method is explained in section 2.3.2 and any discontinuity in the phase is corrected. At each time interval, a lineout perpendicular to the capillary was taken of the data which gives a phase map as a function of time. The next step was to unwrap this phase map in time; again the Goldstein algorithm was implemented. The phase map was then used to calculate the plasma density and the shape of the channel, to give information about the most effective spot size which can be guided.

2.3.4 Calculating the Electron Density Profile

The measured phase is a function of the integrated plasma density along the path of the probe pulse, as defined by,

$$\Phi_m(y,x) = -\frac{e^2}{zm_e c\varepsilon_0 \omega}\int_{-X/2}^{X/2} n_e(x,y,z)dx \tag{2.10}$$

where Φ_m is the measured phase, n_e is the electron density and X is the width of the capillary along the probe. In the case of cylindrical symmetry, an Abel transform can convert the phase shifts measured along a series of parallel chords to the refractive index — and hence electron density — as a function of radial position. However, no such transformation exists for a square geometry and so an assumption about the shape of the density (or phase) profile has to be made. The form of the density profile shape was originally explored by Gonsalves [2].

To convert the measured phase in equation 2.10, it was assumed that the electron density in a capillary of square cross-section could be written as a product of a function of x and a function of y; these functions should be the same, given the square symmetry, and hence,

$$n_e(x,y) = f(x)f(y) \tag{2.11}$$

By assuming this function for the shape of the electron density, an expression is found to convert the phase as,

$$n_e(x,y) = -\frac{zm_e c\varepsilon_0\omega}{e^2}\frac{\Phi_m(y)\Phi_m(x)}{\int_{-Y/2}^{Y/2}\Phi_m(y)dy} \tag{2.12}$$

The assumption of $f(x)f(y)$ geometry introduces an error to the measurement, deduced by Gonsalves [2], of around 10 %. These assumptions are no longer held true in regions such as the gas slots, where the square symmetry is broken.

2.3.4.1 Calculating the Degree of Ionisation of the Gas

The average ionisation percentage of the gas is calculated by comparing the total number of electrons measured in one slice across the capillary, with the number which would be formed by complete ionisation of the gas contained in this region; this gives a fractional quantity to the measured ionisation. This value is taken as an average for the cross-section of the capillary and assumes that the gas fill is uniform across the capillary.

2.3.5 Calculating the Matched Spot Size

Whilst calculating the electron density is interesting in demonstrating how a plasma channel develops, the really important information, in terms of guiding, is the radial electron density distribution of the channel. A useful parameter that can be calculated from the radial electron density distribution of the channel is the matched spot size W_M that the plasma channel can support. This is defined for a parabolic channel by the following criteria,

$$W_M = \left(\frac{r_{ch}^2}{\pi r_e \Delta n_e} \right)^{\frac{1}{4}} \tag{2.13}$$

where r_{ch} is the radius of the channel and Δn_e is the change in density between the density on-axis and the value at r_{ch}. This condition for finding the matched spot size is only true for a parabolic profile, but the measured channels are rarely

parabolic. Durfee *et al.* [45] have shown that the matched spot size does not depend very strongly on the channel shape. This is shown in figure 2.8, where the shape of the channel takes the form,

$$n_e(r) = n_e(0) + \left[1 - \left(\frac{\sqrt{\Delta n_e}}{r_{ch}}\right)^{\alpha} r^{\alpha}\right] \tag{2.14}$$

where n_e is the electron density and r_{ch} is the channel radius which is kept constant at 10 µm. The α parameter defines the steepness of the channel wall. For $\alpha = 2, 4, 8$, the radius of the matched spot size, defined as where the intensity over the radius falls to 1/e, is constant for all three channels. Hence equation 2.13 can be used to estimate W_M even when the channels are not parabolic. The procedure for finding W_M is as follows:

1. Starting at $x = \Delta x$, the parameter $\Delta n_e = n_e(x) - n_e(0)$ is calculated.
2. Δn_e is used in equation 2.13 to find a value for W_M.
3. If $W_M > x$ then $x \to x + \Delta x$ and step 2 is repeated; however if $W_M \leq x$ then the matched spot size is approximately W_M

Gonsalves [2] uses his experimental data runs to plot the match spot size against pressure for different capillary diameters. From this, a two-dimensional fit can be performed to give the predicted spot size (W_M) as a function of pressure and capillary diameter,

$$W_M[\mu m] = 6.6 \times 10^4 \left(\frac{D_{cap}[\mu m]}{2}\right)^{0.651} (n_{H_2}[m^{-3}])^{-0.1875} \tag{2.15}$$

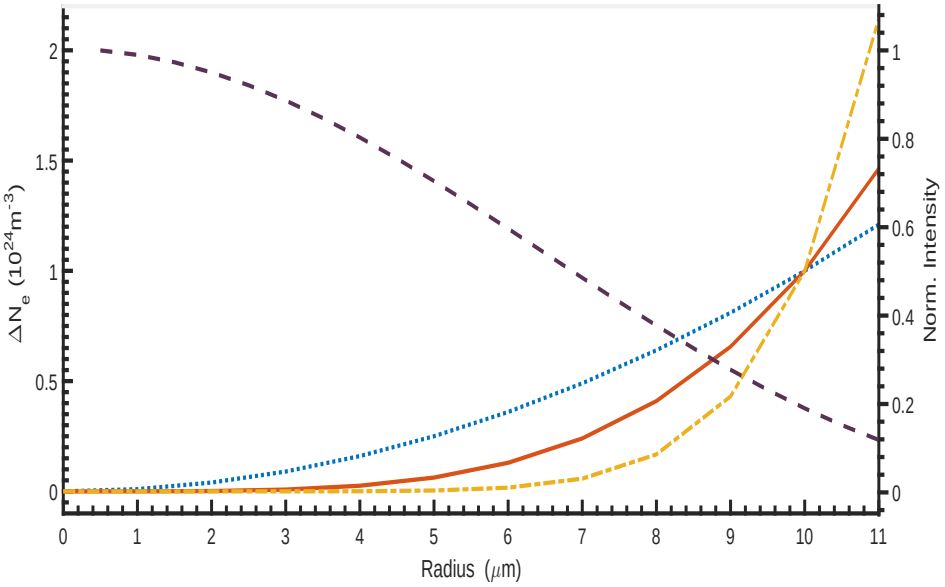


Figure 2.8: shows the electron density profile calculated using equation 2.14 for $\alpha = 2$ in blue dot, $\alpha = 4$ in solid orange and $\alpha = 8$ in yellow dash dot. The lowest order mode supported by these channels is in dashed purple, calculated from the matched spot size.

where D_{cap} is the diameter of the cap and n_{H_2} is the initial density of hydrogen molecules. The result of the predicted spot size is used in the analysis of the data to determine if the matched spot size predicted by the analysis is correct.

To further confirm the validity of the assumption made by Gonsalves [2], this procedure for finding the matched spot was compared with numerical calculations of the lowest order modes of the measured channels, using a code written by S. M. Hooker. This code was used to find the matched spot sizes of increasingly steep parabolic channels, within a capillary of 200 µm in diameter and an on-axis plasma electron density of 1×10^{24} m^{-3}. The different channels can be seen on the left hand side of figure 2.9. The electric field of the 1st order mode supported by this channel was then measured at 1/e to find the matched spot size. The

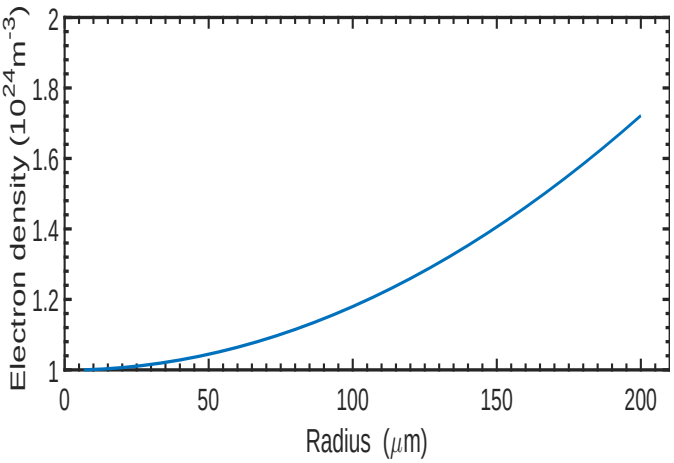
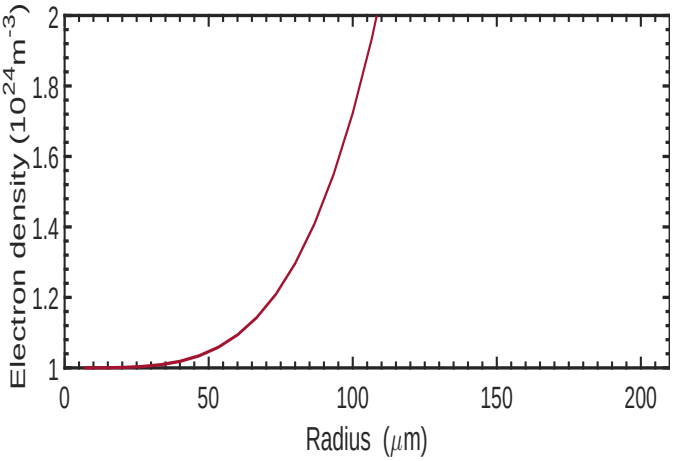
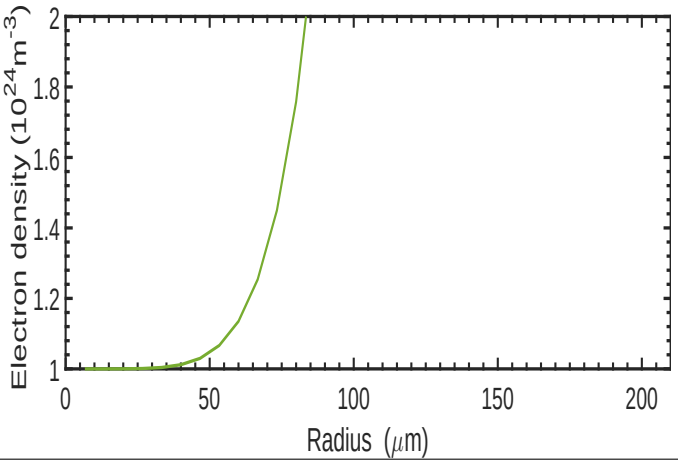
Density profile	Old	New	Profile
	26.7 µm	36 µm	x^2
	33.3 µm	35.3 µm	x^4
	33.3 µm	35.1 µm	x^6

Figure 2.9: shows the variation of electron density of x^2, x^4 and x^6 density profiles with the calculated matched spot size using the Gonsalves method (Old) and the Hooker method (New).

density profiles were then taken by the author and used in a MATLAB code to calculate the matched spot size using Gonsalves' method. It was found that these two methods have agreement of around 5 %, as can be seen in figure 2.9, apart from the x^2 channel which differs by 10 µm; this is because its rate of change is very different initially compared to the other two channels. Coincidently, the shape of the channels in the data tends to resemble the channels modelled with high order powers.

2.3.5.1 Curve Fitting

This method for finding the matched spot size is very sensitive to noise since fluctuations in the electron density can cause the procedure for finding W_M to be reached prematurely. It is therefore necessary to smooth the data by fitting a function to it. Gonsalves [2] previously found that a double Lorentzian is effective. This takes the form of,

$$n_e(x) = c_2 \left(\frac{\Delta y_0^2}{[x-R]^2 + \Delta y_0^2} + \frac{\Delta y_1^2}{[x+R]^2 + \Delta y_1^2} \right) + \sum_{i=0}^{3} c_i x^i \tag{2.16}$$

where $n_e(x)$ is the electron number density as a function of the position along the diameter of the capillary x, the centre of the Lorentzian is determined by the radius R of the capillary and how steep the sides of the Lorentzian is determined by Δy, this can be different for the two Lorentzian. The additional terms $\sum_{i=0}^{3} c_i x^i$, added to the Lorentzian add different effects to the fit: the c_0 term acts as an up/down off-set while the $c_2 x^2$ adds a slight curve to the bottom of the channel. The quality of this fit was tested by varying the additional terms to the Lorentzian by making $c_i = 0$ to see if the goodness of fit (GOF) quality

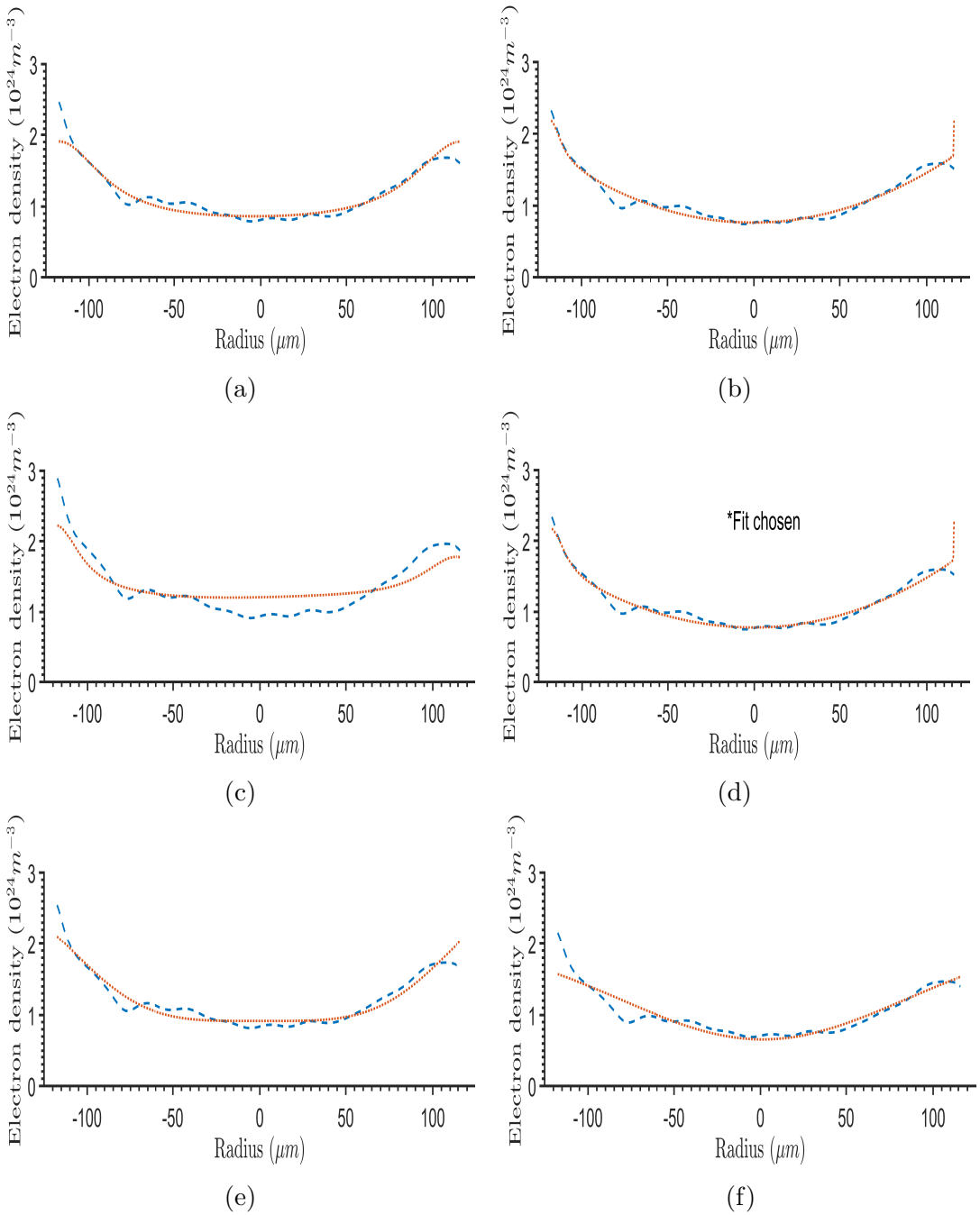


Figure 2.10: The different fitting equations, for a channel created at 100 mbar of hydrogen in a 250 µm diameter channel with the raw data (blue dashed) being compared with the fit (red dash) at 80 ns into the plasma discharge development. 2.10a shows the Lorentzian and a constant term. 2.10b shows the Lorentzian, a constant and an x^2 term. 2.10c shows the Lorentzian, a constant and an x^3 term. 2.10d shows the Lorentzian, a constant, an x^3 and an x^2 term. 2.10e shows a Super Gaussian fit, where $a_1 = 8$. 2.10f shows a Gaussian fit, where $a_1 = 2$.

factor, measured as an R-squared value, improved or declined. The function was also replaced altogether and a Super Gaussian fit of the following form was tried,

$$n_e(x) = c_2 * exp(-(\frac{x - b_1}{R})^{a_1}) + c_0 \tag{2.17}$$

where R is the radius of the capillary; a_1 the power term altering the steepness of the sides of the function; and again an off-set term in electron density c_0. The different functions are plotted against the raw data as shown in figure 2.10. It was found in general that the Lorentzian with the off-set, c_2x^2 and c_3x^3 term followed the data most closely. However, this was not chosen as the function to be used to fit the data because it often gave rise to a fluctuation in the density at the centre of the capillary, causing an incorrect spot size prediction. As a result, the double Lorentzian with an off-set was used as the fit to the data.

2.3.6 Accounting for Errors on the Measurements

The errors on the measurements made here are assumed to be the same as those previously estimated by Gonsalves [2]. It is assumed that the error on the measured phase is $\pm$ 0.1 rad, which corresponds to an error in the density measurements of $\pm$ 0.1 $\times$ 10^{24} m^{-3}. The error in the calculated matched spot size is 15 %, originally found by looking at the statistical fluctuations in the results of several experiments performed under the same conditions.

2.4 Results

2.4.1 Benchmark Experiments

Initially, the results from a standard capillary discharge are presented to act as a comparison with the results obtained for a change in discharge circuit, using helium and changing the sapphire plates for diamond ones. The plasma channel was 15 mm long confined in a 250 µm square cross-section guide, filled with hydrogen gas, broken down using the thyratron circuit, with a charging voltage of 16.5 kV, which for these parameters drove a current pulse of approximately 120 ns durations, 450 A peak current.

Figure 2.11 shows the time evolution of the measured electron density profile. It illustrates that as the discharge is applied at 20 ns there was an increase in electron density and the starting formation of a channel can be observed. At a steady state formed by 80 ns, this channel is maintained until 120 ns when the current begins to decrease and so the channel begins to relax. This time evolution of the channel can be described by the simulation carried out by Broks *et al.* [41]. The initial density profile at 20 ns is described as the ionisation phase, in which the dominant energy loss for the discharge current was ionisation. During this time, heat transfer to the wall was 'slow', creating this relatively flat density profile. But by 60 ns, the ionisation of the channel has increased and ohmic heating has increased the electron temperature in the center of the channel to 8 eV according to the computational modelling by Broks *et al.* [41]. A temperature gradient was then set up, as heat was conducted to the wall. The pressure gradient was rapidly equalised, via bulk flow of the electrons from the centre of the

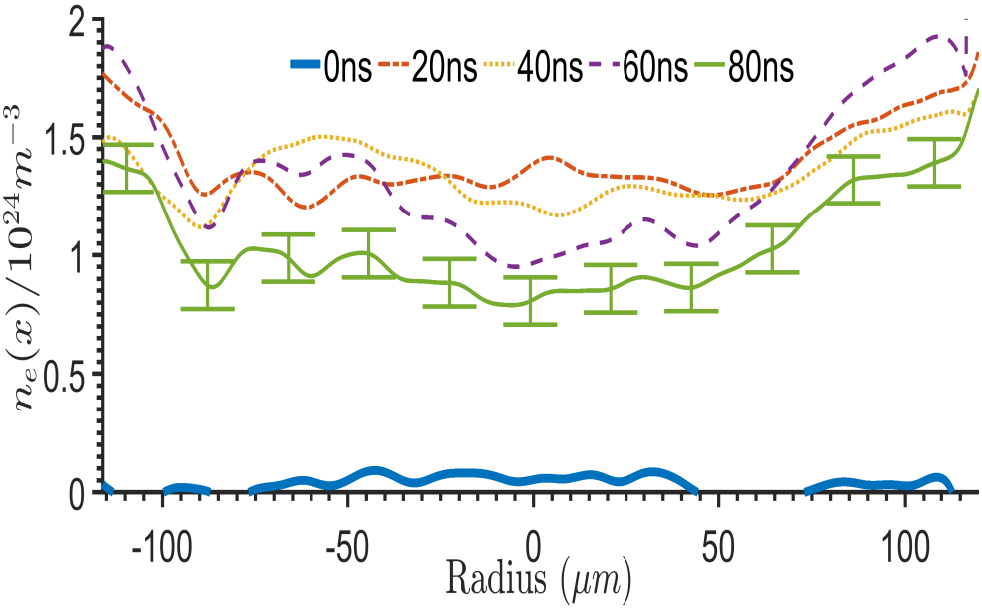


Figure 2.11: Temporal evolution of the corrected transverse electron density profile as a function of transverse coordinate x for a square cross-section capillary of side 250 µm connected to a thyratron discharge circuit, charged to 16.5 kV, with a hydrogen backing pressure of 100 mbar. The curves are labelled by the delay of the laser probe pulse after the onset of the discharge current.

capillary to the wall. This causes a stable plasma channel to be reached by 80 ns, with a minimum electron density on-axis. The channel shape was maintained but the degree of ionisation in the channel decreased, as the thyratron discharge circuit reduced the energy supplied to the system. At about 120 ns the channel profile began to relax, as the heat transfer to the wall again slowed.

Figure 2.12 shows the evolution of the ionisation of the plasma channel during the discharge pulse. The time axis is labelled by the delay of the laser probe pulse after the onset of the discharge current. It is noted that there was a relatively fast rise time of the plasma ionisation, which occurred within 25 ns, and that the ionisation percentage varied with the current. It was observed that there is

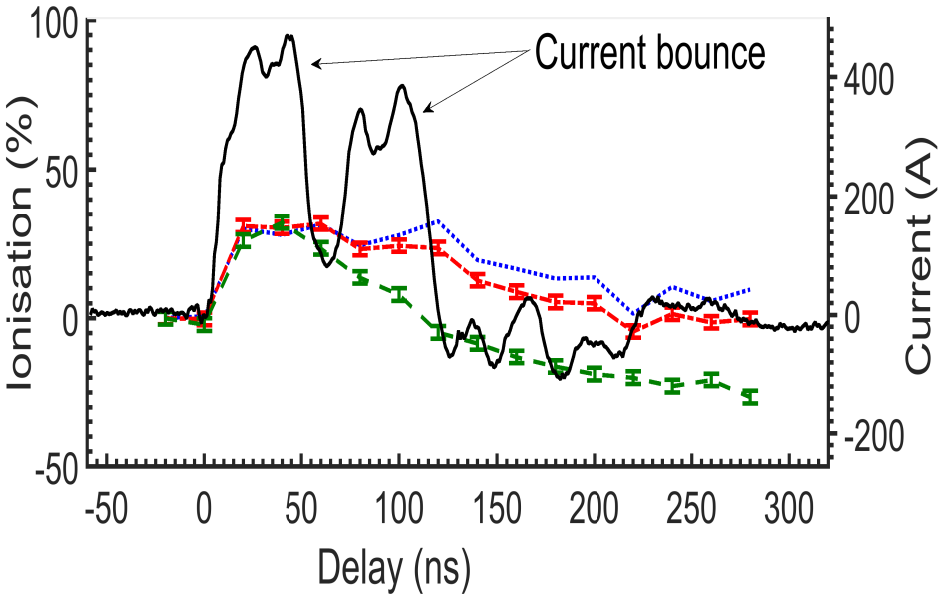


Figure 2.12: Temporal evolution of the deduced percentage ionisation as a function of time during the discharge pulse for a square cross-section capillary of side 250 µm connected to a thyratron discharge circuit, charged to 16.5 kV, with a hydrogen backing pressure of 100 mbar. The green dashed line represents the 532 nm data, the red dash dot line represents the 1064 nm data and the blue dotted line represents the corrected data. The negative ionisation level of the green data, at later time delays, is caused by the phase contribution being dominated by the heating of the sapphire wall. The black solid line shows the current trace for the discharge. The discontinuity of the current trace is caused by 'current bounce' from the discharge circuit.

a slight drop in ionisation at around 80 ns, and the ionisation then increased again with the second current spike, until the ionisation slowly decreased due to re-combination of the plasma and losses of electrons to the wall post-140 ns.

Figure 2.13 shows that as the plasma channel was formed at around 25 ns, the matched spot size reaches the predicted spot size, given by the thick solid gold line. The predicted spot size is an estimate of the focal spot that a channel of a

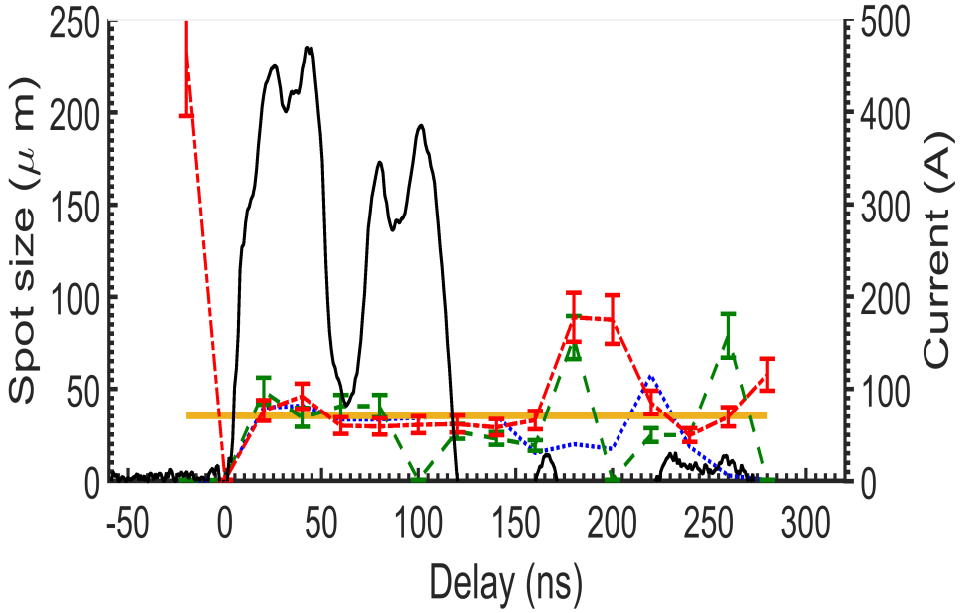


Figure 2.13: Temporal evolution of the deduced matched spot size as a function of time during the discharge pulse for a square cross-section capillary of side 250 µm connected to a thyratron discharge circuit charged to 16.5 kV, with a hydrogen backing pressure of 100 mbar. The thick solid gold line represents the matched spot size predicted by equation 2.13; the dashed green line represents the spot size prediction for the 532 nm data; the red dash dot line represents the spot size prediction for the 1064 nm data and the blue dotted line represents the spot size prediction for the corrected data. The black solid line shows the current trace for the discharge.

given diameter and density can guide. For these parameters the predicted spot size is 35 µm. The matched spot size was maintained at almost the predicted spot size for the rest of the discharge. With a slight decrease in matched spot size to less than the predicted spot size, coinciding with the second current spike at around 80 ns. The matched spot size then increased as the current turned off and the electron density profile became more uniform.

As demonstrated in both figure 2.12 & figure 2.13, at later times the discrepancy between the measurements made by the 1064 nm and the 532 nm wavelengths of the probe increased, suggesting that a much heavier reliance on the correction factor was necessary for this data. This increasing discrepancy was caused by the change in the refractive index of the sapphire with temperature, due to the transfer of heat from the plasma channel to the wall. A correction factor can be used to account for this, shown as the blue dashed dot line in figures 2.12 & 2.13, which is calculated as described in section 2.3.1.1. At later time delays, particularly seen in figure 2.12, the measured ionisation level for the 532 nm wavelength became negative, suggesting the phase contribution from the wall dominated.

This data is very similar to the data recorded by both Ibbotson & Gonsalves [2]. Here, I will compare this to Ibbotson's data, as this is the most recent results. Like Ibbotson, the data was taken for capillaries that are used for waveguide experiments. However, in these experiments a slightly larger square capillary cross-section was used of 250 µm rather than 200 µm used by Ibbotson, but the same peak discharge current of 400 A was used to avoid damaging the sapphire, making it possible to collect multiple images from one capillary. The discrepancy in capillary diameter size means that for this experiment a current density of 6.72 $\mathrm{mA\,\mu m^{-2}}$ was achieved. This is lower than the current density of 10.5 $\mathrm{mA\,\mu m^{-2}}$ achieved by Ibbotson and therefore the same ionisation levels are not reached.

The temporal evolution of the electron density profile closely follows that measured by Ibbotson & Gonsalves. It is noted that, as seen by Gonsalves, there is a time in the development of the electron density profile where the centre of the

channel is not a minimum, usually around 60 ns, as can be seen in figure 2.11. This feature is thought to be caused by a reflection of expanding plasma from the capillary wall; this leads to the formation of a temporary local electron density maximum on-axis which causes an anti-guiding effect. However, this reflected plasma is not permanent and is removed over the next 20 ns.

2.4.2 Change of Circuit Design Used to Produce Plasma Channel Experiments

The plasma formed in a capillary discharge waveguide is generated by applying a large electrical voltage across the capillary filled with gas. The high voltage has been supplied in previous work by a thyrtron circuit but this causes large electrical noise; a discontinuous current profile, is over-engineered and bulky. Because of this, a new circuit was designed to drive the capillary discharge waveguides called the Compact Marx Bank. In this section, the plasma channel formed by the Compact Marx Bank is measured and compared against the thyrtron circuit.

The thyrtron circuit high voltage was supplied by a 1-2 nF capacitor, which was charged by a Glassman power supply unit to a working voltage of 20-30 kV. This was switched into a 50 Ω coaxial cable by a thyratron high voltage switch (e2v cx1685) to complete the circuit and deliver a large voltage to the electrodes of the capillary discharge waveguide. The electrical diagram of this circuit is shown in figure 2.14a. The components were placed in a large metal box measuring $50 \times 30 \times 50$ cm. Due to the size of this box the equipment was kept outside the vacuum chamber and hence it was necessary to use a coaxial cable 2-3 m

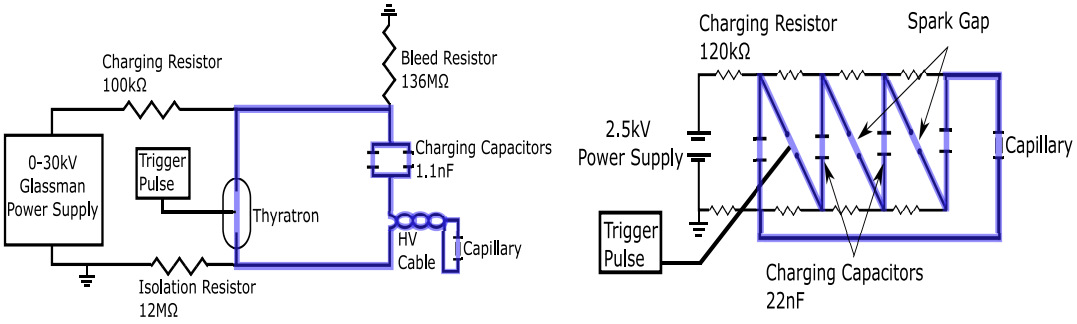


Figure 2.14: Circuit diagrams of the two supply circuits investigated in this work. 2.14a shows the electrical diagram of the thyratron circuit and 2.14b shows the electrical diagram of the Compact Marx Bank. The path taken by the current when the discharge is fired is shown in blue.

long to connect the discharge circuit to the electrodes of the capillary discharge waveguide. This produced a unique problem of 'current bounce' as the coaxial cable is not matched to the impedance of the plasma. This caused a discontinuous current profile, as can be seen by the current trace given by the black line in figure 2.13.

An alternative to this system is the Compact Marx Bank designed and built by A. Dyson [46]. Here, a Compact Marx Bank and trigger unit as shown in figure 2.14b were housed in a single box. The Compact Marx Bank circuit was arranged in an RC ladder network, where multi-layer compact chip capacitors of capacitance 22 nF were charged through a 120 kΩ resistor in parallel and then discharged in series through the spark gaps, to deliver up to a 20 kV, 500 A pulse. The spark gaps were bare wires arranged tip to tip with a gap between them of 1-2 mm, this was adjusted so that the spark gaps remain closed when the circuit was charging. The spark gaps were found to last $>$ 10000 shots before having to be readjusted.

The transformer trigger unit, also housed in this box, delivered a -5 kV trigger pulse via a thin wire to the first spark gap and so initiated the first breakdown. The box was air-tight and maintain at atmospheric pressure inside the vacuum chamber by a 5 mm pipe connected to the outside of the vacuum chamber. The Compact Marx Bank was also supplied with an external high voltage power supply, delivering up to 2.5 kV to the capacitors; an external trigger provided by a high speed MOSFET HV switch (SPA17N80C3) sent a 1.25 kV, 100 ns pulse to the the transformer trigger unit.

One advantage of the Compact Marx Bank system was that there is no longer a 'current bounce', as the coaxial cable is less than 20 cm, and thus produces a smooth current profile in time. The short distances travelled by the high current also meant the Compact Marx Bank generated less electrical noise. Additionally, all the HV components were contained within the vacuum chamber, making the system much safer to use. If multiple acceleration stages were to be used, these compact discharge systems could be located next to one another in the vacuum chamber. The capacitors could be charged using a battery and miniature EMCO PCB 2.5 kV HV supply, as the time averaged power needed is low at < 1 W. Using a battery as a supply would have the further advantage of isolating the discharge from the laboratory earth which inhibited breakdown of the chamber walls and other equipment.

The electron density profile created by the Compact Marx Bank system is shown in figure 2.15, for a 15 mm long, 250 µm square capillary, with an initial backing of a 100 mbar of hydrogen. The capacitors were charged to 2 kV, to ensure

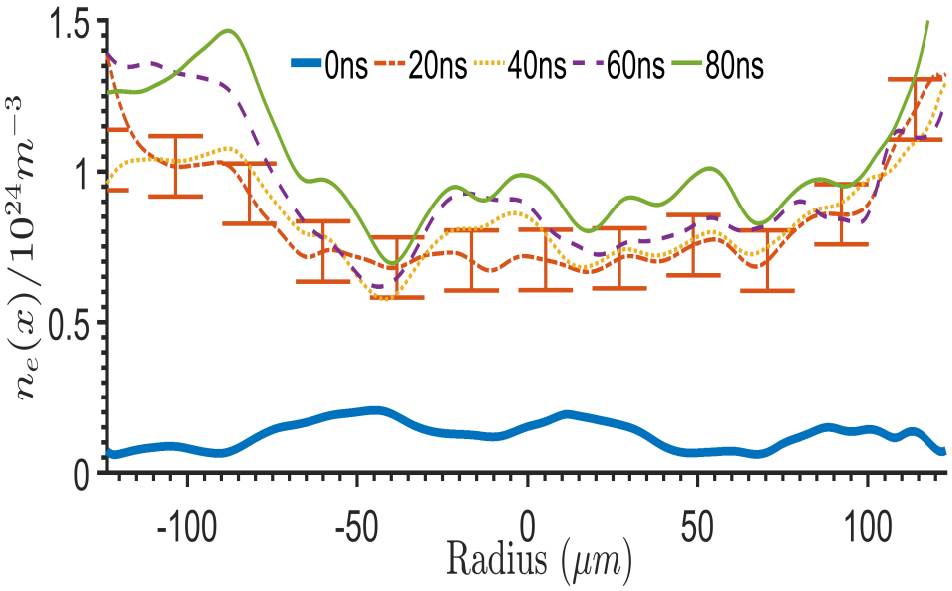
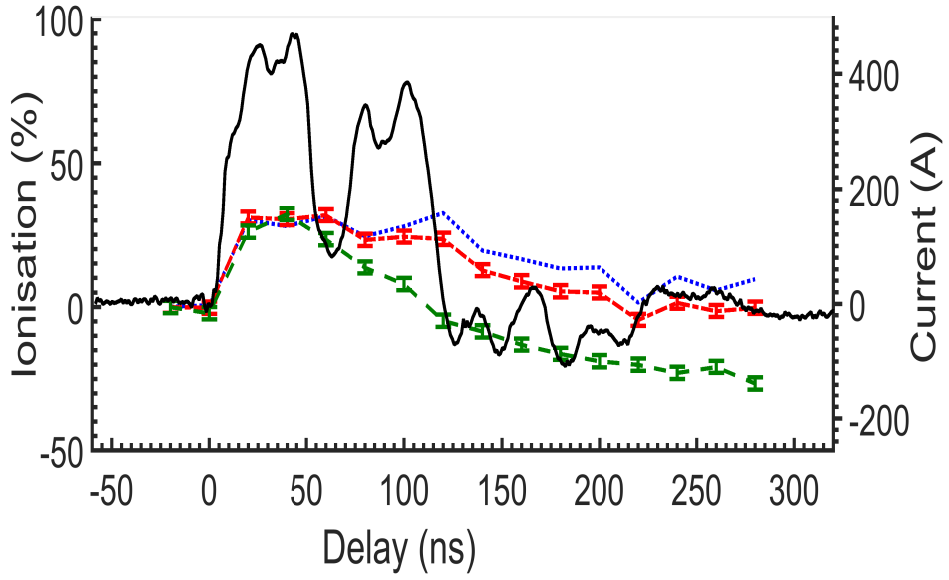


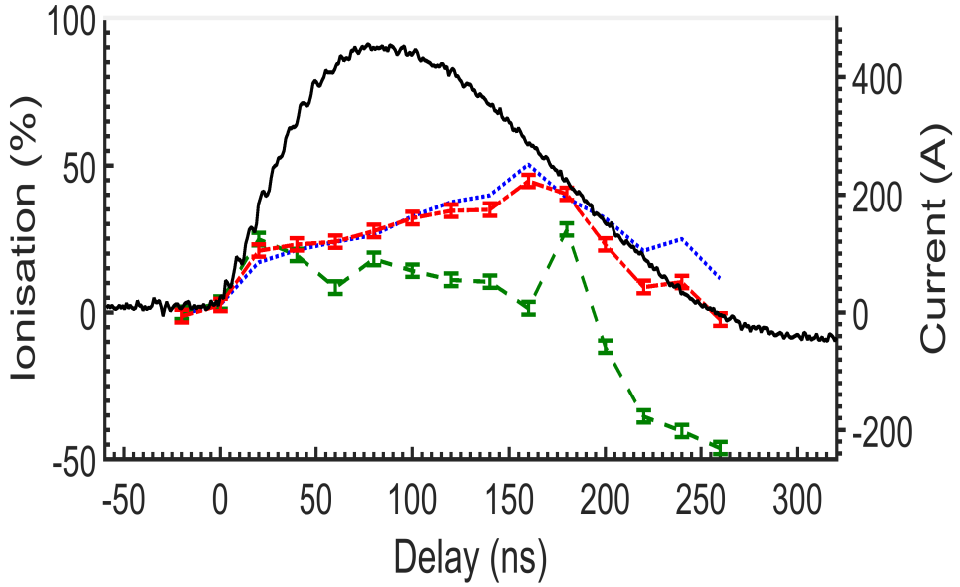
Figure 2.15: Temporal evolution of the corrected transverse electron density profile as a function of transverse coordinate x for a square cross-section capillary of side 250 µm connected to the Compact Marx Bank discharge circuit, charged to 2.0 kV, with a hydrogen backing pressure of 100 mbar. The curves are labelled by the delay of the laser probe pulse after the onset of the discharge current.

that a similar peak current of around 450 A was produced, so a comparison of the effects of this discharge circuit could be made against the thyrtron discharge circuit. A very similar trend to that of the channel formed by a thyratron circuit and the peak axial electron densities are seen, as shown in figure 2.15. However, the lifetime of the plasma channel formed by the Compact Marx Bank system was almost double that obtained with the thyratron circuit, as the Compact Marx Bank system delivered a continuous current for almost double the time of the thyratron circuit.

Figure 2.16, shows the ionisation percentage of the Compact Marx Bank and thyratron circuits. For 0 ns to 50 ns the Compact Marx Bank produced plasmas



(a)



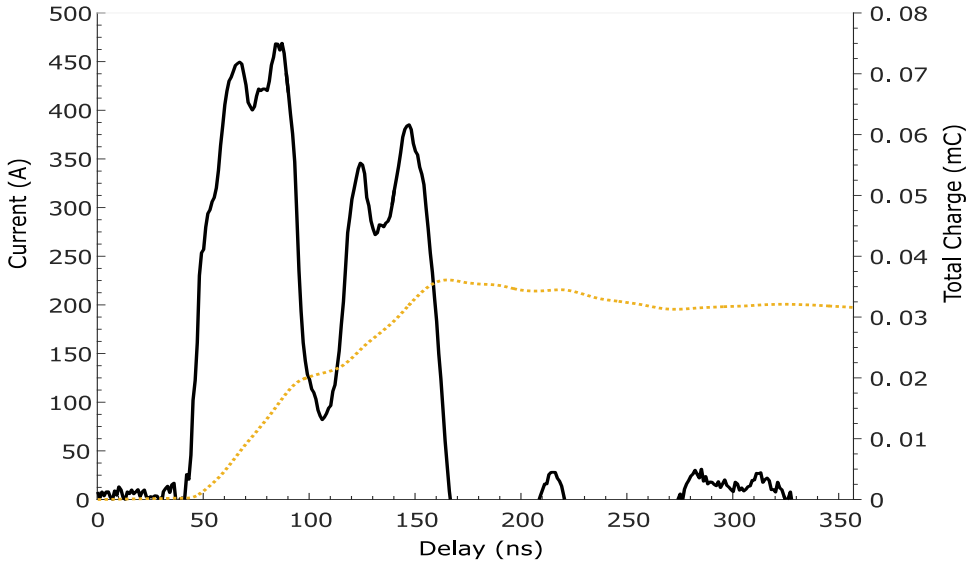
(b)

Figure 2.16: Temporal evolution of the deduced percentage ionisation as a function of time during the discharge pulse for a square cross-section capillary of side 250 µm, with a hydrogen backing pressure of 100 mbar, connected to a thyratron discharge circuit charged to 16.5 kV in figure 2.16a (the same as in section 2.4.1) and Compact Marx Bank circuit charged to 2.0 kV in figure 2.16b. The green dashed line represents the 532 nm data, the red dash dot line represents the 1064 nm data and the blue dot line represents the corrected data. The black solid line shows the current trace for the discharge.

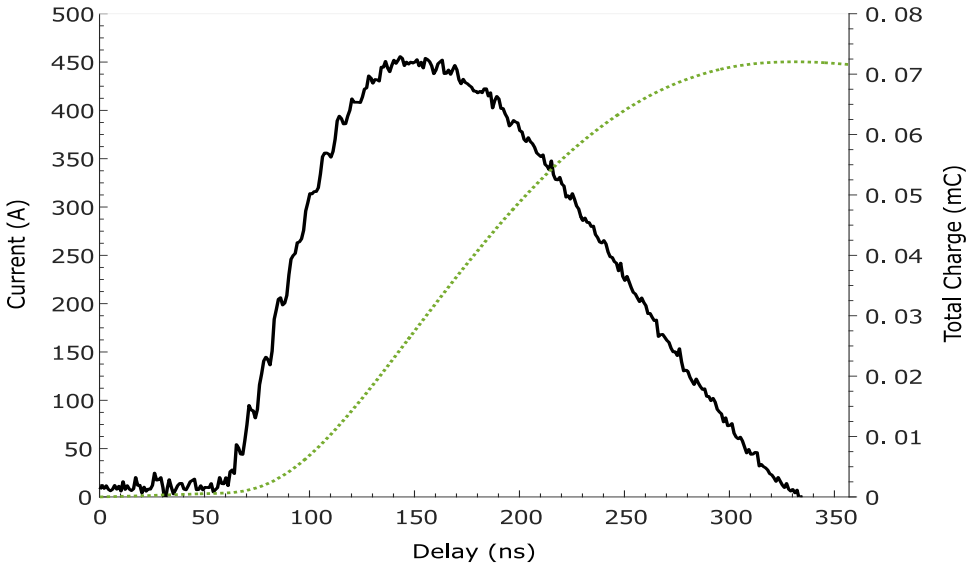
with a similar ionisation percentage as the thyratron circuit. However, at later times (>70 ns) during the discharge, much higher peaks of the ionisation percentage were achieved using the Compact Marx Bank, peaking at around 50 %. This is almost double that achieved by the thyratron circuit. Furthermore, it is seen that the period of time for which the channel was ionised above > 20 % was double that achieved for the thyratron circuit.

The increased ionisation percentage achieved by the Compact Marx Bank can be explained by considering the total charge supplied by the circuit, as is seen in figure 2.17. The total charge was calculated by integrating the current traces delivered to the plasma by the circuit. During the first 150 ns, both circuits delivered about the same amount of charge to the system. However, because of the 'current bounce' in the thyratron circuit, the charge delivered to the system began levelling off and hence the energy supplied in the middle of the channel formation stopped increasing as did the percentage ionisation; see figure 2.16a. The same was not seen for the Compact Marx Bank as there was no 'current bounce', just a continuous smooth current profile. This continually supplied energy into the plasma and so caused a continual increase in the percentage ionisation as can be seen in figure 2.16b.

Figure 2.18 compares the evolution of the matched spot sizes for the two circuits. It is seen that both circuits produced matched spot sizes which were close to those predicted by the scaling law given by equation 2.13, but the duration of the plasma channel produced by the Compact Marx Bank was approximately twice that achieved with the thyratron circuit.

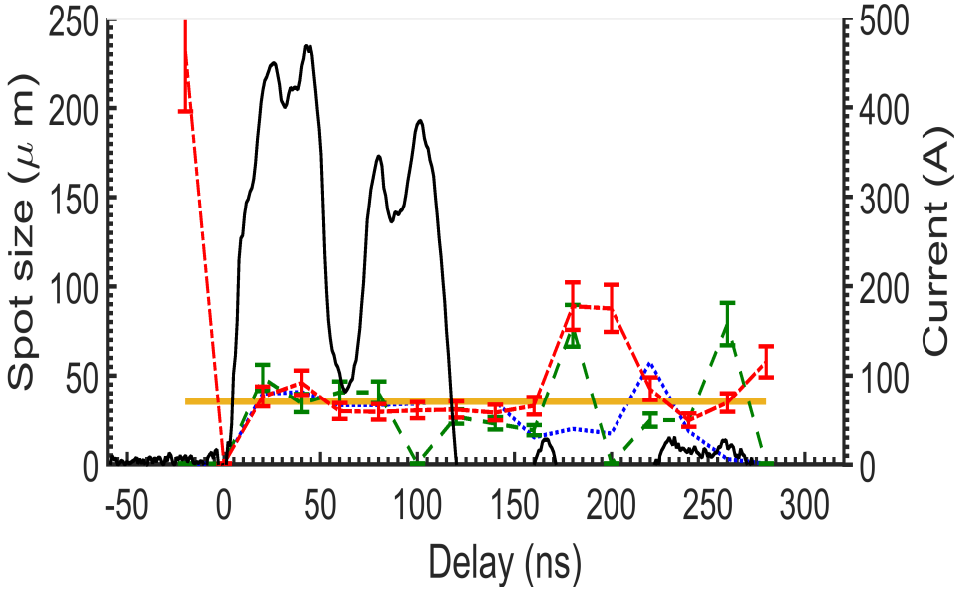


(a)

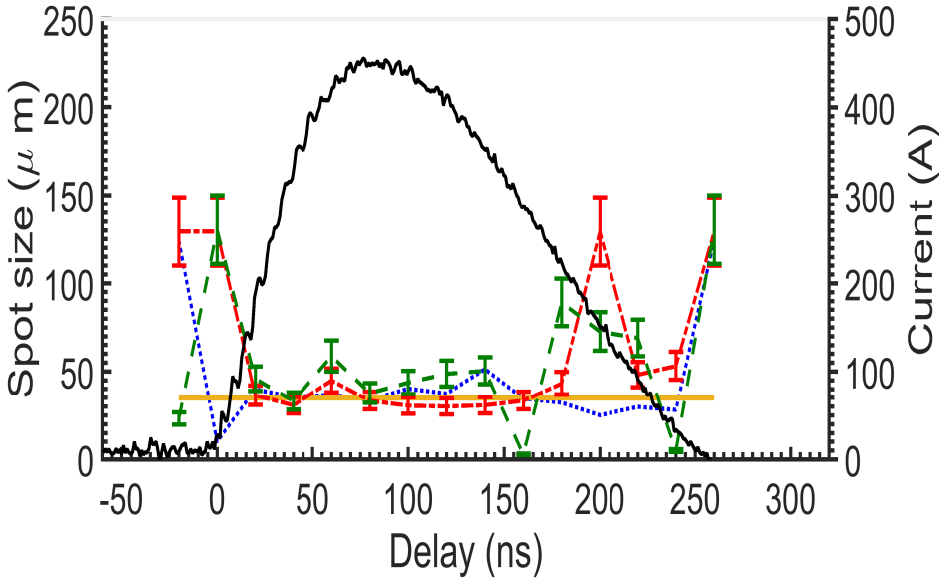


(b)

Figure 2.17: Comparison of the charge delivered by the two different discharge systems over time, for a 15 mm long, 250 µm square cross-section capillary with a hydrogen backing pressure of 100 mbar. The black line in both figures shows the current trace of the discharge system. With the thyratron circuit in 2.17a, where the gold line represents the total charge and the Compact Marx Bank discharge in 2.17b, where the green line represents the total charge delivered.



(a)



(b)

Figure 2.18: Temporal evolution of the deduced matched spot size as a function of time during the discharge pulse for a square cross-section capillary of side 250 µm, with a hydrogen backing pressure of 100 mbar, connected to a thyratron discharge circuit charged to 16.5 kV in figure 2.18a, as in section 2.4.1, and a Compact Marx Bank discharge circuit charged to 2.0 kV in figure 2.18b. The solid thick gold line shows the matched spot size predicted by equation 2.13, the dashed green line shows the spot size deduced from the 532 nm data, the red dashed dot line shows the spot size prediction for the 1064 nm data and the blue dotted line represents the spot size prediction for the corrected data. The black solid line shows the current trace for the discharge.

2.4.3 Change of Gas Experiments

It was decided to investigate channel formation in helium-filled capillary discharges; to the author's knowledge this was the first such study to be performed. As explained in section 2.3.1.1, for hydrogen plasmas the main contribution to the phase shift arises from the plasma electrons. Kim *et al.* [47] also found this to be the case for helium plasmas formed by ionisation of helium gas by 20 mJ, 240 fs pulses from a Ti:sapphire laser pulse. This is in contrast to the method of plasma production used in this experiment; however, in Kim's [47] experiment the spatial wings of the laser pulse produce a plasma that did not become fully ionised but the measured phase in this region still matched the simulated model of the system, suggesting that the only contribution to the measured phase shift of a helium plasma is the presence of electrons.

Figure 2.19 shows the evolution of the transverse electron density profile produced in 250 µm square cross-section capillaries with a helium backing pressure of 100 mbar, connected to a thyratron discharge circuit charged to 16.5 kV. It is clear that the lifetimes of the plasma channels are the same as when the capillary is filled with hydrogen. However, the on-axis density of the helium plasma channel is approximately four times higher (at around 4×10^{24} m^{-3}) than the hydrogen plasma channel (which is around 1×10^{24} m^{-3}).

Figure 2.20 shows how the percentage ionisation level of the channel develops with time. For helium, 100 % ionisation means liberating both the first and second electron. The peak percentage ionisation level of the plasma channel is

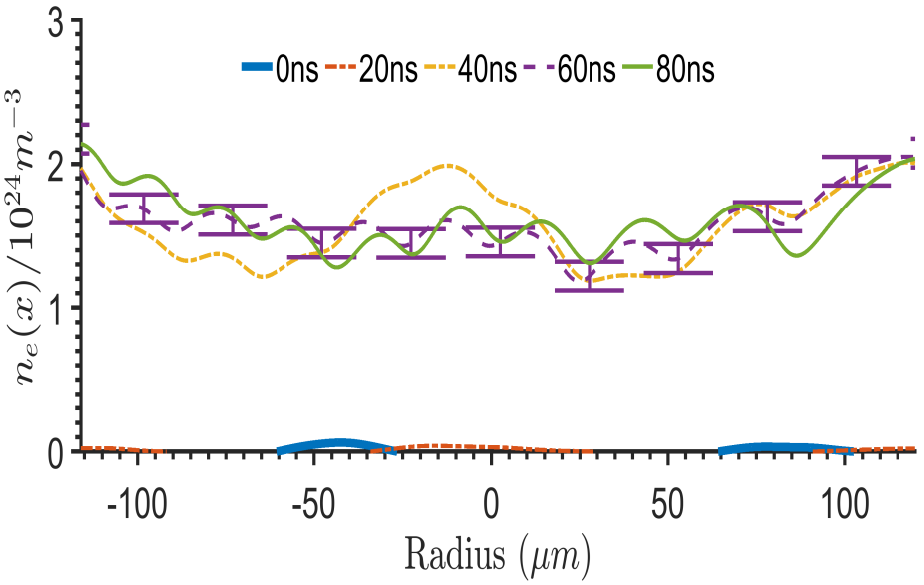
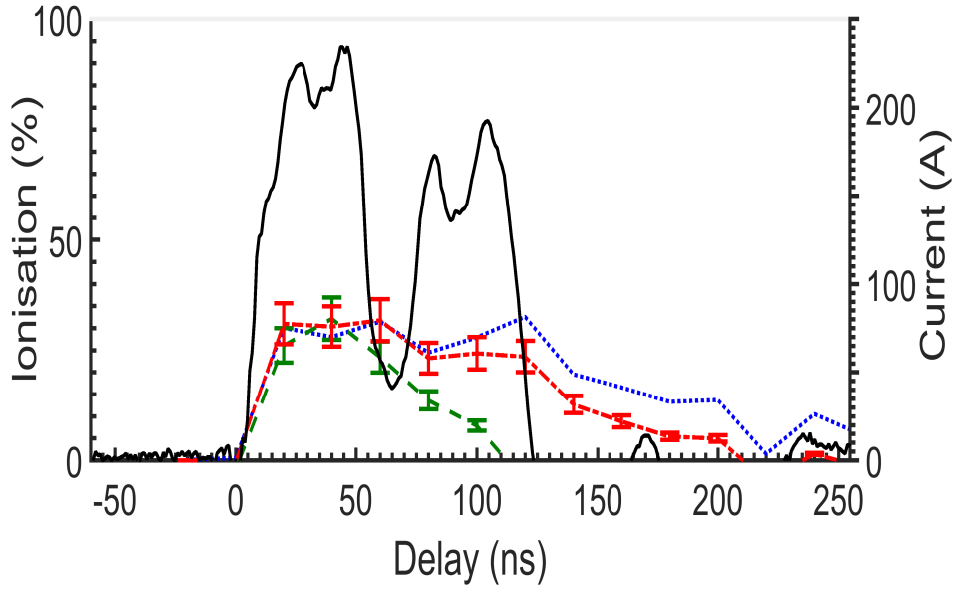
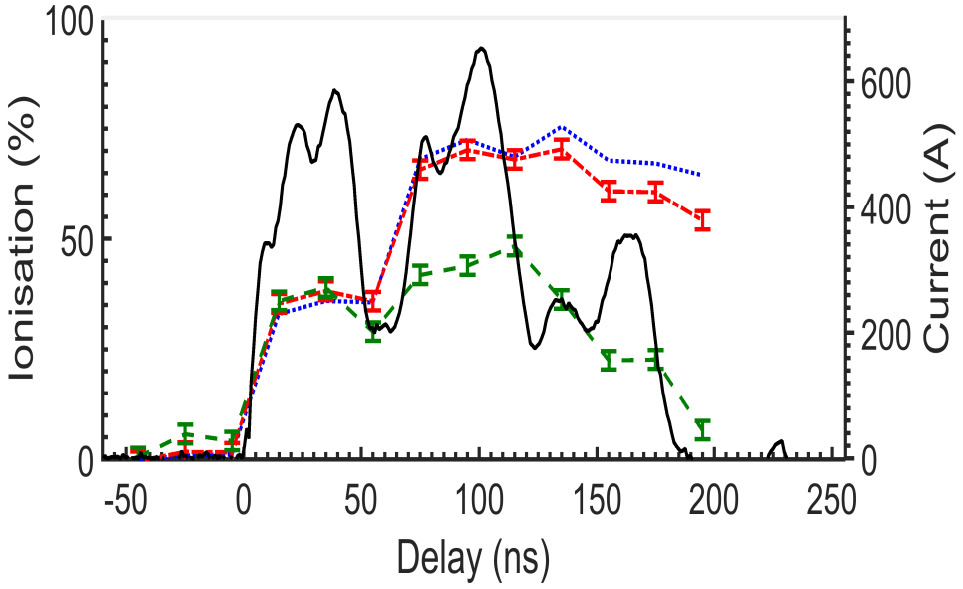


Figure 2.19: Temporal evolution of the corrected transverse electron density profile as a function of transverse coordinate x for a square cross-section capillary of side 250 µm connected to the thyratron circuit charged to 16.5 kV, with a helium backing pressure of 100 mbar. The curves are labelled by the delay of the laser probe pulse after the onset of the discharge current.

almost twice as large as that for hydrogen. Initially, both discharges have very similar ionisation levels and peak current spikes. However, in the second half of the discharge ($>$ 60 ns) the ionisation level for helium increases substantially, which interestingly coincides with the current bounce. The reason for this is not known, as a helium plasma should be much harder to form owing to its higher energy ionisation level. However, helium does have a metastable state, so it should liberate its first electron forming a percentage ionisation level similar to the bench mark hydrogen plasmas. Conducting a brief review of the literature there is some evidence by Svensson *et al.* [48] that the actual measured helium pressure and the electron number density are not 1:1 but actually 1:1.3. The author conducted further 2D OpenFOAM simulations (see section 3.3 for further

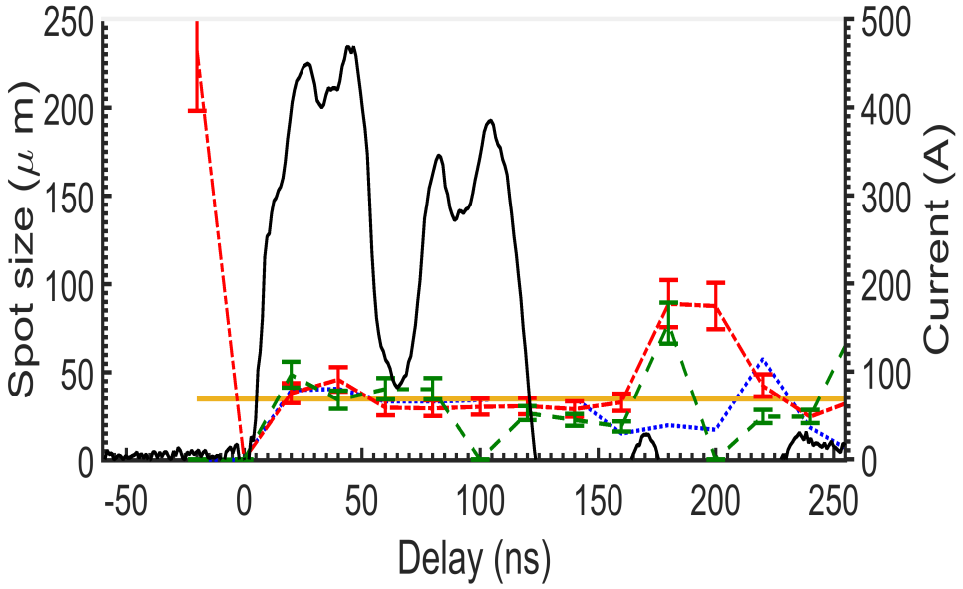


(a)

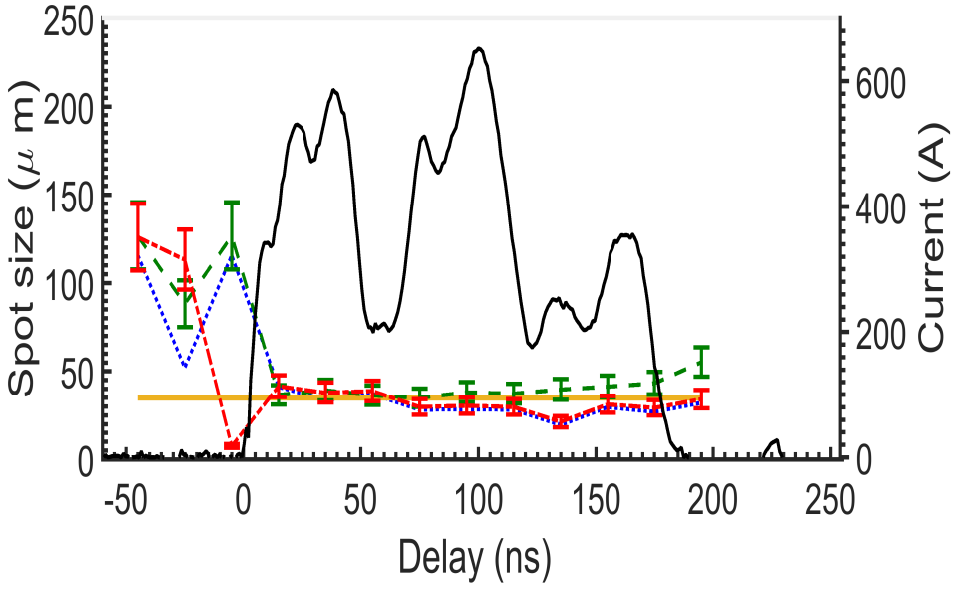


(b)

Figure 2.20: Temporal evolution of the deduced percentage ionisation as a function of time during the discharge pulse for a square cross-section capillary of side 250 µm, connected to a thyratron discharge circuit charged to 16.5 kV, with a hydrogen backing pressure of 100 mbar in figure 2.20a the same as in section 2.4.1 and a helium backing pressure of 100 mbar in figure 2.20b. The green dashed line represents the 532 nm data; the red dot dashed line represents the 1064 nm data and the blue dotted line represents the corrected data. The solid black line shows the current trace for the discharge.



(a)



(b)

Figure 2.21: Temporal evolution of the deduced matched spot size as a function of time during the discharge pulse for a square cross-section capillary of side 250 µm, connected to a thyratron discharge circuit charged to 16.5 kV, with a hydrogen backing pressure of 100 mbar in figure 2.21a, the same as in section 2.4.1 and with a helium backing pressure of 100 mbar in figure 2.21b. The thick solid gold line represents the matched spot size predicted by equation 2.13; the dashed green line represents the spot size prediction for the 532 nm data; the red dot dashed line represents the spot size prediction for the 1064 nm data and the blue dotted line represents the spot size prediction for the corrected data. The solid black line shows the current trace for the discharge.

detail on methodology) but could not find the same discrepancy in the specific heats of the gas identified in Svensson's work, that gave the difference between the measured pressure and the electron number density. Further studies are required to understand the problem fully.

Figure 2.21 shows that despite the increases in percentage ionisation for a helium plasma, the time window for guiding is similar to that obtained in hydrogen-filled capillaries; at $>$ 20 ns the matched spot size of the plasma channel reached that predicted by equation 2.15. This was maintained for the rest of the discharge, with a slight decrease in the predicted spot size to less than the matched spot size, coinciding with the second current spike at around 60 ns.

2.4.4 Change of Capillary Material Experiments

Since the capillary discharge waveguide was first invented [49] only two materials have been used for the capillary: alumina [50] and sapphire [51]. Of these, the latter has become more prevalent owing to the fact that it has a higher melting point and thermal conductivity; it is also transparent in the optical region, which makes it easier to detect capillary failures and, as shown in this chapter, allows optical access for probing of the plasma channel [52]. It has previously been shown that capillaries made from sapphire can survive for tens of thousands of discharge pulses, though this does however lead to an erosion of the material over time. An interesting alternative material is diamond since it has a much higher thermal conductivity and so is expected not to suffer the same heat damage for the same energy deposited as sapphire. In order to test this, man-made diamond sheets

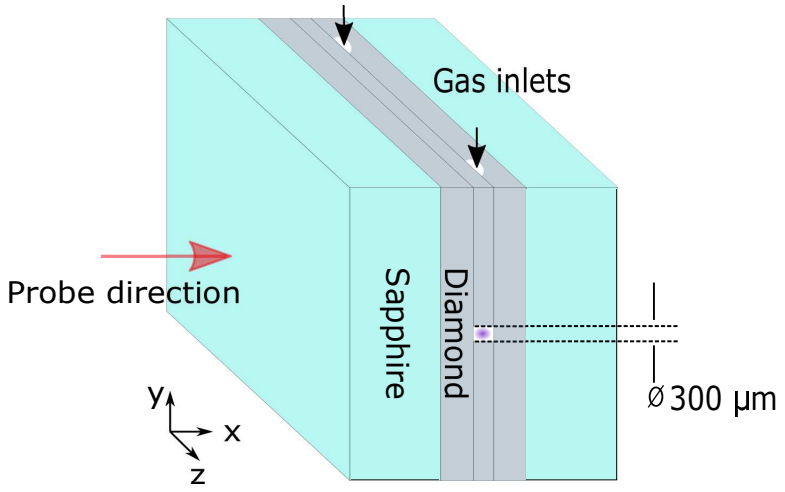


Figure 2.22: Schematic diagram showing the layout of diamond blocks and spacer plates, which were placed over the sapphire blocks.

were procured. These were polished, so that transverse interferometry could be carried out on them in exactly the same way as on the sapphire. However, owing to the high cost of material, and to avoid redesigning the capillary holder, thin sheets of diamond were used rather than replacing the whole sapphire block. The arrangement employed is shown schematically in figure 2.22. Here, two large sheets of CVD diamond measuring $15 \times 20 \times 0.5$ mm (Euclid Techlabs) were placed in front of the sapphire blocks and the spacer plates were replaced by $9 \times 15 \times 0.3$ mm diamond spacer plates to form a 15 mm long, 300 µm square capillary.

Figure 2.23 shows the image of the fringes obtained with the 1064 nm probe beam. It is difficult to retrieve a phase map from these fringes and hence deduce the ionisation percentages in the channel. It was found that the poor quality fringes were the result of scattering of the probe beam on the diamond; with

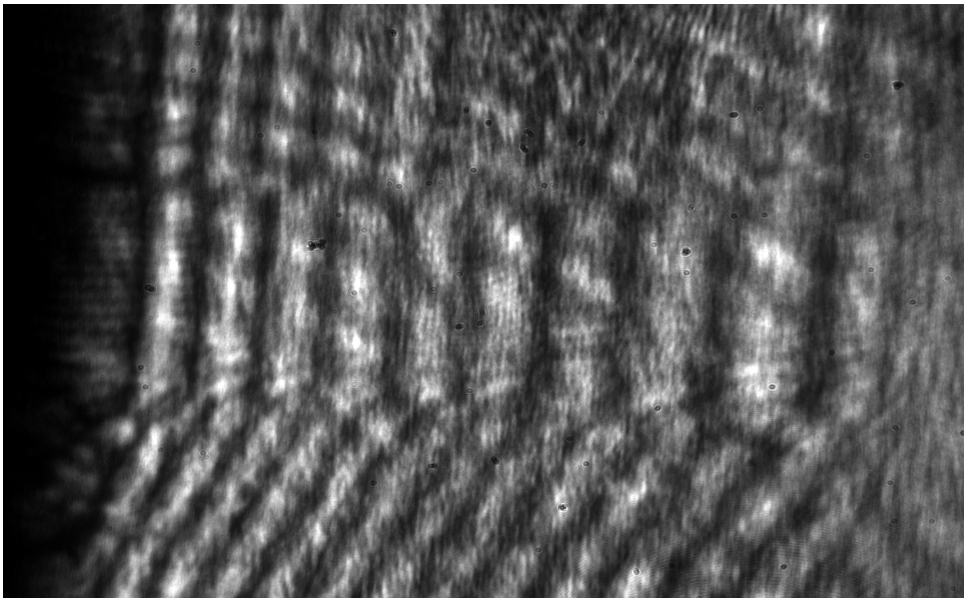


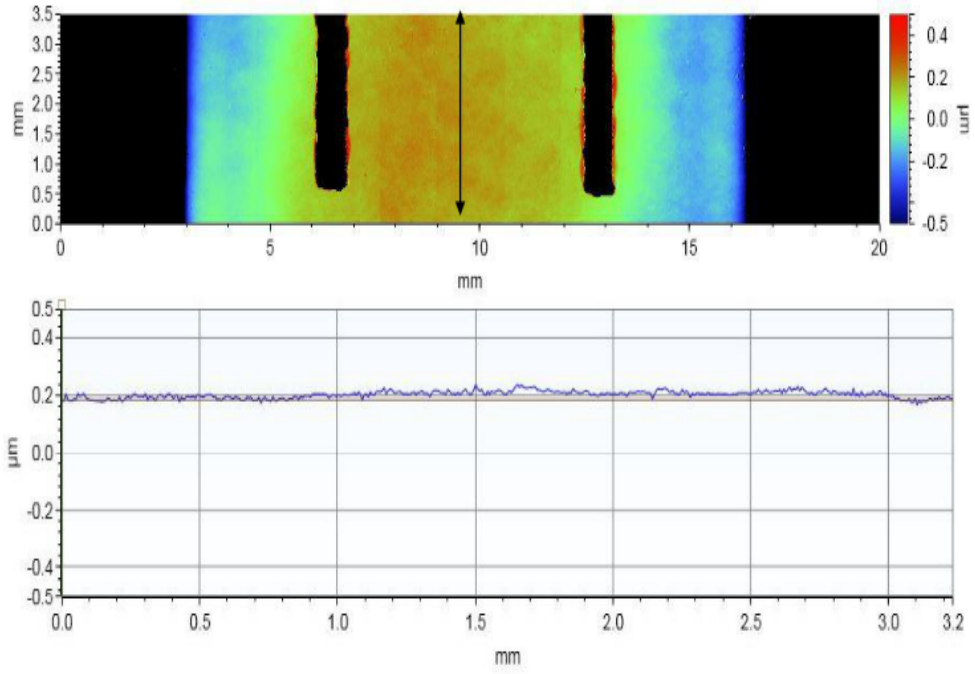
Figure 2.23: shows the recorded fringe pattern for the 1064 nm wavelength, for a 300 µm diamond channel, with a backing pressure of 100 mbar of hydrogen connected to a thyratron circuit being charged to 15 kV.

many layers of diamond the optical quality was not good enough to form a fringe pattern, whereas with a single sheet the optical quality of the diamond was good enough to form good quality fringes. Given the importance of the conductivity of the walls to the shape of the transverse electron density profile, it is hard to ascertain the guiding properties of this channel.

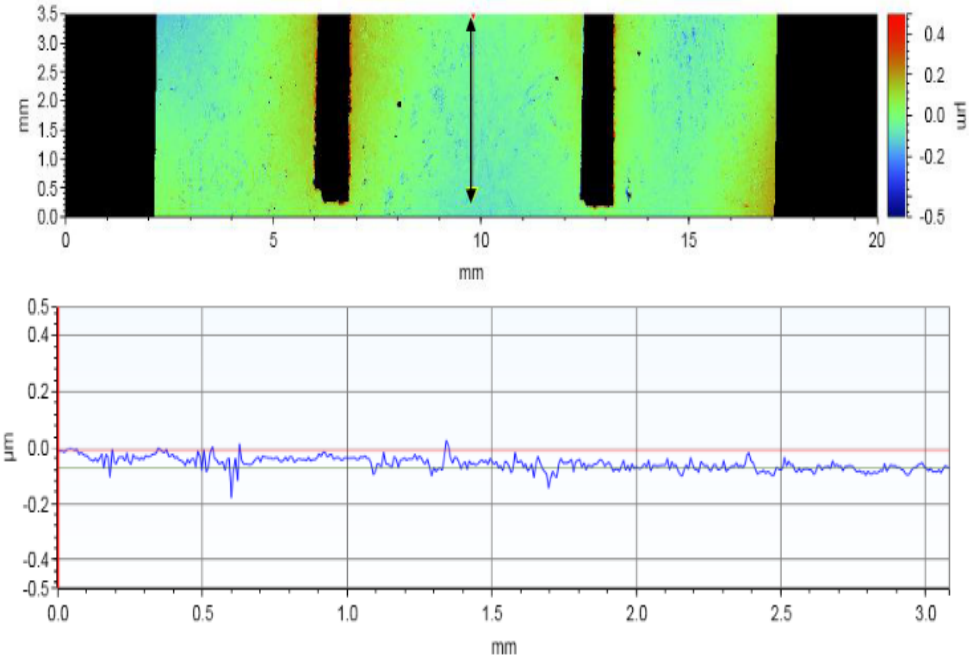
2.4.4.1 Lifetime Study of Diamond

The lifetime of the capillary employing sapphire and diamond walls was studied by measuring the flatness of the capillary plates before and after a large number of electrical discharges. The surface flatness of the material was measured using an optical interferometric profiler (Wyko NT 9300) which can scan surfaces across

a large area. The original surface flatness of the sapphire and diamond plates are in figure 2.24. In these images the gas slots may be used as a point of reference. It can be seen that the sapphire surface does not deviate by more than 1 µm and the diamond surface does not change by more than 3 µm, with a slight curve across the plate usually caused by the polishing process. Approximately 10 000 discharge pulses through 300 µm diameter capillaries filled with 100 mbar of hydrogen were taken. For this work, the thyratron circuit was used, with the charging capacitor charged to 15 kV; under these conditions the peak current was approximately 400 A for the diamond capillary and 600 A for the sapphire capillary. Measurements of the surface flatness were taken again after these discharge pulses, as is seen in figure 2.25. It is immediately clear that the diamond plates do not seem to have been damaged at all by the discharge. In contrast, with sapphire plates, the discharge removed approximately 0.7 µm of material from the centre of the capillary and deposited much of this near the edges of the spacer plates. This demonstrates that despite the significant increase in cost (the diamond plates were 100 times more expensive than the sapphire ones) there is a huge improvement in the lifetime of the diamond capillary.

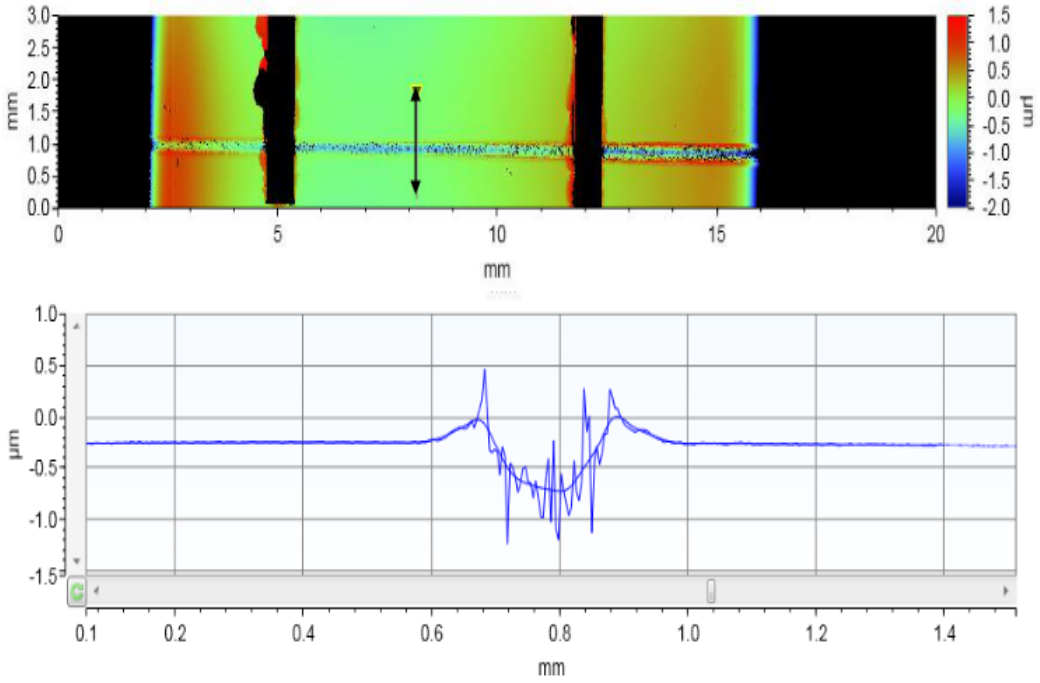


(a)

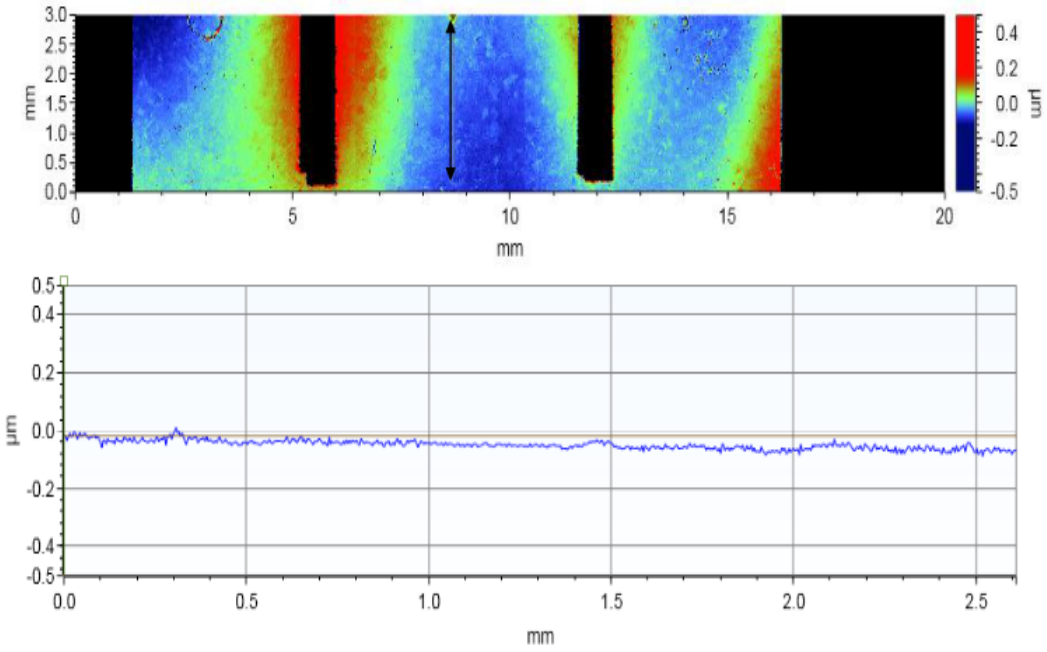


(b)

Figure 2.24: Measured surface profiles of the sapphire plate (2.24a) and diamond plate (2.24b) used to form capillary before 10 000 hydrogen-filled discharges. The black arrow represents the line out on the 3D surface was taken from.



(a)



(b)

Figure 2.25: Measured surface profiles of the sapphire plate (2.25a) and diamond plate (2.25b) used to form a capillary after 10 000 hydrogen-filled discharges. The black arrow represents the line out on the 3D surface was taken from.

2.5 Conclusion

Transverse interferometry was used to measure the evolution of the transverse electron density profile produced in gas-filled capillaries, and to compare the plasma channels formed by two types of discharge circuit. The electron density profile produced by the Compact Marx Bank is similar to that produced by the thyratron circuit and can be used to provide double the time window for guiding a matched spot size. By finding the integrated charge delivered by the Compact Marx Bank it is concluded that energy is continuously delivered to the system, causing the ionisation levels to steadily increase with no change in the guiding properties of the channel.

Transverse interferometry was also used to measure the electron density profile in helium-filled capillary discharges. It was found that a guiding channel very close to the predicted spot size was formed. Plasma channels formed in helium gas had a higher fractional ionisation than those produced with hydrogen gas fills. It seems reasonable to replace the use of hydrogen in experiments with helium as the same guiding can be achieved with a much less dangerous gas.

Transverse interferometry was attempted on capillaries formed in diamond plates. However, due to the poor optical quality the results were inconclusive. Upon performing a life-time study the diamond appears to perform much better against the sapphire in terms of damage after extensive use. This is however still not enough information to make the considerable extra investment (diamond is almost one hundred times the cost of sapphire) that would be required to change

to an all-diamond system, particularly when considering the high likelihood that laser damage due to diffraction or misalignment of the laser when driving a wakefield is high. More work in this area needs to be carried out to further investigate the plasma channel. This could be achieved by reducing the thickness of the diamond plates to 250 µm or by longitudinal interferometry as performed by Daniels *et al.*[53].

Chapter 3

Target Development

3.1 Introduction

It is important in laser wakefield experiments to carefully design the interaction between the laser pulse and the target, which plays a key role in the acceleration of the electrons. Here, two types of target were studied: gas-filled capillary discharge waveguides and gas cells.

For the former, an important issue is the flow of gas up to the point that the discharge is fired. This can lead to the formation of a plume of gas at the two ends of the capillary, and the formation of a longitudinally varying gas density within it. The existence of a plume near the capillary entrance could affect coupling of the incoming laser pulse into the capillary, and a longitudinal variation of gas density within the main capillary could affect the plasma channel which is formed. In order to understand these effects, fluid flow simulations were performed using computational fluid dynamic code OpenFOAM [54].

For a gas cell, the flow of the gas is also important as the starting conditions are assumed to be those that are experienced in the laser plasma interaction. Therefore, OpenFOAM was once again used to gain a further understanding and this time influence the design of the gas cell, such as to minimise the plume and create conditions for a flat longitudinal density profile.

The individual design considerations, influenced by the experiment, for both targets were taken into account and a Computer Aided Design (CAD) was drawn up before manufacturing the targets.

3.2 Gemini Target Design

The target used in the 2014 experiments was a gas-filled capillary discharge waveguide, with the capillary machined into a sapphire block. This allowed the guiding of high intensity laser pulses as discussed in section 1.5. The 2014 Gemini experiment required a very small focal spot, making the beam divergence large, and so required the laser to be focussed very closely to the entrance of the capillary to avoid the beam clipping the capillary walls. This meant that the gas slots machined into the sapphire also had to be very close to the entrance, to avoid gas density ramps. The waveguide housing also had to be adapted from the original design by Walker [55], not only to accommodate the laser beam profile but also to add a gas cell on to the side of the capillary discharge waveguide housing such that either target could be used.

3.2.1 Waveguide Design

To avoid the interaction of the laser pulse with the gas density ramp, the focal plane was placed beyond the gas inlets that fed the capillary channel. However, because of the large divergence of the beam used on the 2014 Gemini experiment, the focus could not be placed at the usual point of 4 mm inside the capillary. The solution was to machine the gas inlets closer to the capillary entrance but there were limitations to this caused by the waveguide housing. This was resolved by creating diagonal gas inlets, as shown in figure 3.1, such that the entrance of the gas inlets remained in the same position but the crossover with the capillary was much closer to the entrance.

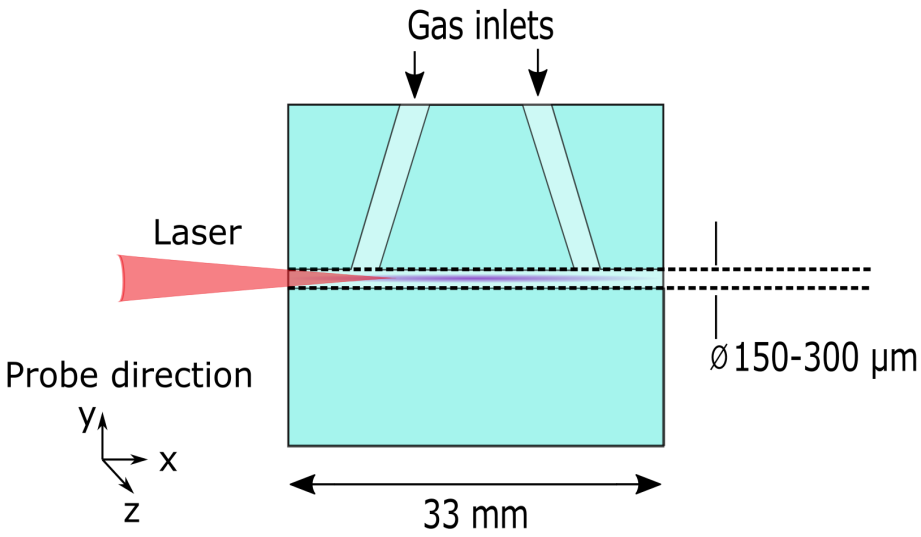
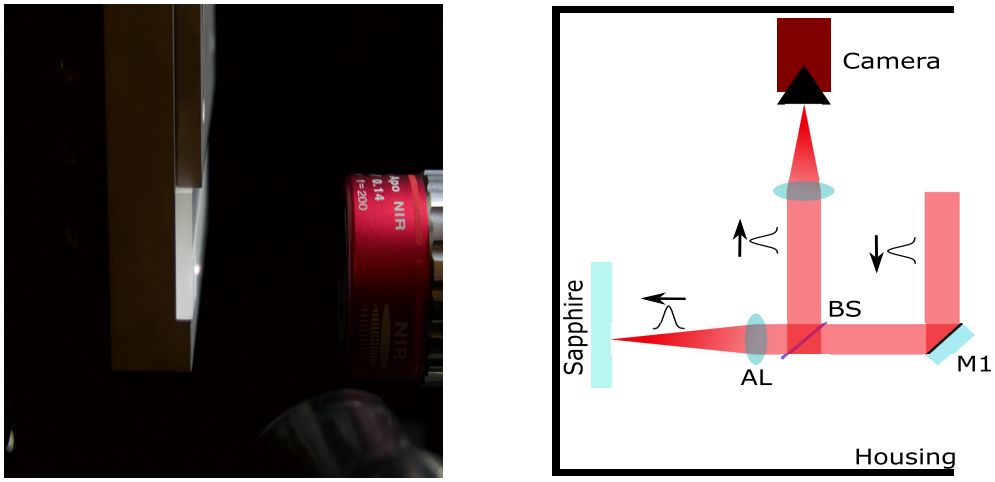


Figure 3.1: Schematic diagram showing the diagonal gas inlets and the capillary, laser machined into the sapphire blocks.

3.2.1.1 Laser Machining of the Sapphire

The gas inlets and capillary channels were laser machined into the sapphire blocks at Oxford using the system shown in figure 3.2b. This requires a laser system that delivers a pulse of < 1 ps, at a high repetition rate > 100 Hz. At these short pulse durations the laser pulse deposits its energy instantaneously and liberates electrons, via multi photon ionisation, from the surface of the sapphire which forms a plasma. This electron plasma then sets up a charge separation which causes the ions to follow, breaking their local bonds and leaving the bulk material; thus ablating only the area where the laser ionises the electrons. Due to the short (fs) nature of the laser pulses there is no heating of the sapphire and so thermal cracking to the sapphire was avoided [56] and smooth gas inlets and capillary channels were formed. To fulfil these requirements, a 400 µJ, at full energy, $<$ 100 fs and 1 kHz rep rate laser was used. This laser beam was focused using an achromatic lens (5X Mitutoyo Plan Apo NIR Infinity Corrected Objective) onto the sapphire block. The reflected light from the surface was then re-collimated by the achromatic lens and sent towards a CCD (PointGrey Flea 2: FL2-20S4M-C) with 1624 by 1224 pixels of dimension 4.4 µm. An achromatic lens system was used so that an external white light source could determine when the sapphire surface was in focus and show the outline of the sapphire, allowing for the relative alignment of the laser focus to the sapphire. The optical layout of the laser machining set up is shown in figure 3.2b.

The position of the sapphire stage was controlled by a multi-axis stage (ensemble motion), as shown in figure 3.2a. The stage is controlled by a script, written in an



(a) (b)

Figure 3.2: Photo of a sapphire block (figure 3.2a) being held in a specialised mount, moved by a multi-axis stage around a laser focus formed by a microscope objective (the red object on the right). Also seen is a small plasma ball on the sapphire surface that is ablating the sapphire. Figure 3.2b shows the optical layout of the machining set up. Here, AL is the achromatic lens, M1 is a mirror and BS the beam splitter.

adapted form of the computing language BASIC. These scripts were generated using a LabView program, originally written by previous generations of graduate and postdoctoral students, that describes the dimensions of the sapphire and desired capillary channel/gas inlets. This was a very versatile set-up which could be used to create almost any gas inlets or capillary channel that can be imagined and so the LabView code was edited, by the author, to produce diagonal gas inlets to meet the requirements of the experiment.

3.2.2 Waveguide Housing

3.2.2.1 Design Considerations

Targets which require a pre-formed plasma channel generate complex design considerations for the waveguide housing, as part of the infrastructure required to form and retain the plasma channel. The design constraints which were considered when setting out to build such a target are outlined below.

A small target profile is required as the movement of the waveguide housing is limited by the range of motion of the multi-axis stage on which the waveguide is mounted; this range is typically 50 mm. The stage is used to align the capillary waveguide to the laser axis of propagation. It is also used to drive the waveguide housing completely out of the path of the laser allowing the beam to be diagnosed without being altered by the capillary channel.

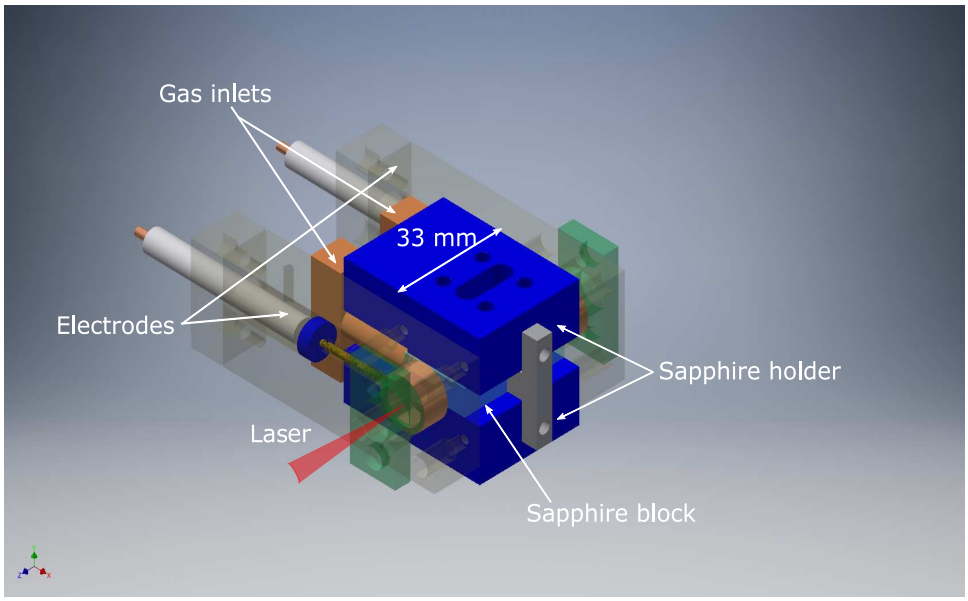
The waveguide housing design should be robust and the parts should not be fragile such that they break easily or that they require specialist fixing mechanisms. The waveguide housing should have as few small parts as possible, making them easy to handle. A typical experiment would involve a study of different capillary lengths and diameters; whilst it would be possible to build a different housing for each of these, it would be advantageous to keep as much of the housing as possible the same without changing the location of the front face and therefore maintain the interaction point of the laser focus and the entrance of the capillary discharge waveguide.

The capillary discharge waveguide requires electrodes at each end, electrically isolated so as to allow a discharge current to flow along the capillary, but preventing discharge around the sapphire block or to the chamber wall. The capillary waveguide has to support a given spot size, propagating it over many Rayleigh ranges, as was described and set out in section 2.3.5. The capillary waveguide channel must be reusable thousands of times.

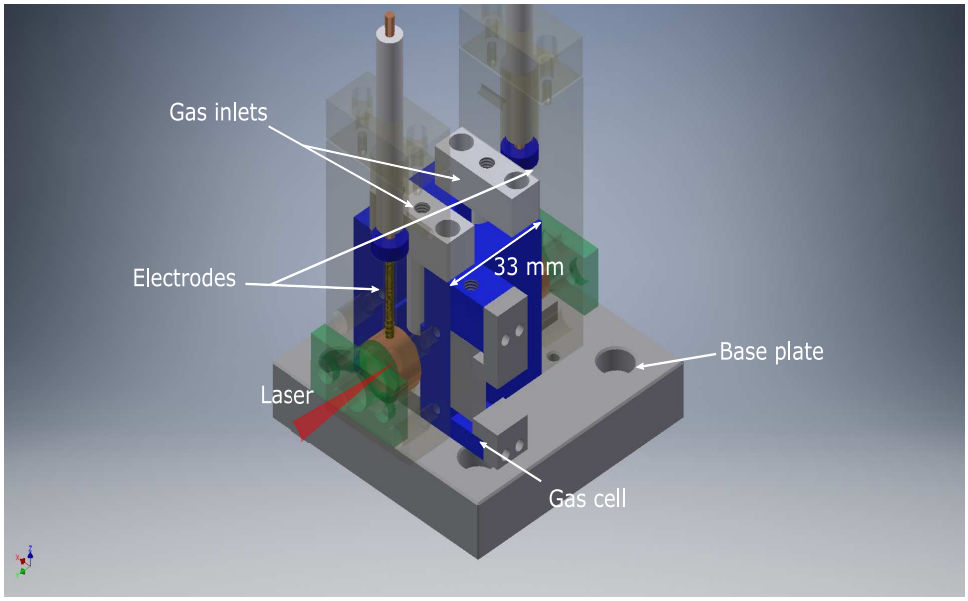
3.2.2.2 Implementation

Bearing these design considerations in mind, Auto CAD Inventor was used to create a virtual design of the waveguide housing. Auto CAD allows great freedom of design and instant changes, as well as allowing the production of technical drawings and machine readable files. The new design was based on an earlier design by previous group member Andy Walker. To meet the requirements of a parallel gas cell to the capillary discharge waveguide used in this experiment, Walker's initial design was adapted, as shown in figure 3.3. This involved the addition of a C shaped holder being attached to the original waveguide housing, the top of which having a hole to feed in gas, for two short 2 mm sapphire plates that are to be used to form the gas cell, these were restrained by two L brackets shown in gray in figure 3.3b.

In both the original and new design the infrastructure was made mainly from Clear Cast Acrylic to electrically isolate the electrodes avoiding electrical breakdown. These were broken up into a number of common parts that allowed the length of the capillary to be changed easily. The small profile was achieved, by making these parts narrow in the laser propagation direction but relatively thick



(a)



(b)

Figure 3.3: Figure 3.3a shows the original CAD drawing of the housing for the capillary discharge waveguide. Figure 3.3b shows the improved version of the capillary discharge waveguide housing that was used in the 2014 Gemini experiments.

so as to make them robust and of an appreciable size. Metal wire thread inserts in the Acrylic waveguide housing were used to reduce wear, because it was found previously that not having thread inserts could lead to bolts shearing and becoming lodged in the threads. A standard bolt length and size (M3) was maintained.

However, some key changes to the Walker design were made. Originally, the sapphire was held in place by a single piece of plastic and then the waveguide housing was attached to a magnetic base plate. This design was changed by adding a plastic base plate, as shown in figure 3.4 part 2, allowing the entrance of the capillary waveguide to be placed in approximately the same position each time, regardless of the length of the sapphire.

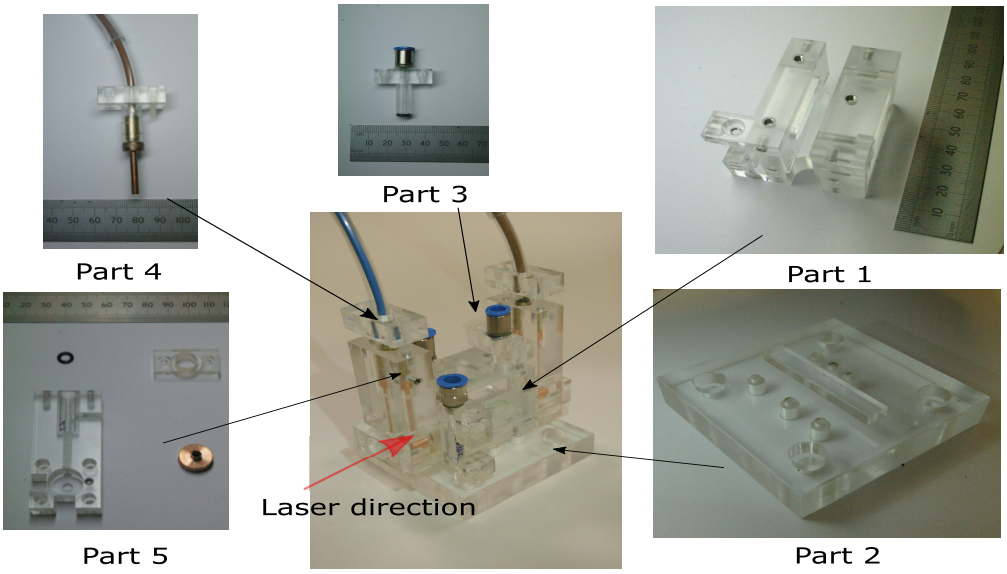


Figure 3.4: The target used on the 2014 Gemini experiment. Here, part 1 is the central structure that holds the sapphire, which is then placed onto part 2 the plastic base plate, with part 3 being attached at the top and used to deliver the gas to the capillary and part 4, being placed inside part 5, which is then attached to part 1 and is used to supply the electrical discharge.

The new waveguide design is shown assembled, together with its components, in figure 3.4. Figure 3.4 part 1, shows the additional gas cell attached to the side of the capillary housing. This was used to mount two sapphire plates that were 2 mm in length, with a large diameter capillary machined into it, of the order of > 400 µm and a single gas inlet.

3.2.2.3 Experimental Improvements

It was noted during the 2013 ASTRA experiments that it was difficult to replace the pins with their nut and bolt design. And so a new design was implemented, to replace this nut and bolt with a brass threaded sleeve and a copper thread on the pin so that the discharge cables could be removed easily, which made the system much easier to work with. The original design is seen on the far left of figure 3.5 and the improved version of the pin is seen on the far right.

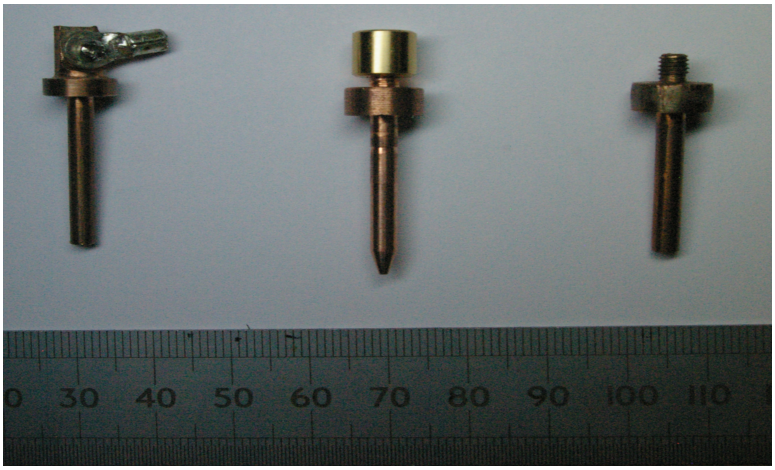


Figure 3.5: showing the different pin designs. Left, is the original pin. Middle, is an experimental pin design with a pointed end, also seen is the brass fixing that connects to the electrical cable of the discharge. Right, shows the actual copper pin design used on the 2014 Gemini experiment, with the original flat end. The pin is attached using the brass fixing which is not shown here.

An attempt was made to remove the copper sleeve, shown in figure 3.4 part 5, that the copper pin sits against, by making a pointed end to the pin, as can be seen on the pin in the centre of figure 3.5. The idea was to strike the plasma directly from the tip of this pin, but it was found that this was difficult to do, as there was not enough gas around the end of the pin to form an easy path for the discharge.

During the 2014 Gemini experiment the beam layout was changed. This required re-designing the waveguide housing to meet this new challenge whilst still retaining the original design consideration. This meant that parts 4 and 5 in figure 3.4 now intruded on the beam line and so a small square gap had to be made in part 5 so that it could be rotated by 90 degrees to sit on the plastic base plate, part 2, to be clear of obstructing the beam.

It also became apparent on the 2014 Gemini experiment that it is important to be able to locate the front of the capillary waveguide with respect to the laser focus. A way of doing this is to image a point on the waveguide housing whose position, relative to the entrance of the capillary waveguide, is reliably known. In order to achieve this, an additional piece was made, shown in figure 3.6, which replaced part 4/5 on the waveguide housing. By imaging the laser focal spot and then finding the point where the razor blade is sharply in focus, the position of the capillary waveguide with respect to laser focus can be found.

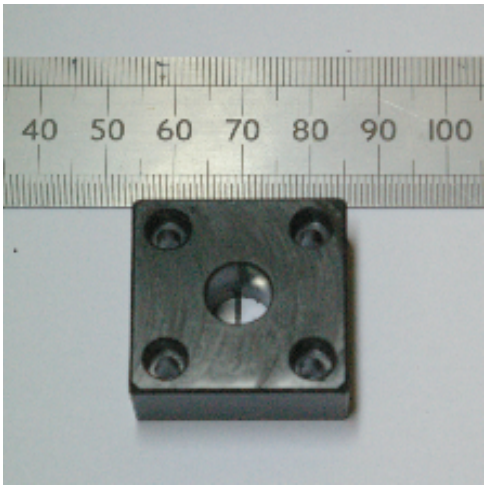
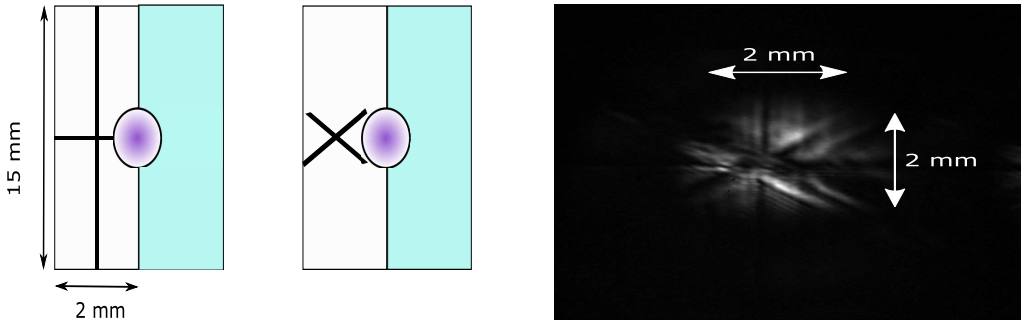


Figure 3.6: Knife edge holder used to align the entrance of the capillary to the laser focus.

3.2.3 Alignment Technique

The alignment process itself is non-trivial; in order to produce a reliable method of aligning the capillary waveguide to the laser axis, a '+' and a 'x' were machined into the ends of the sapphire block. The '+' was machined on the front surface, i.e. upstream of the laser focus point, and the 'x' was machined on the back surface of the sapphire face. An example of these marks can be seen in figure 3.7. By machining these marks relative to the capillary entrance and exit, it was possible to align to the axis of the laser so that it could be determined where the capillary was, relative to the '+' and 'x', and overlap these two marks in order to easily align the capillary to the laser axis. It was found, however, that these marks were difficult to see, especially once the beam became restricted due to the waveguide housing. It also became difficult to implement for capillaries longer than 15 mm, as the the image of the '+'/'x' mark degraded as the light scattered



(a) (b)

Figure 3.7: Figure 3.7a shows the ideal placements of the etched + and x alignment marks to be made by the machine rig laser at each end of the same sapphire block. Figure 3.7b shows an image taken of the x and + using an 800 nm wavelength laser pulse through 15 mm of sapphire.

through the sapphire block and so became difficult to resolve.

An alternative approach was based on a pair of wire cross-hairs mounted on rectangular frames fixed to the waveguide housing. However, it was found that this method was difficult to implement at the laser facility and actually much more fiddly than anticipated with the extra optics that were downstream. The provision of a system for aiding the alignment of the capillary remains to be developed.

3.3 OpenFOAM

3.3.1 Introduction

Knowing the distribution of gas density within the target is very important for laser wakefield acceleration experiments. In the case of capillary discharge waveguides, it is a key parameter determining the distribution of the electron density

profile and hence the spot size that can be supported. The gas pressure is also directly linked to the electron plasma density and hence the plasma wavelength, which determines the pulse duration of the laser for matched conditions.

To better understand the gas distribution and hence the electron density, two-dimensional, computational fluid dynamics software called OpenFOAM V2.1 was employed. This was built on the work of a previous group member Wolf Rittershofer [57]. OpenFOAM takes an initial set of conditions 'and assumptions' and models how the gas particles would propagate through a specified geometry as time progresses. At any time slice, the temperature and pressure of the gas is given and from the ideal gas equation the electron number density can be calculated.

The original work carried out by Rittershofer [57] included a number of different checks of the validity of the simulations which will be outlined in section 3.3.2. These simulations were also checked against Raman scattering measurements and the simulations were found to be within the acceptable experimental error of 3 % for the Raman scattering results.

Using this technique, a wide range of simulation parameters were run to quickly establish conditions that met the requirements for the 2014 Gemini and 2015 ASTRA experiments; this helped to set limitations on the target design.

3.3.2 Simulation Parameters

Computational fluid dynamics can be used in a wide range of applications. The gas molecules in these fluid dynamic simulations are treated as a continuous averaged mass distribution, known as the continuation approximation. The approximation is only valid if the mean free path λ of the particles is small compared to the physical size of structure L. This relationship can be expressed by the Kundsen number K_n,

$$K_n = \frac{\lambda}{L} \approx \frac{108}{P[mbar]L[\mu m]} \tag{3.1}$$

if K_n is < 0.1 then the continuation approximation is still valid; above this value a different approach has to be taken, as shown in [58]. For the experiments presented here this regime is generally true but for very low pressure (<5 mbar) and small scale lengths λ (<100 µm) can become comparable to the dimensions of the structure in which the gas flows.

The Navier-Stokes equations were used to solve the fluid computational dynamic problem, a detailed explanation of these equations is given in Guti *et al.* [59]. The OpenFOAM solver chosen was sonicFoam [54] as it can solve the Navier-Stokes equations for compressible supersonic gas flows. The boundary of the model, between the gas in the centre of the target, which is at a constant pressure, and the exit of the target, that is at vacuum, produces conditions where supersonic velocities of the fluid are reached, necessitating a solver that can model these conditions.

Because of these boundary conditions in the problem, the fluid experiences two different types of flow: laminar flow, which is steady; and turbulent flow, where fluid flows with chaotic changes, causing the formation of eddies. The type of flow is determined by the Reynolds number [60], which is a measure of the inertial force of the fluid to the viscous forces. For this system, turbulent flow is seen at the boundary between the vacuum and target exit. Due to the difficulty of modelling the different flow dynamics, the $k-\omega$ shear stress transport (SST) model, which combines different models to achieve the best results, was used to approximate the turbulence. This model is based on the Reynolds-averaged Navier-Stokes equation and used in situations where large pressure gradients exist.

The thermodynamic modelling of the system was undertaken using ePsiThermo [54], a general thermophysical model based on internal energy U and compressibility ψ of the gas. The gas was assumed to be a pure ideal gas which was represented by using the pureMixture and perfectGas models in OpenFOAM. Changes in specific heat are negligible in these experiments so the simple standard model hPsiThermo was used, which calculates the specific heat of the system using enthalpy h and compressibility ψ.

Two different models were used for the transport. In regions where the flow was non-turbulent the viscosity was modelled by constTransport, a model which keeps the viscosity of the gas constant. However, for regions where the flow began to become turbulent the sutherlandTransport model was used to derive the viscosity, this model calculates the viscosity of an ideal gas as a function of temperature for each time step.

The condition for convergence of the simulation was set by the Courant Number [54],

$$Co = \frac{\delta t \mid \mathbf{U} \mid}{\delta x} \tag{3.2}$$

where δt is the time step, $\mathbf{U}$ is the fluid velocity in the cell and δx is the cell size in the direction of the velocity. The mean and maximum Courant Number are calculated at each time step and stop the simulation if this value goes above 1.

In previous modelling of the capillaries by Rittershofer [57], it was assumed that the walls that form the capillary are not perfectly smooth. This wall roughness can be a model parameter in OpenFOAM, where it was assumed that the wall had sand like particulates of the size 1 - 10 µm. Rittershofer showed that for the roughness of the walls in this experiment there was little effect on the outcome and so the modelling presented here is done without this additional parameter.

3.3.3 Geometry Parameters

OpenFOAM takes a series of files that are used to define starting parameters and the shape of the model and combines them with the boundary conditions that are to be simulated. The model layout is broken down into a mesh grid that is defined by the user in a file called BlockMesh. This file contains a list of co-ordinates detailing the internal and external boundaries of the problem. This can make it very hard to create objects that are more complicated than just a box or pipe with a change in diameter. Therefore a visualisation code was written in Mathematica by Wolf Rittershofer and allows for the visualisation of the model that is being

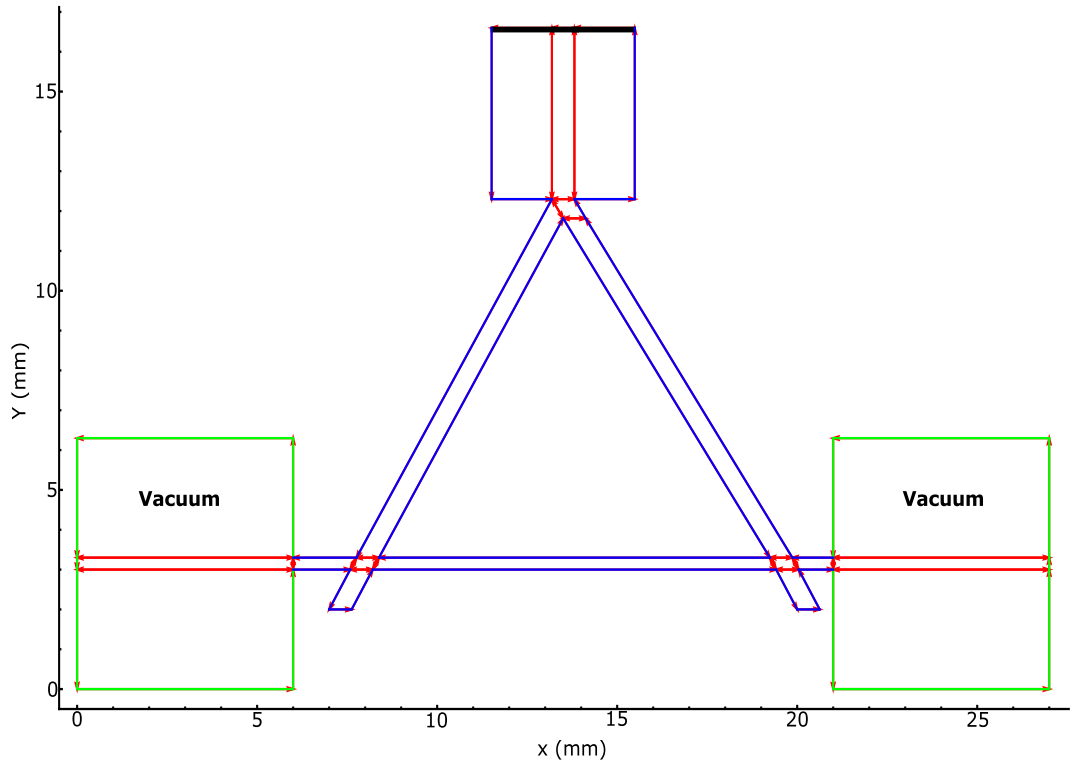


Figure 3.8: Layout of the grid that was used to form the blockMesh file using OpenFOAM. Where the black line represents the gas input boundary; green lines represent the vacuum boundary; blue lines represent a material wall and red lines represent internal boundary walls.

designed, an example of which is shown in figure 3.8. The visualisation software allowed the boundary conditions to be easily checked and much more complicated shapes to be designed than would otherwise be achievable. The program also highlighted key parameters such as the pressure to feed into the model and the number of time steps to be used, and wrote all of the files out in a format that was compatible with the OpenFOAM software, making it very easy to edit designs and change parameters for a large number of different models.

Using the visualisation software, models of the capillary waveguide were made. The 4 mm diameter gas pipe feeding the capillary was shortened to reduce the computational demands required, as, typically, this would be 2 - 3 m long before it reached the gas board which supplied the targets with a constant gas backing pressure. The gas pipe was connected to the entrance of the 625 µm wide gas inlets and delivered gas to the capillary. In contrast to previous work, the author modelled not just a simple joint between these two elements but allowed for the gas inlets to continue on past the capillary by 1 mm, as would be true in the actual experiments, to see if the gas that stagnates in this region has any effect on the gas profile in the capillary. Various capillary diameters from 200 µm to 300 µm and of 15 mm in length were modelled. The boxes at the end of each of these capillaries were outflow boxes which effectively represented the evacuated space.

The simulations were run until a steady state of the gas flow was achieved. This is close to the reality of the experiment, in which the gas to the target is pulsed but left open, for approximately two seconds, to ensure that a steady flow rate is reached before the interaction with the laser pulse.

OpenFOAM is capable of being used to model both 3D and 2D structures. The modelling of 3D structures is a lot more computationally expensive and it has been found by Rittershofer [57] that the results in the 2D case are nearly identical, apart from the outflow region, which differs in some parts by almost 5 % and so for this work only 2D model simulations were performed as the outflow regions are not important here.

3.3.4 Results

3.3.4.1 2014 Gemini Capillary Waveguide

The gas flow into the 2014 Gemini capillary waveguide was modelled before the experiment, using the geometry shown in figure 3.8, to try and ensure that the new geometry of the capillary did not have an effect on the gas flow that was delivered to the capillary and hence have unexpected consequences for the electron density profile that was formed. Figure 3.9 shows the horizontal lineouts of the modelling results, taken along the top and bottom of the capillary next to the wall and a lineout from the centre of the capillary. Here it can be seen that the gas density profile is very uniform and that towards the exit of the capillary a cone-like shape is formed. The profile of the of the gas density is the same as those modelled previously by Rittershofer [57] in which two channels with the same gas pressure led to a uniform gas density profile.

Where the gas input intersected with the capillary, as in this simulation, there is little density perturbation, whereas when Rittershofer modelled a standard capillary, a slight increase in gas density was observed. This increase was assumed to be caused by the gas rebounding from the lower capillary wall. This effect, whilst still present in this simulation, could clearly be minimised by including gas inlets in the model that allow gas to overshoot the capillary, thus modelling the gas density profile more accurately.

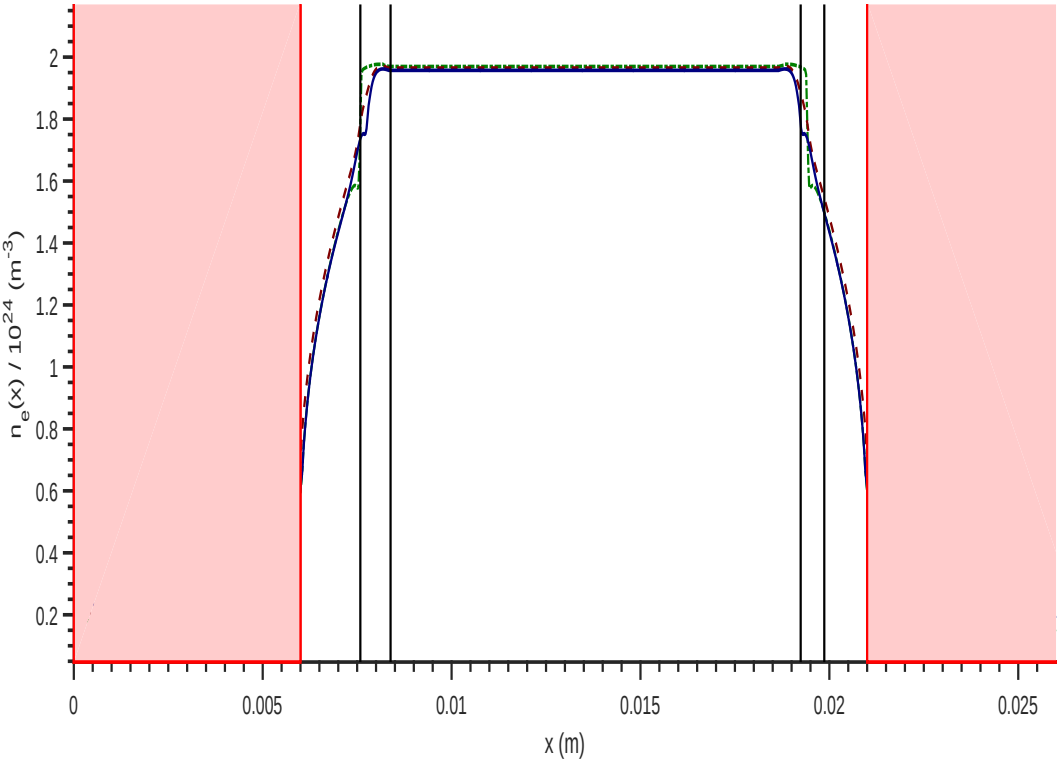


Figure 3.9: The steady-state longitudinal profile of hydrogen (H_2) electron number density for the 2014 Gemini Capillary Waveguide model. Here, the vertical black lines represent the gas inlet region; the red box represents the vacuum space; the green dashed dot line represents the density at the bottom of the capillary; the red dashed line represents the density at the centre of the capillary and the blue solid line represents the density at the top of the capillary.

3.3.4.2 2015 ASTRA Gas Cell

For the 2015 ASTRA gas cell, OpenFOAM was used in parallel with CAD software to improve upon the design ideas by modelling the physical density profiles. Here, a brief account of the model will be given but section 3.4 will give a full account of the design criteria and reasoning for this choice of target. The 2015 ASTRA gas cell is very different from the 2014 Gemini Capillary Waveguide; at Gemini, the laser pulses were to be guided in a capillary discharge waveguide; in

2015 ASTRA, however, the interaction length of the laser with the target was only required to be 4 mm, the same length as the Rayleigh range of the laser pulse. As a consequence, it was not necessary to guide the laser pulse, and instead a simple gas cell could be employed as shown in figure 3.10. This is a pure gas target, where the laser comes in from the left, interacts with a small region of gas and then exits from the target on the right. The target is large, compared to the interaction region, because of the constraints on the engineering, due to the nature of the interaction to be studied, which is further explained in chapter 4. The gas in the interaction region needed to be a uniform density, and its relation to the pressure in the feed pipe had to be fully characterised as this was critical to understanding the results of the 2015 ASTRA experiment.

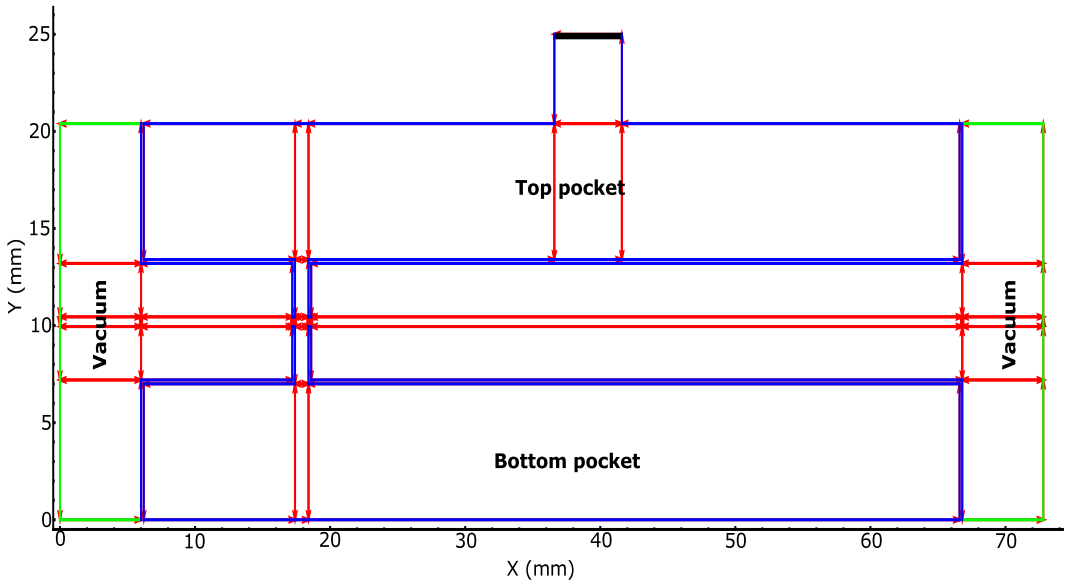


Figure 3.10: Layout of the grid that was used to form the blockMesh file using OpenFOAM. Where the black line represents the input gas boundary; green lines represent the vacuum boundary; blue lines represent a material wall and red lines represent internal boundary walls.

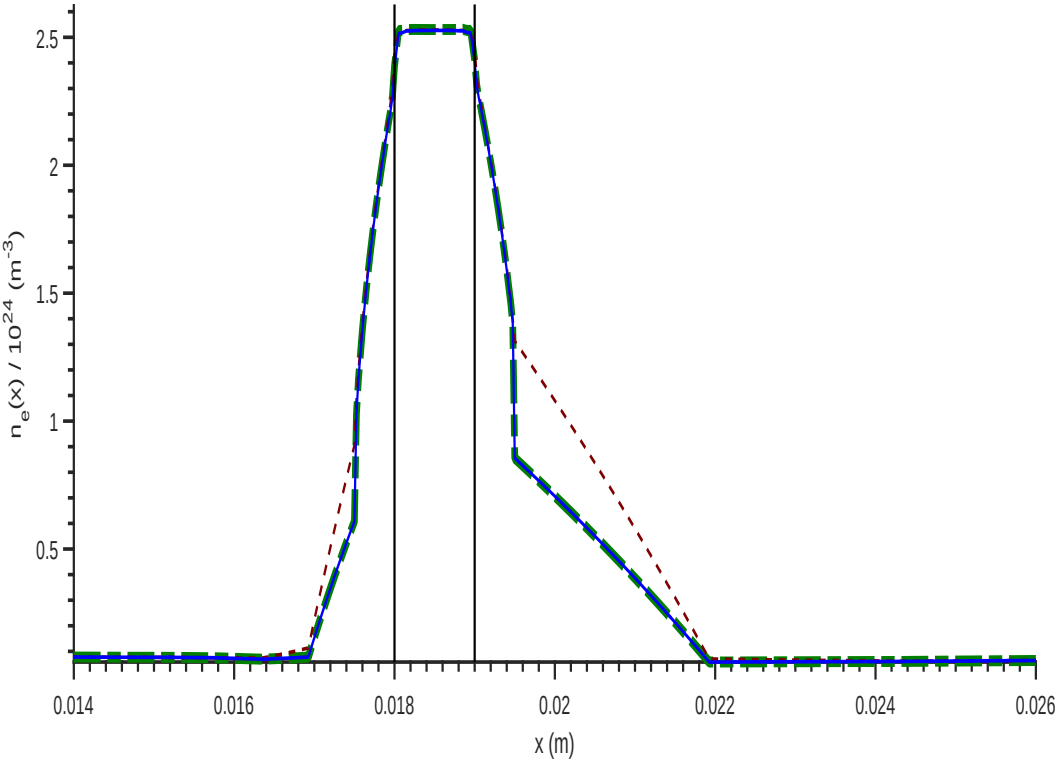


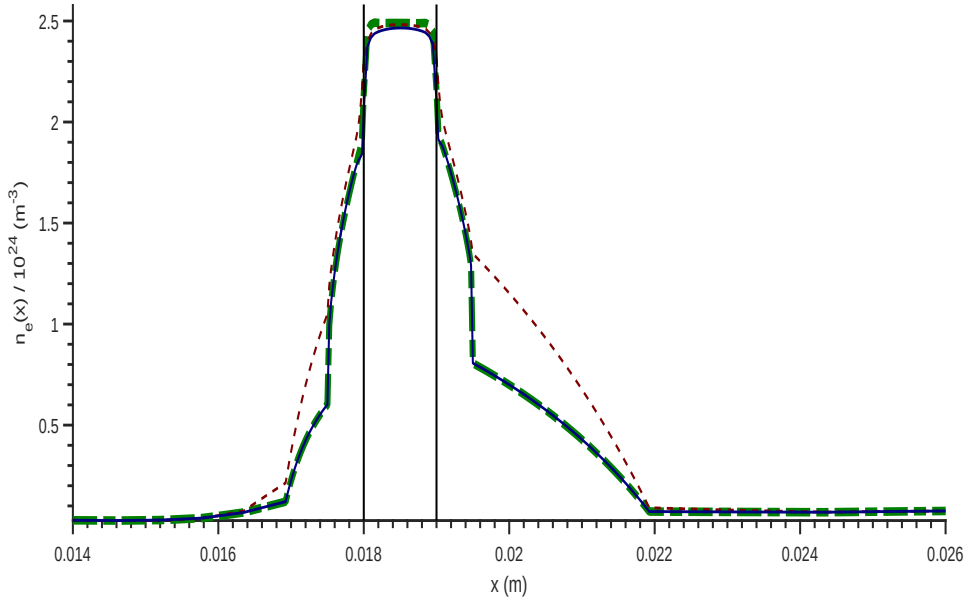
Figure 3.11: The steady-state longitudinal profile of hydrogen (H_2) electron number density for the 2015 ASTRA gas cell model produced by the OpenFOAM software. Here the vertical black lines represent the gas inlet region; the green dot dashed line represents the density at the bottom of the capillary; the red dashed line represents the density at the centre of the capillary and the blue solid line represents the density at the top of the capillary.

Figure 3.11, shows the gas profile for the top, middle and bottom of the interaction region. As for the capillary waveguide, it is seen that the density is very uniform in the central region, and that plumes of gas emerge from each end. A range 50 to 100 mbar of input pressures was explored; it was found that the density of the central region varied linearly with the fill pressure, and that the longitudinal profiles of the plumes were independent of pressure.

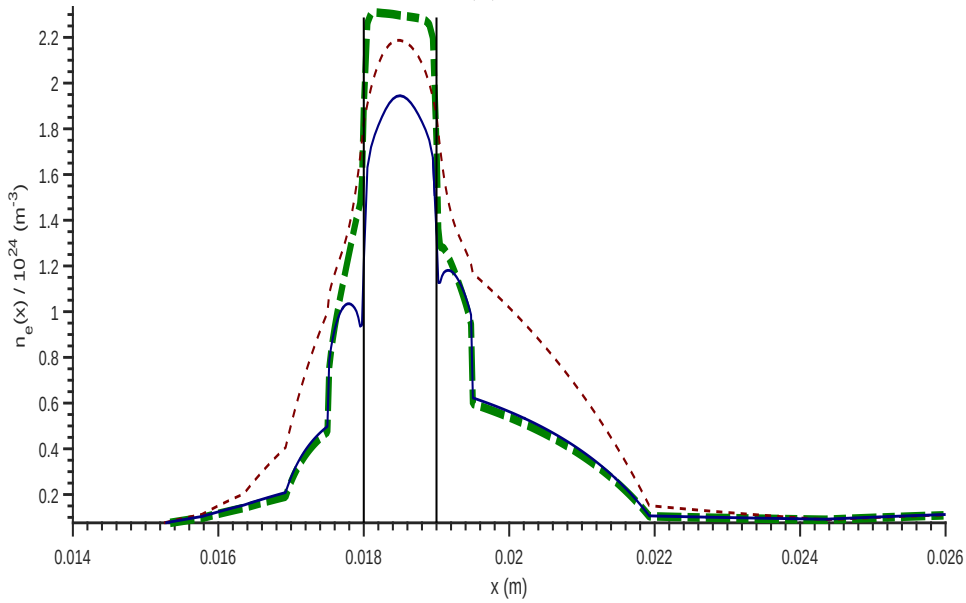
It was then decided to vary the size of the pinhole where the gas escapes from the centre of the target to the vacuum space, similar in practice to changing the size of the capillary diameter. It was found that up to a pinhole diameter of 0.5 mm, the central density remained uniform and that the gas ramps got a little steeper but remained very similar in shape, as shown in figure 3.12a. Above 0.5 mm, the uniform region begins to display a curved density profile longitudinally and the gas ramps at both exits become both wider and longer, as shown in figure 3.12b.

Finally, it was decided to vary the thickness of the pinholes, in effect changing some of the dynamics of the interaction between the vacuum and the steady state, as can be seen in figure 3.13. This had very little effect on the gas profile created or the diameter of the pinhole that could be tolerated. For this reason, the thickness of the pinholes that are used were made thinner to 200 µm, rather than 500 µm as had originally been planned.

It was noted that the simulations took a long time to achieve a steadystate because the bottom pocket is isolated from the top pocket, as shown in figure 3.10, the bottom pocket had to be filled with gas before equilibrium was achieved. Of course in the actual target, the bottom pocket would not be isolated from the top pocket. Therefore, it was decided to add a second gas inlet to the bottom pocket and thus reduce the amount of computational time taken to reach a steady state. Comparing this model against the previous model it was found that the steady state scenarios were very similar.

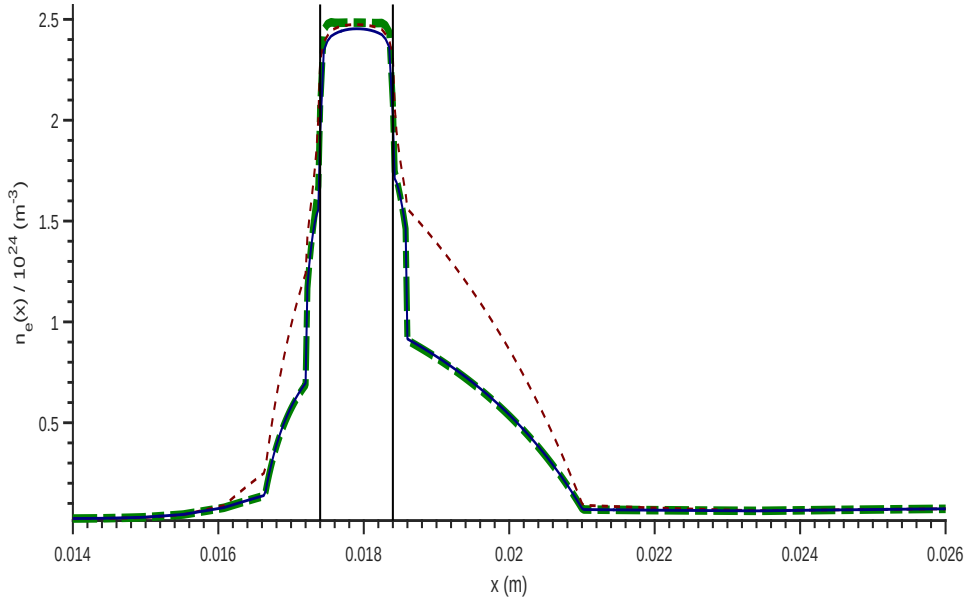


(a)

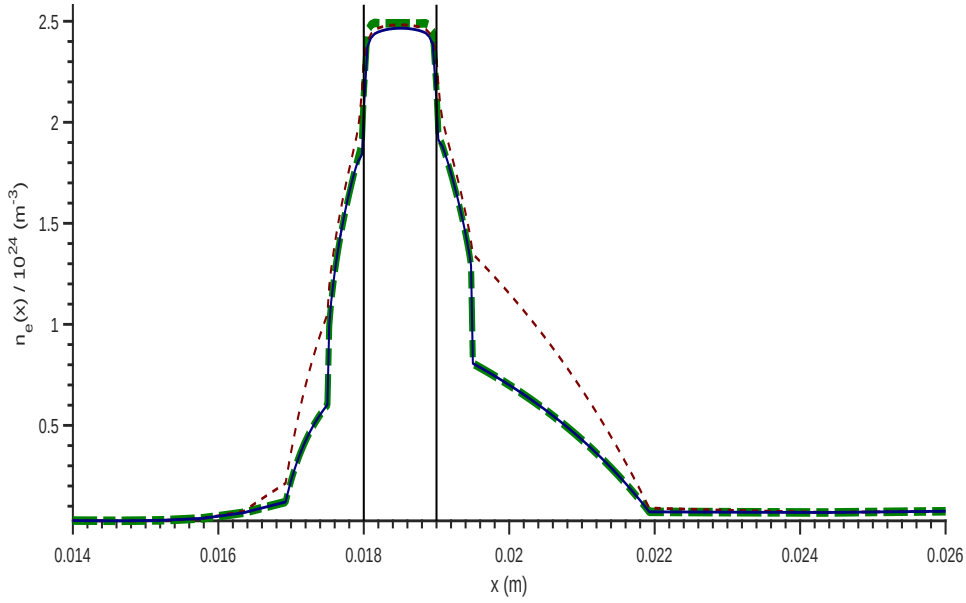


(b)

Figure 3.12: The steady-state longitudinal profile of hydrogen (H_2) electron number density for the 2015 ASTRA gas cell model produced by the OpenFOAM software. Figure 3.12a has a 200 µm pinhole diameter, while figure 3.12b has a 500 µm pinhole diameter. Here the vertical black lines represent the gas inlet region, the green dot dashed line represent the density at the bottom of the capillary, the red dashed line represents the density at the centre of the capillary and the blue solid line represents the density at the top of the capillary.



(a)



(b)

Figure 3.13: The steady-state longitudinal profile of hydrogen H_2 electron number density for the 2015 ASTRA gas cell model produced by the OpenFOAM software with a pinhole diameter of 200 µm, and variable thickness. Figure 3.13a is a 200 µm thick pinhole and figure 3.13b is a 500 µm thick pinhole. Here the vertical black lines represent the gas inlet region, the green dashed dot line represent the density at the bottom of the capillary, the red dashed line represents the density at the centre of the capillary and the blue solid line represents the density at the top of the capillary.

3.3.5 Conclusion

OpenFOAM was used very successfully to help predict the initial longitudinal density profiles for capillary and gas cell targets. The speed and simplicity of creating these models, allowed for a large parameter space to be explored quickly and efficiently with a great deal of confidence.

The parameters of the 2015 ASTRA gas cell model influenced the design choice of key components and also eliminated any doubt as to the conditions of the gas target that was being used. This gave extra credibility to the experiments, as discussed in chapter 4, and allowed predictions of the experiment to be made with some confidence.

3.4 ASTRA Target Design

3.4.1 Design Considerations

The target design to be used on the 2015 ASTRA experiment was a gas cell. A gas cell was chosen rather than a capillary waveguide to simplify the experiment. The key requirements of the cell were that it should have a variable interaction region (1-4 mm) of flat gas density profile.

It was also required that the overall dimensions of the cell were small so that it could be moved in and out of the laser beam by a multi-axis stage. It was necessary that the laser beam did not clip the gas cell and that the gas cell could be removed entirely from the path of the laser beam to allow for the alignment

of laser diagnostics further downstream. It was desirable that the cell should be robust with as few small or delicate parts as possible. In addition, the gas cell was designed to require very few bespoke fixtures to hold it together, as these are time consuming to have manufactured and are also more difficult to replace during in the experiment. The gas cell had to be resilient, such that it could be used for many shots before it would be necessary to replace parts.

Applying the results from the OpenFOAM simulations it became apparent that in order to maintain a flat gas profile, the openings to the vacuum should have a diameter of approximately 0.5 mm.

3.4.2 Implementation

With these design considerations in mind, the CAD drawing package Auto CAD Inventor was used to draw up the design as shown in figure 3.14. The design con-

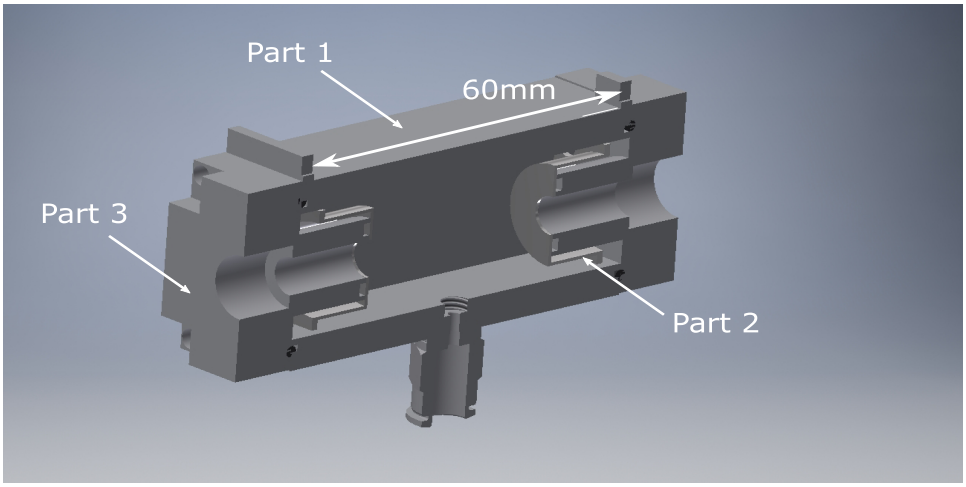


Figure 3.14: Cut-away view of the CAD drawing of the ASTRA gas cell. The gas cell is shown in its assembled form showing how the parts fit together.

sists of a hollow rectangular aluminium block as is shown in part 1, figure 3.15. Along the long length of the rectangle face, two sapphire windows were installed to allow the laser/gas interaction to be viewed. At either end, a metal lip was used as a feature to locate the longitudinal position of the gas cell, relative to the laser focus, in a similar way to the cross-wires described in section 3.2.3. The end faces included a rubber o-ring to seal the other parts to the main body. On the underside of part 1, a 5 mm push-in connector (Festo) gas fitting was attached, to supply gas to the target. Finally, four thin metal feet were used to attach the gas cell to the Hexapod control stage.

Parts 2 & 3, shown in figure 3.15, were used to vary the length of gas interaction with the laser pulse. Part 2, which closely resembles a 'top hat' with a hole cut out of the top, was designed to fit over part 3. Two of these pieces were then assembled and attached to either end of part 1 with the square rubber o-rings forming a seal. The 'top hat' part furthest upstream of the laser focal point was a fixed short length. The second piece, downstream from the laser focal point, varied in length, allowing for a change in the interaction length from 1 mm to 4 mm.

Parts 2 & 3 were also designed to hold thin foils which the ASTRA laser would drill through to form a pinhole, allowing for easy alignment of the laser axis while keeping the vacuum aperture small. Part 4, in figure 3.15, shows the foils that were made. Over 100 stainless steel, 200 µm thick foils were made, such that these could be replaced on a daily basis if necessary. Initially, these foils were 250 µm thick but were difficult for the laser to machine through and so later batches

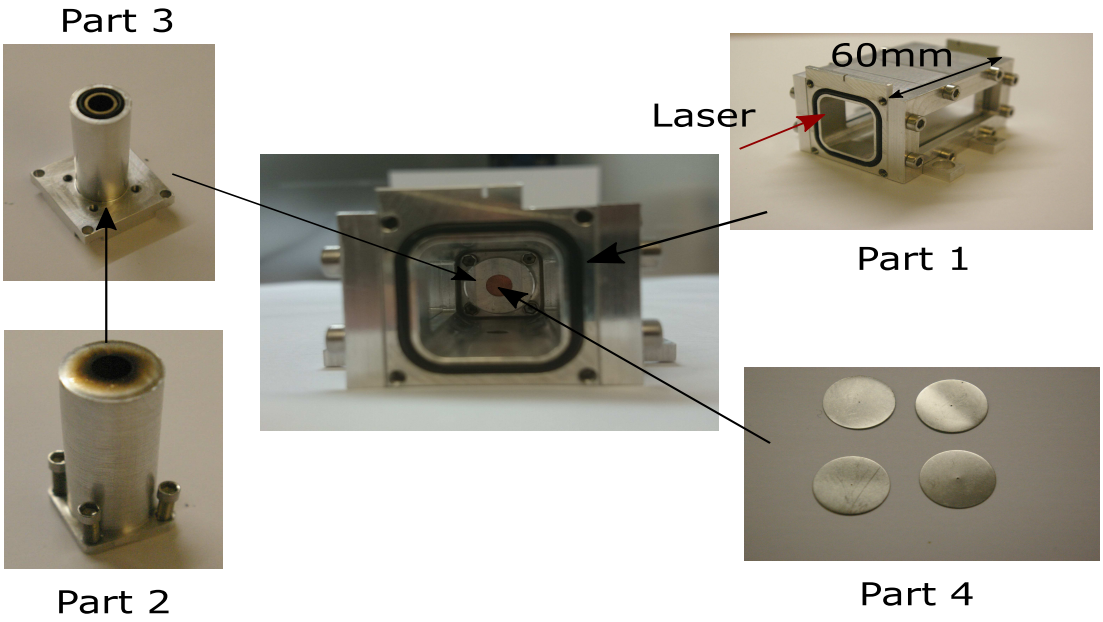


Figure 3.15: The parts making up the 2015 ASTRA gas cell. Part 1 forms the body of the target, with part 2 trapping part 4, the foil, onto part 3; this assembly is then attached to part 1 as is shown in the central picture.

reduced the foil thickness to 200 µm as the OpenFOAM simulation demonstrated that decreasing the thickness had little effect on the gas density profile.

The fixtures used to hold the parts together were standard M3, 5 mm length stainless steel bolts that located into tapped aluminium holes, the use of different materials for the housing and bolts prevents the bolts from seizing in the threads. In addition, the standard nature of these fixtures made them easy to source and interchange. Unfortunately, due to the size of the square face which had to keep a small profile, bolt heads of the bolts used to attach parts 2 & 3 together had to be turned down in order to fit in such a tight space.

3.4.3 Experimental Improvements

Part 1, in figure 3.15, was re-designed during an experimental break to remove the sapphire windows. This was done for two reasons: firstly the windows were not being used; secondly, their removal allowed for a much slimmer profile, making it easier to manoeuvre the gas cell. The four metal feet, were originally designed as separate pieces but computer aided manufacturing allowed for these also to be incorporated into the main body of the design. The final version of part 1 is shown in figure 3.16. All of these changes, also meant a reduction in the number of rubber seals that had to be formed, reducing the likelihood of a gas leak.

Initially, Part 1 of the gas cell was designed with metal lips to help locate the gas cell relative to the laser focus. However, it became apparent whilst at ASTRA that this would not work and so a separate holder for a circular 1 inch United

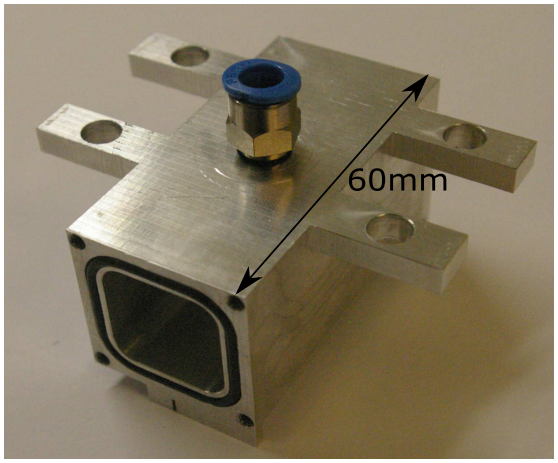
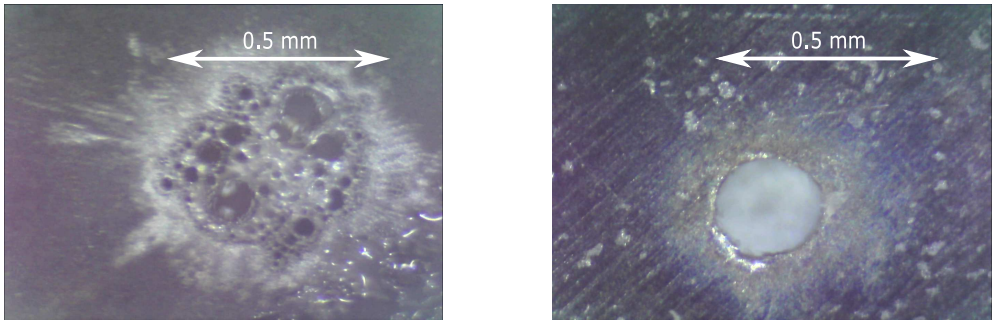


Figure 3.16: An image of the improved version of part 1 shown from the gas connection side, in which the sapphire windows have been removed and the legs attaching it to the hexapod form part of the main body.

States Air Force resolution grid was made to fit on the front of the main body, so that its exact location was know relative to the first foil that interacted with the laser, and allowing the laser focus to be placed at an exact known position inside the gas cell.



(a) (b)

Figure 3.17: Figure 3.17a shows the entrance hole created by the ASTRA laser system through the stainless steel foil. Figure 3.17b shows the same foil but with a pre-formed pinhole after exposure to the ASTRA laser for the same duration of shots in which the pinhole maintains its shape and size.

ASTRA is a comparatively 'high' repetition laser system capable of delivering short, high intensity pulses at 5 Hz. Initially, it was assumed that a hole would be perforated in the metal foil by the laser which would thus reduce the need to align the target. However, it was found, experimentally, that this in fact took a long period of time ($\sim$ 20 minutes), even at 5 Hz, and meant that the entry and exit holes were of different sizes. It was also found that a large jitter in the pointing of the ASTRA laser caused multiple holes to be drilled as can be seen in figure 3.17a. This eventually caused the overall size of the hole to become too large. To overcome this, pre-drilled pinholes with a diameter of 250 µm were

made in the foils. The pinholes then had to be aligned onto the laser axis, most easily achieved by using a CW diode laser with a cross-hair in the beam which, when viewed on a screen downstream of the gas cell, could be used very easily to determine when the two pinholes in the foil were aligned along the laser axis. Using pre-formed pinholes removed the difficulty associated with ASTRA forming the holes, as seen in figure 3.17b. It was found that these pinholes maintained a small size that was within the tolerance to allow for a smooth gas density profile.

Chapter 4

Measurements of Wakefields Driven by Multiple Laser Pulses

4.1 Motivation

This experiment was conducted between June and December 2015, over three access periods of six weeks, nine weeks and seven weeks. Between the second and third of these periods of access, the entire breadboard from the vacuum chamber was removed in order to allow another experiment to be conducted in the same chamber. The main experimental aim was to generate a plasma wakefield driven by a train of low-energy laser pulses separated by a plasma period. The purpose of this experiment was to provide a proof-of-principle demonstration of the MP-LWFA concept described in section 1.1.3.

To quantitatively measure the amplitude of the wakefield, Frequency Domain Holography (FDH) was used [61, 62]. The laser wakefield generated by the multi-

pulse technique was expected to have a relative wake amplitude of 1 - 10 %. It was found possible to measure wakes with amplitudes of about 1 % which, as far as the author is aware, is the lowest amplitude measured with this technique to date.

In this chapter, the experimental set-up employed is described in detail. A detailed account of the FDH analysis and an outline of how Temporarily Encoded Spectral Shifting (TESS) can be used to analyse the same data set is given. A full description of a TESS analysis of the same data set can be found in the thesis of group member James Cowley.

4.2 Experimental Set-Up

This section describes the beam line configurations. An initial introduction to the ASTRA laser system will be given, followed by a description of the optical layout of the drive beam and the method of generating a pulse train from the ASTRA laser system used to excite a wakefield. A description of the probe beam line and finally the alignment technique of the probe line to the drive beam will be discussed.

4.2.1 ASTRA Laser

The ASTRA-Gemini laser system is a short pulse (40 fs), high energy (12 J), dual beam laser which is used to explore many aspects of laser plasma interaction physics. Target area 2 (TA2), also known as the ASTRA Target Area, receives the full beam from the ASTRA laser system. The ASTRA laser, which acts as the seed for the ASTRA-Gemini laser, is a 5 Hz Ti:Sapphire system pro-

ducing 40 fs, joule-level pulses. A full description of the ASTRA laser is given below.

The ASTRA laser is based on the design of a chirped pulse amplification (CPA) laser system. In the first stage of a CPA system a pulse from an oscillator is stretched in time using a pulse stretcher to many times the original pulse duration. In the case of ASTRA 12 fs, 75 MHz laser pulses from a kerr-lens mode locked Ti:Sapphire laser are stretched in a glass block to 7 ps.

Pulses are stretched before amplification to avoid laser induced damage in the laser gain medium. For ASTRA there are several amplification stages. The first is a regenerative amplifier this increases the pulse energy from the oscillator to 0.8 mJ, this system only amplifies one pulse every millisecond. The rep-rate of ASTRA is then down selected, again, after the regenerative amplifier to 10 Hz by a fast pockels cell and polariser combination. The pulses pass through an acousto-optic programmable dispersive filter (AOPDF), this is a dispersive medium that shapes the pulses. The 10 Hz pulses are then further stretched to 530 ps by a pair of transmissive gratings. This additional stretch allows for hundreds of milli joules pulse energy levels to be reached. The pulses are then amplified in three multi pass amplifiers. Amplifier one takes the pulses from 0.8 mJ to 4 mJ in four passes of the Ti:sapphire crystal. Amplifier two takes this pulse energy up to 120 mJ and finally, amplifier three takes the pulse energy up to 1.2 J. Of the 10 Hz output of this system, half the pulses are sent to the ASTRA target area (TA2) while the other half act as a seed for the ASTRA-Gemini system for further amplification. This is achieved using a rotating half-wave plate and polariser. The 5

Hz pulses destined for the ASTRA target area then pass through a set of energy controls.

The final stage of the CPA system is to re-compress the stretched pulses, creating a short pulse high energy beam. For the ASTRA pulses this is achieved with a pair of gold gratings in a vacuum compressor that generates the final 45 fs 600 mJ pulse.

For increased stability, the ASTRA laser runs continuously in full power mode; however, energy control in the target area is achieved through the use of a polarising beam splitter and waveplate combination. For the experiments described here, this polarising beam splitter and waveplate combination were removed as they introduce a ~ 30 % energy loss on the main ASTRA beam. The parameters of the ASTRA laser are given in Table 4.1.

	Drive Beam	Probe Beam
Beam Diameter	55-60 mm	3.1 mm
Pulse Energy Post Compressor	600 mJ	0.3 mJ
Central Wavelength (λ_0)	818 nm	409 nm
Spot Radius (W)	$\sim$ 34 µm	$\sim$ 130 µm
Rayleigh Range (Z_R)	$\sim$ 4.6 mm	$\sim$ 130 mm
FWHM Pulse Length	45 fs	40 fs
Peak Power (P)	13 TW	-
Peak Intensity (I_0)	2×10^{22} Wm^{-2}	-
a_0	0.96	-

Table 4.1: Parameters of the ASTRA laser for the main ASTRA and probe beams.

Energy measurements of the main ASTRA beam were taken whilst the laser was operated at medium power just before the ASTRA compressor, and inside the vacuum chamber, before any of the target chamber optics. From these measurements the throughput of the compressor was found to be $\sim$ 60 %. This information was used to estimate the energy of the fully compressed beam on target to be 600 mJ, as the full power energy into the Target Area was measured as 1 J. The central wavelength was measured using a high-resolution spectrometer (Ocean Optics HR4000) and fibre optic cable (QP600-10-UV/VIS), placed in the path of the laser beam.

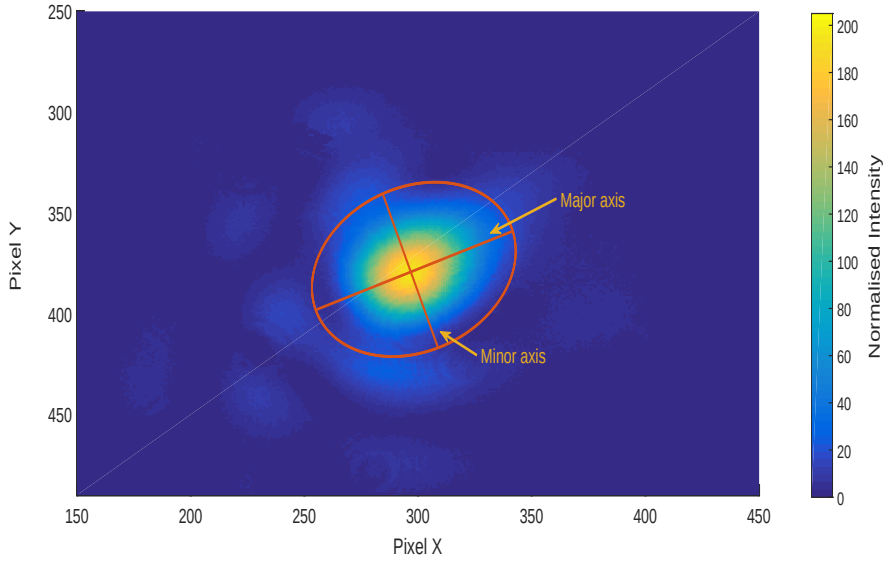
The spot radius was measured using a focal spot imaging system comprising of a charge-couple device (CCD) camera (Allied Vision Stingray) and 20 times microscope objective (20X Mitutoyo Plan Apo NIR Infinity Corrected Objective) mounted on an XYZ translation stage, located inside the vacuum chamber, allowing for the imaging of the focal spot created by the off-axis parabola. A small mirror, located just before the interaction point, could be flipped into the beam path in order to steer the beam on to the focal spot imaging system. Spatial calibration of this system was achieved by mounting a USAF resolution grid and back lighting it with the 800 nm wavelength drive beam; the USAF resolution grid was then brought into sharp focus on the CCD using the XYZ stage. The Rayleigh range was determined by measuring the focal spot waist $W(z)$, as a function of position, along the propagation axis. A curve was then fitted for the

focal spot waist against position of the form,

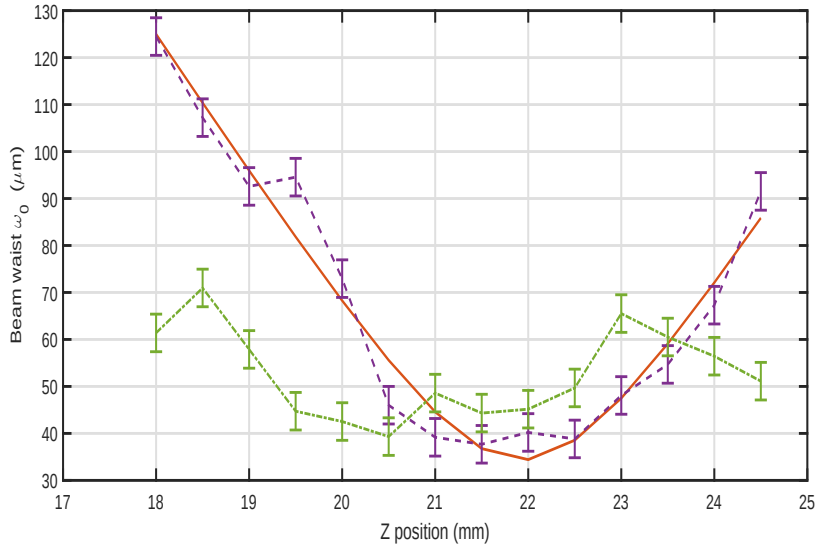
$$W(z) = \sqrt{1 + \left(\frac{M^2(z - z_0)}{Z_R}\right)} \tag{4.1}$$

where Z_R, M^2 and x_0 are the coefficients of the fit, this gave a value for Z_R. The Rayleigh range Z_R is defined as $Z_R = \frac{\pi W_0^2}{\lambda}$. A typical example of the drive beam focal spot and the analysis of the variation of the focal spot size, with longitudinal position, is shown in figure 4.1. This analysis was performed using a code written by group member Gavin Cheung. The pulse duration of the drive beam was measured using a spectral phase interferometer for direct electric-field reconstruction (SPIDER) [63], this was cross-checked against a single-shot autocorrelator (SSA). Using these measured parameters, the peak power, intensity and a_0 of the drive beam were calculated.

The probe beam in TA2 was formed by picking off around 10 % of the ASTRA beam in the second amplifier. The probe was sent on a long delay line and then fully compressed using a separate compressor from the main ASTRA beam line. The energy of the probe beam was measured to be 0.3 mJ, and was taken at 800 nm immediately before its frequency was doubled. The Rayleigh range of the 400 nm probe beam was estimated to be $\sim$ 130 mm, as the distance over which the focal spot imaging system could be used to scan was smaller than the Rayleigh range of the probe. The duration of the 400 nm probe pulse could not be measured directly as the diagnostics were designed for an 800 nm wavelength. Therefore, a measurement of the 800 nm probe was made using an SSA installed on the probe beam line, directly after the probe compressor. It was found that



(a)



(b)

Figure 4.1: The analysis of a typical focal spot of the ASTRA drive beam. Figure 4.1a shows the raw image of the focal spot, with the solid orange line being the contour line of the 4 sigma moment method fit. Figure 4.1b shows the variation of the major (dash dot green line) and minor (dash purple line) beam waist of the spot. The solid orange line is the fit to the minor axis used to calculate the Rayleigh range.

the 800 nm probe pulse was compressed to around 40 fs and it was assumed that the pulse duration of the 400 nm probe beam would be shorter than this by a factor of $1/\sqrt{2}$, making the probe pulse approximately 28 fs.

4.2.1.1 Methods for Measuring the Amplitude & Phase of a Pulse

There are many different techniques for measuring the amplitude and phase of a pulse but only two ubiquitous methods in laser physics will be reviewed here, these are:

FROG - **F**requency-**R**esolved **O**ptical **G**ating. This is a spatially resolved autocorrelation technique. This requires splitting a pulse into two paths, one with a variable delay, recombining them on a non-linear optical medium. The second harmonic generation created by the non-linear medium is collected by a lens and sent to a spectrometer. The spectrometer CCD displays the pulse duration in one direction and the wavelength of the pulse in the other. From this measurement a full reconstruction of the phase of the pulse can be made by using an iterative retrieval algorithm. Further information on this technique is given by E. Walmsley *et al.* [64]

SPIDER - **S**pectral **P**hase **I**nterferometry for **D**irect **E**lectric-**F**iled **R**econstruction. This is a spectral shearing interferometry technique. In this method two copies of the same pulse are made. One is stretched in time, the other pulse has another copy made which is delayed in time. The two arms are then recombined on a non-linear optic, the second harmonic generated light is collected with a lens and sent to a spectrometer. An interference pattern is observed on the spectrometer.

The modulation of the spectrum allows for the direct calculation of the phase of the pulse. A detailed explanation is given by R. Trebino [65]

4.2.2 Drive Beam Line

The drive beam line set-up at ASTRA is shown in figure 4.2. The drive beam is produced by pulse train optics, see section 4.2.3, using the main ASTRA beam. Once the drive beam entered the target chamber from the main ASTRA compressor, it was steered onto the same beam path as the probe, which was combined with the drive beam path through the back of a 'dichroic' mirror which was highly reflective for 800 nm radiation and had high transmission for 400 nm radiation. Both beams were then focussed using an f/18, f = 1 m off-axis paraboloid to the interaction point (IP) in the chamber. Located in the focal region was the gas cell which was mounted on a Hexapod stage (Physik Instrumente) to give complete control of alignment of the target to the drive beam axis. Post the IP, the drive beam was reduced in intensity by a 'dichroic' mirror (CVI BS1) which reflected 1 % of 800 nm light. Behind this 'dichroic' mirror was placed an energy meter (Molectron) that was used to monitor the shot-to-shot variation of the energy of the drive beam. Both drive and probe beam were then collimated by a 1 m focal length lens before exiting the vacuum chamber via a window. The beams were then reduced in diameter by a factor of 3 using a Galilean telescope. The drive beam was sent to two far-field cameras: the 'wide view' set-up comprising a 300 mm focal length lens and a CCD camera (Allied Vision Pike) and a 'focal spot' set-up comprising a 300 mm, a 10 times microscope objective (10X Mitutoyo Plan Apo NIR Infinity Corrected Objective) and a beam tube lens imaged on to

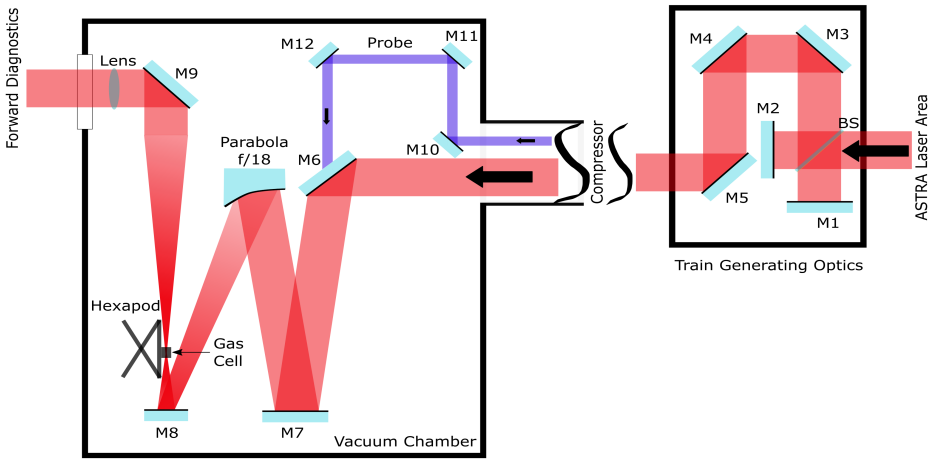


Figure 4.2: Experimental layout of ASTRA drive beam. Where M# represents a mirror, and BS a beam splitter. The red beam represents the 800 nm drive beam and the blue beam represents the 400 nm probe beam. The right shows the final configuration of the pulse train generating optics for the main beam. The probe was combined with the main beam through the back of M6. Both the probe and drive beam were then focused using an off-axis parabola. M9 was only partially reflecting for the drive beam and so was used as a beam dump.

a CCD (Allied Vision Pike). The 'wide view' system was used to locate the drive beam and determine drift, while the additional 'focal spot' system was used to monitor the beam quality during high powered shots.

In order to locate the IP accurately, two measurements had to be made. The first measurement was to image the focus, to do this a temporary camera and microscope objective were placed in the chamber to image the focus of the drive (and probe) beam down stream. For the second measurement, a thin wire was attached to a bolt hole on the hexapod stage and the hexapod was manoeuvred

until the wire was brought into focus. Since the distance between the front pinhole and the wire could be measured, this information allowed the distance between the front pinhole and the laser focus to be calculated. This enabled the entrance of the gas target to be placed correctly, relative to the focus.

4.2.3 Generation of Pulse Trains

Generating a multi-pulse wakefield requires a laser capable of generating a train of multiple 70 fs duration pulses, with a varying time delay between each pulse of around 50 - 200 fs and focused intensity of 1×10^{20} Wm^{-2}. Unfortunately no laser facility can offer such a laser system, at this time, and it was therefore necessary to adapt the ASTRA laser system to generate a train of pulses from a single pulse. Two methods for doing this were investigated, both of which worked by inserting additional optics into a single, chirped pulse from the ASTRA laser. The optical systems were: (i) a multi-order wave plate and a linear polariser; and (ii) a Michelson interferometer which was reported on by Shalloo [66]. Method (i) had the advantage that, in principle, all the incident energy could be converted into a pulse train; however, as described below, problems with the wave plate meant that this method had to be abandoned in favour of the Michelson method.

4.2.3.1 Multi-order Wave Plate

The single, ultrafast pulse from ASTRA enabled the generation of a pulse train to be achieved by spectrally filtering a chirped pulse. This was initially attempted using a multi-order waveplate and linear polariser, exploiting the polarisation of the beam to generate a pulse train as has been achieved by Robinson [67], albeit with lower pulse energies than provided by ASTRA. The ASTRA beam

was stretched, by adjusting the grating separation in the ASTRA compressor, to around 1-2 ps and passed through a 60 mm diameter, potassium dihydrogen phosphate (KDP) crystal, of thickness l, which had its e and o axes oriented at 45° to the input polarisation, thus the input pulse is decomposed along these axes. Due to the difference in the refractive index experienced by the o- and e-waves, the two polarisations develop a phase difference of $\phi = (2\pi/\lambda)\Delta n l$, changing the polarisation state of the beam. Since the laser pulse is spectrally chirped, and ϕ depends on the wavelength, the polarisation of the transmitted beam depends on λ, and hence on the temporal position within the pulse. If the pulse is now passed through a linear polariser oriented parallel to the incident beam, those wavelengths for which $\phi = 2\pi m$ will be transmitted with no loss.

By replacing the polariser with a polarising beam-splitter, two pulse trains could be separated from each other, with orthogonal dominant polarisation [66]. Either polarisation can be used to drive a wakefield. By using a Michelson arrangement, as shown in figure 4.3, the delay between the two pulse trains can be adjusted. By timing the relative delay between these two to a multiple of λ_p all of the incident laser energy can be used to drive a wakefield. The relative timing between the two pulse trains can also be set to dampen the wakefield generated by one pulse train with the other trailing pulse train and thus recover the energy from the system. However, this method did not work as the two surfaces on the KDP plates were not parallel to less than an arcsecond. This meant that pulse trains were generated in the near-field beams, but that when focussed the two polarisations were focussed to different points, so that pulse trains were not generated in the focal region.

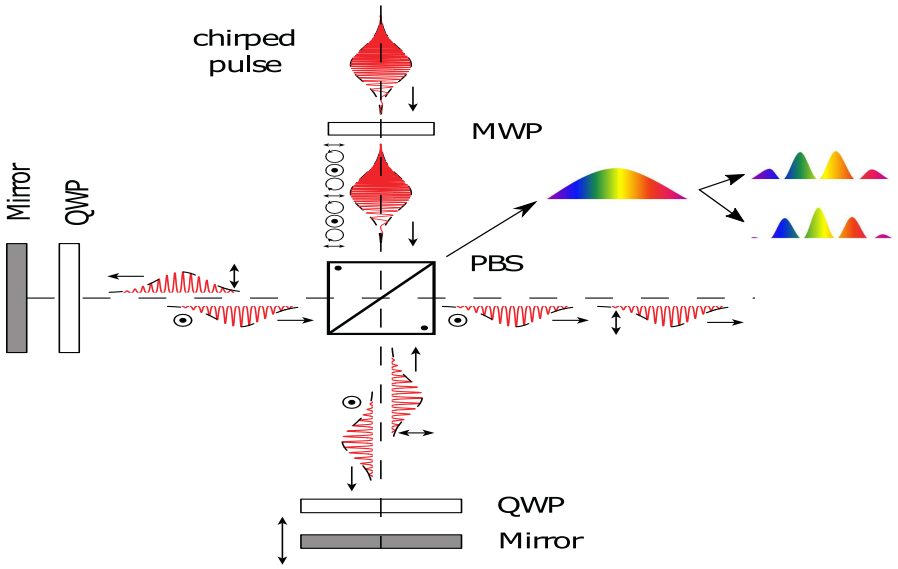


Figure 4.3: Layout of the optics used to generate a pulse train using a multi-order wave plate set-up. Where MWP is the multi-order wave plate, PBS is a polarising beam splitter and QWP is a quarter wave plate. The chirped pulse passes through the MWP, decomposing it into its different polarisations according to wavelength. The PBS then 'sliced' the stretch pulse, as is seen on the right hand side of the figure.

4.2.3.2 Michelson Interferometer

The other method investigated was to spectrally filter a stretched pulse from the ASTRA compressor using a Michelson interferometer to generate the pulse train. When a phase delay of $\phi = \frac{2\pi\Delta x}{\lambda}$, where Δx is the path difference between the two arms, is introduced, wavelengths for which the total phase difference is equal to an even integer multiple of π will be transmitted with zero loss. However, this technique has the disadvantage that half of the initial energy was being lost, by generating a pulse train that was reflected but could not be recovered.

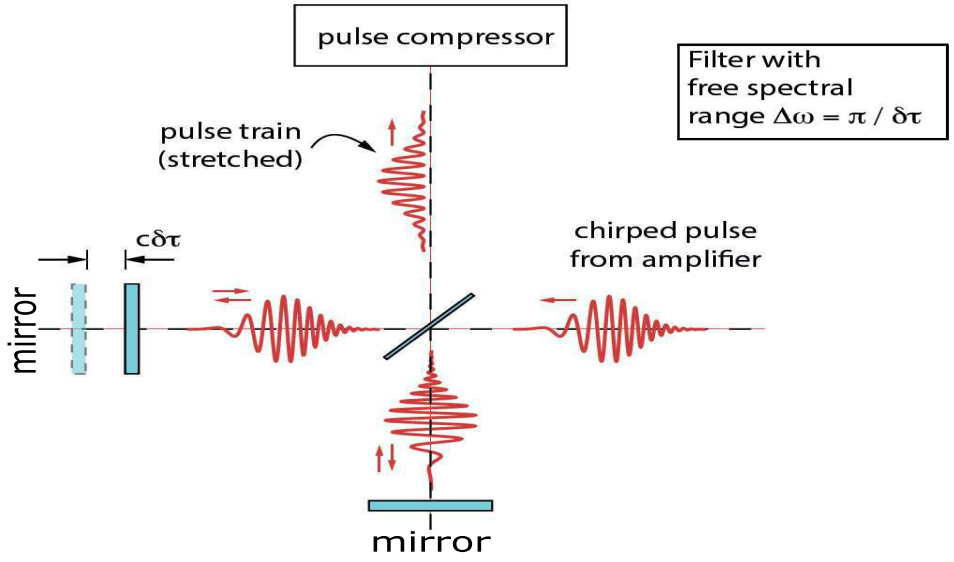


Figure 4.4: Layout of the optics used to generate a pulse train using a Michelson interferometer set-up. Where $c\delta\tau$ is the path difference Δx of the two pulses. The chirped pulse from the final amplifier in ASTRA is spectrally filtered using a Michelson interferometer before being compressed.

It was found that implementing this method after the ASTRA compressor caused the B-integral, a measure of the nonlinear phase shift of a pulse, experienced by the beams - especially the one which passed through the beam splitter three times - was significant. The B-integral for a single passage through the beam splitter was calculated to be approximately 3, this leads to self-phase-modulation of the pulse [68]. This self-phase-modulation causes the frequency to vary within the pulse and caused the pulse train to be washed out as each pulse now has a different frequency variation. This was overcome by moving the Michelson to before the ASTRA compressor, as shown in figure 4.4. The beam splitter (Manx), was 4 inches in diameter, 50:50 at 800 nm optimised for P-polarisation, made from

BK7 glass, measuring 12.95 mm thick. Both arms of the Michelson were retro reflecting by dielectric mirrors, with one arm on a motorised stage (Thorlabs DRV014), giving a minimum increment of 1 µm. By placing the Michelson before the ASTRA compressor, even at the full power of the ASTRA laser, the B-integral was $B \ll 1$ as the pulses were still stretched to many hundreds of picoseconds. The Michelson could be operated in two ways:

1. Two fully compressed (sub 50 fs) pulses separated by $\tau = x/c$, could be generated by setting the ASTRA compressor to give optimum compression, referred to as the double pulse regime. This allowed for experiments to be conducted where one pulse generated a wakefield and the second pulse was used to damp this wakefield as was originally possible with the multi-order wave plate method.

2. A pulse train could be formed by spectrally filtering a stretched pulse, as described above. When the two pulses were displaced from each other a given phase delay was introduced using the Michelson. This long pulse train was then compressed using the main ASTRA compressor by adjusting the grating separation. This allowed the production of pulse trains with pulse numbers greater than $N = 2$.

4.2.3.3 Different Operating Regimes

As already described, the Michelson configuration reduced the total on-target drive laser energy by 50 %. In order to make a valid comparison of the measured wakefield amplitudes generated by a single pulse, initial experiments used a configuration which turned the beam splitter in the Michelson by 90 degrees; the

	Single Pulse	Pulse Train(N≈7)	Double Pulse
Pulse Energy On Target	210 mJ	300 mJ	150 mJ
FWHM Pulse Length	55 fs	1 ps	65 fs
Peak Power (P)	4.7 TW	0.6 TW	2.3 TW
Peak Intensity (I_0)	2.6×10^{21} Wm^{-2}	0.3×10^{21} Wm^{-2}	1.3×10^{21} Wm^{-2}
a_0	0.35	0.12	0.24
Pulse Separation	-	112 fs	365 fs

Table 4.2: Parameters of the different pulses used to drive a wakefield.

transmitted beam was then blocked. This effectively bypassed one of the arms of the Michelson and reduced the energy of the pulse by 50 % making the energy on target comparable to that achieved with pulse trains. The parameters for the different regimes are shown in table 4.2, where the pulse length is the total duration of the pulse rather than the duration of individual pulses in a train.

4.2.3.4 Pulse Train Characterisation

The pulse trains and double pulse were measured using a home-built single-shot autocorrelator (SSA). A pick-off of the drive beam was taken, using a 1 inch silver mirror that could be driven into the path of the beam; the beam from the pick-off was then sent through a thin window to the SSA. The SSA split the beam using a thin film pellicle (Thorlabs BP245B2), and one beam was then sent to a fixed arm and the other to a variable arm, used to calibrate the SSA. Both beams were recombined on a 15 mm diameter, 150 µm thick SHG crystal (Inrad) cut at 38.8°. This very thin crystal gave a large spectral bandwidth, which gave the temporal resolution to measure the short pulses in the train. The frequency doubled light was collected and focussed onto a CCD camera (Marlin), using a 1 inch, biconvex, 50 mm focal length lens. An 800 nm filter was placed on the front of the CCD

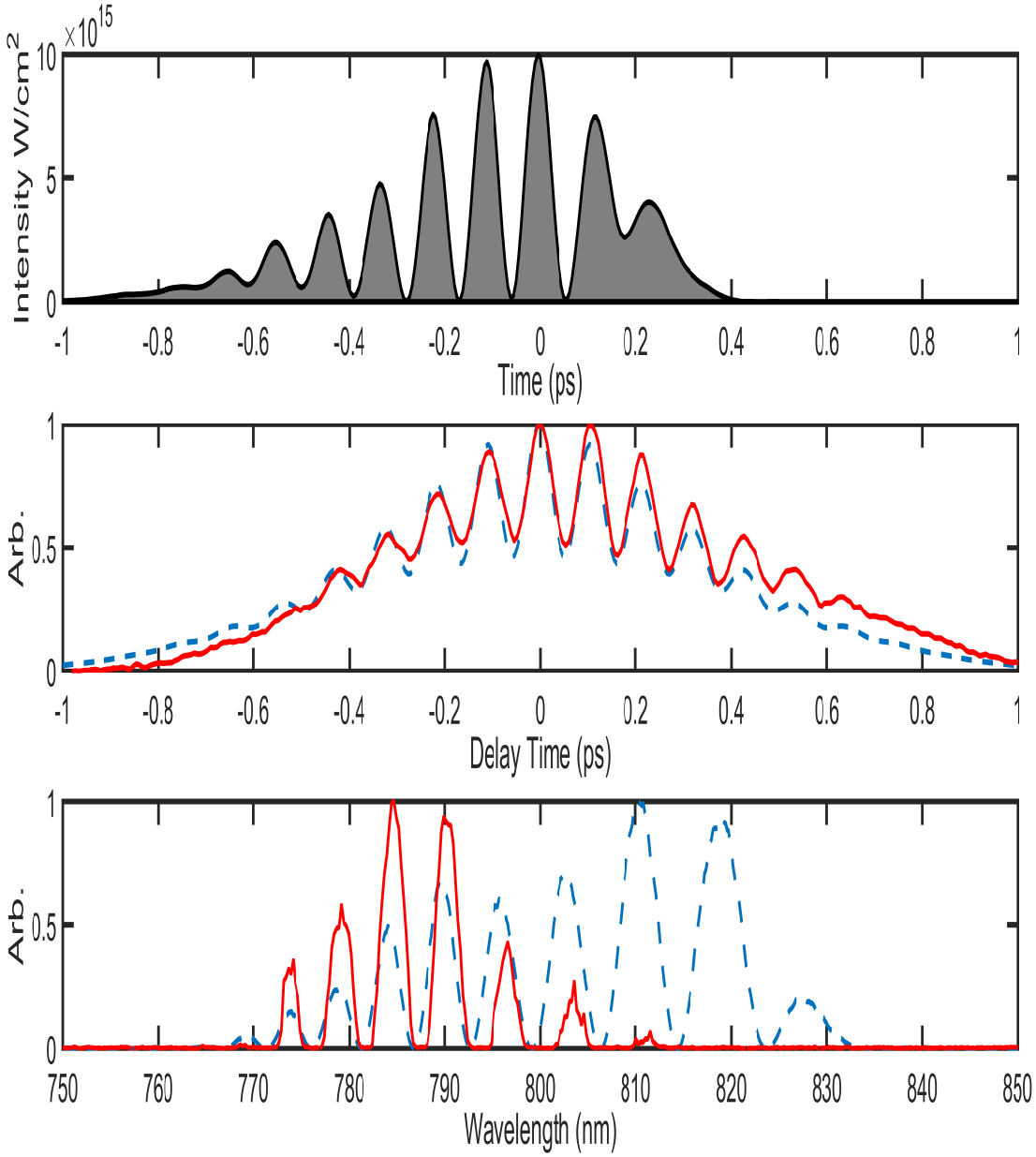


Image courtesy of Rob Shalloo

Figure 4.5: the reconstructed pulse train (Top), the recorded lineout of the SSA (Middle) and the recorded spectral fringe modulation taken by spectrometer just after the compressor (Bottom). The solid red line is the recorded data and the dashed blue line the fit of reconstructed measurement of the pulse train from a model of the Michelson and vacuum compressor.

camera to protect it from any stray laser light. To avoid damage to the camera, a piece of 3.6 ND filter was placed between the camera and the lens that captured the 400 nm light from the crystal, when the ASTRA laser was used at full power.

A lineout from the SSA along with the spectrum of the pulses, as shown in the middle and bottom of figure 4.5, were used to reconstruct the pulse trains. The pulse trains were reconstructed from these measured output as follows. The amplitude transmission of the Michelson and ASTRA compressor were calculated as a function of frequency. The measured spectral amplitude of the laser pulse leaving the final amplifier were multiplied by this transmission to give the spectral amplitude of the pulse train. The temporal profile of the pulse train, as shown at the top of figure 4.5, was then calculated by taking a Fourier transform, and from this an autocorrelation was calculated. The calculated autocorrelation was fitted to the measured autocorrelation, as shown in the middle of figure 4.5, allowing the parameters of the Michelson and compressor to vary within their experimental uncertainty. The spectrum of the modelled pulse train was compared to the recorded spectrum as is seen at the bottom of figure 4.5. The difference between the recorded spectrum and modelled spectrum in the bottom picture is caused by the fact that the 'dichroic' mirror (M9), described in section 4.2.2, does not have the same reflection efficiency across all wavelengths and so some of the spectral modulation are not seen.

4.2.4 Probe Beam Line

The probe beam set-up changed very little during the experimental run and was based on a Michelson interferometer, with the layout shown in figure 4.6. Unfortunately, the quality of the probe beam used was poor since it had a large number of visible striations in the near field. Therefore, a soft aperture, that is an aperture without a hard edge, was applied to the probe beam to avoid an Airy disk pattern. This was used to select a smaller portion of the probe beam measuring 3.1 mm in diameter. The probe was then frequency doubled using a 15 mm square Beta Barium Borate (BBO) type 1 crystal to maximise the efficiency of conversion. The BBO was measured to have a thickness of 600 µm ± 10 µm using a white light source microscope (OGP CMM zip250). The BBO crystal was held in a rotation mount (Thorlabs RSP1/M), on top of a rotation stage (Thorlabs PR01/M), to give maximum degrees of freedom. This enabled the production of a probe bandwidth of 5.6 nm full width half maximum.

The probe was then sent to a Michelson interferometer. The beam was split in the interferometer by a 6.48 mm thick, 1 inch diameter beam splitter (IDEX PW1-1025UV). Each arm of the Michelson was retro reflecting, which was achieved by using 1 inch diameter silver mirrors. The path length of one arm could be changed, as it was mounted to a manual translation stage, allowing the separation Δt of the probe and reference pulses to be adjusted.

Both the reference and probe pulses were then sent to a retro reflecting delay stage that was used to displace the probe pulses relative to the main pulse. This

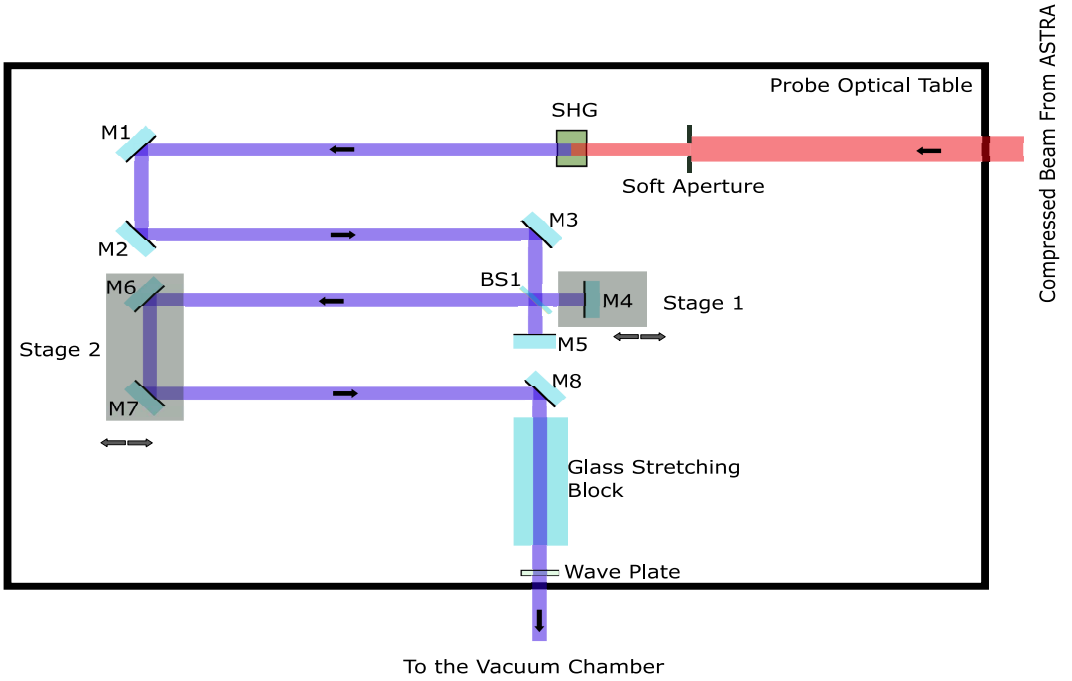


Figure 4.6: Experimental layout of ASTRA probe beam. Where M# is a mirror, BS is a beam splitter and SHG is a crystal generating second harmonic light. The red beam is the initial fundamental 800 nm light and the blue beam is the second harmonic generated 400 nm light.

stage used a stepper motor actuator (Thorlabs DRV014) with a 50 mm working range that had a precision of 2 µm and hence could position the probe and reference pulses relative to the main pulse with a precision of ±7 fs.

The probe and reference pulses were then sent through a 160 mm thick piece of BK7 glass to stretch them by dispersion to approximately 1.5 ps. Finally, both pulses passed through a half wave plate to change their polarisation from that of the main ASTRA drive beam. Before implementing this change, drive-generated blue light caused by low order high harmonic generation (HHG) was created by the interaction of the drive beam with the gas target. This HHG was found to

interfere with the probe and reference pulses, causing unwanted spectral fringes. With the polarisation of the probe and reference pulses orthogonal to that of the drive pulses, it was straightforward to block drive-generated blue radiation. The pulses then entered the vacuum chamber and joined up with the drive beam through the back of the 'dichroic' mirror.

The probe beam then followed the same path as the drive beam until the spectrometers, where it was split from the drive beam using a 'dichroic' beam splitter designed to transmit (reflect) 400 nm (800 nm) radiation. The probe beam then passed through a polarising beam cube to block any of the pump generated blue light. The probe was then focussed on to the slit of an imaging spectrometer (Acton SpectraPro 2750) containing a 2400 grooves / mm grating which dispersed the spectra of the diagnostic pulses onto a CCD detector (Andor Newton, DU940N-BU) with 2048 by 512 pixels of dimensions 13.5 µm × 13.5 µm. The calibration of the CCD in the spatial dimension was achieved by imaging an Air Force resolution grid with the grating adjusted to zero-order. This gave a value of 1.3 µm per pixel in the spatial dimension.

This methodology was in contrast to the original design by Matlis [61]. In the Matlis design a fully compressed 800 nm pulse was frequency doubled. The remaining 800 nm and frequency doubled 400 nm were then sent through a piece of glass, referred to as the, 'walk off glass', causing them to be separated in time as each wavelength experiences a different refractive index. Both beams then passed through a second frequency doubling crystal to convert the 800nm pulse into 400 nm. Both pulses were now stretched to around 1 ps by a second piece

of glass. This method has the distinct advantage of having both probe beams travelling along the same optical path. However, the separation between probe and reference was fixed which would be a disadvantage here, as the pulse trains of different lengths required a different separation.

4.2.5 Beam Alignment

A method was developed to ensure that the probe and drive beams were co-propagating. This was achieved by using the in-chamber focal camera to observe the main and probe beams and adjusting the position and pointing of the probe beam to ensure that it overlapped with the drive beam both in the near and far fields. This method was complemented by observing the focii of the drive and probe beams with the probe beam spectrometer set to zero-order. A thin glass plate, mounted to the hexapod, was then moved into the beams; in just a few laser shots, the drive beam drilled a small hole, which could be observed as a black hole in the image of the probe beam on the spectrometer. This procedure allowed the overlap between the drive and probe beams to be checked, and also enabled the probe beam to be steered onto the entrance slit of the spectrometer.

4.3 Analysis Method

4.3.1 Commonalities of the Analysis Methods

In this section, the initial analysis which is performed for both the Temporarily Encoded Spectral Shifting (TESS) and Frequency Domain Holography (FDH) data is described. The complete analysis of both methods is then described in

subsequent sections. The probe and reference are imaged on to a spectrometer, and due to the separation in the time domain between the pulses, a fringe pattern is produced (as seen in figure 4.7a) such that the periodicity is determined by the timing separation. This is shown by the following equation,

$$I = |U_{ref}|^2 + |U_{probe}|^2 + 2\Re|U_{ref} + U^*_{probe}e^{-i\omega\tau}| \tag{4.2}$$

where I is the recorded intensity on the CCD, U is the electric field of the probe/reference and τ the time off-set between the probe and reference. When the probe interacts with a plasma wave, the additional phase it acquires is encoded in the fringe pattern. The fringe pattern was taken in the spectral domain but the wakefield signature was most easily seen in the temporal domain, which was accessed by taking a Fast Fourier Transform (FFT) of the spectral data.

By taking a FT in the horizontal direction and adding padding to the image, to increase the sampling of the signal, a temporal image of the data was formed, as shown in figure 4.7b. The main DC term, here centred at 0 ps, and the main sideband caused by the separation in the probe and reference can be seen at 5 ps; this was expected as the delay between the probe and reference added by the probe Michelson interferometer was set to 5 ps. Other sidebands are seen further out than this but were assumed to be caused by reflections from optics in the probe line. Either side of the sideband at 6.3 ps and 3.7 ps are the sub-sidebands. These two small symmetric blobs, are a result of the wakefield and it was these features that were used in the TESS analysis to recover information about the wakefield generated.

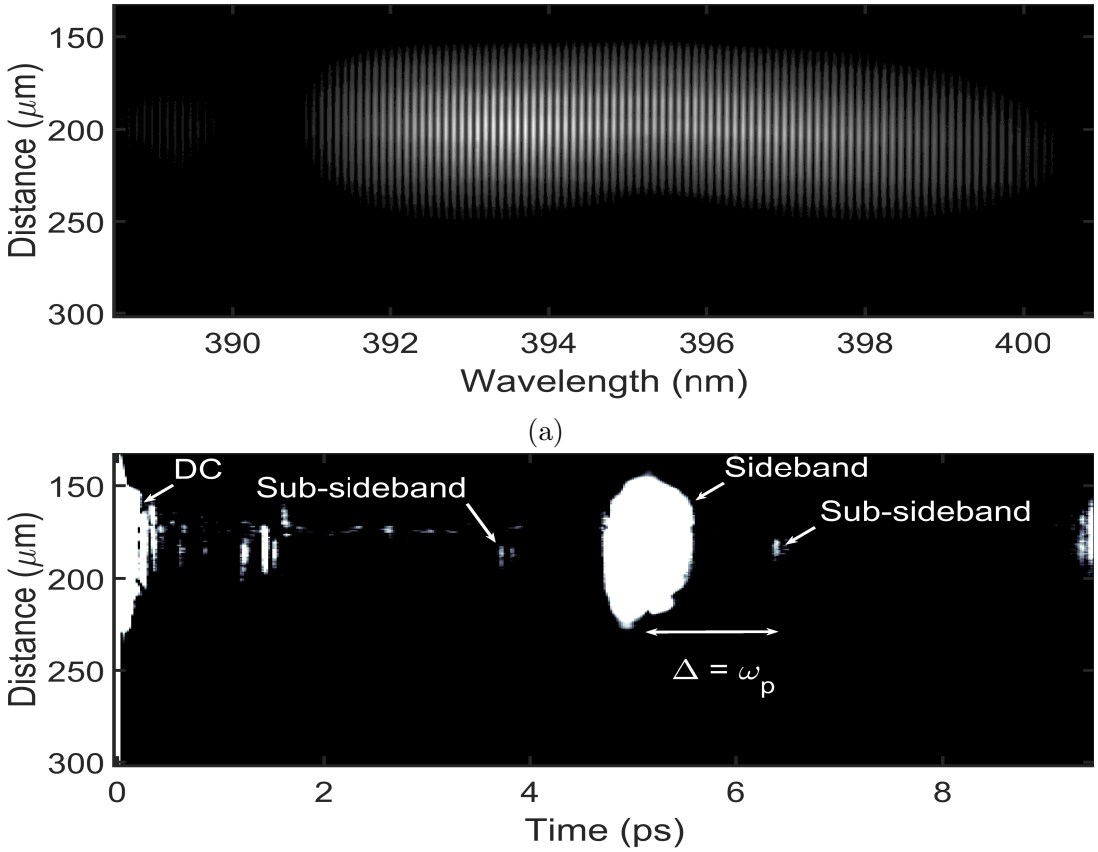


Figure 4.7: The key steps in the analysis of the data. 4.7a shows the raw spectral reference fringes and 4.7b shows the Fourier Transform of the fringes in time domain giving the TESS data.

At the beginning of each data run a set of reference spectrum was taken with no gas present, having undergone the same analysis as the data and being used in the subtraction of the background in both the FDH and TESS analysis. A more mathematical and detailed explanation of each analysis method will now be presented in the following sections. Figure 4.8 shows an overview of the steps undertaken for the FDH and TESS methods.

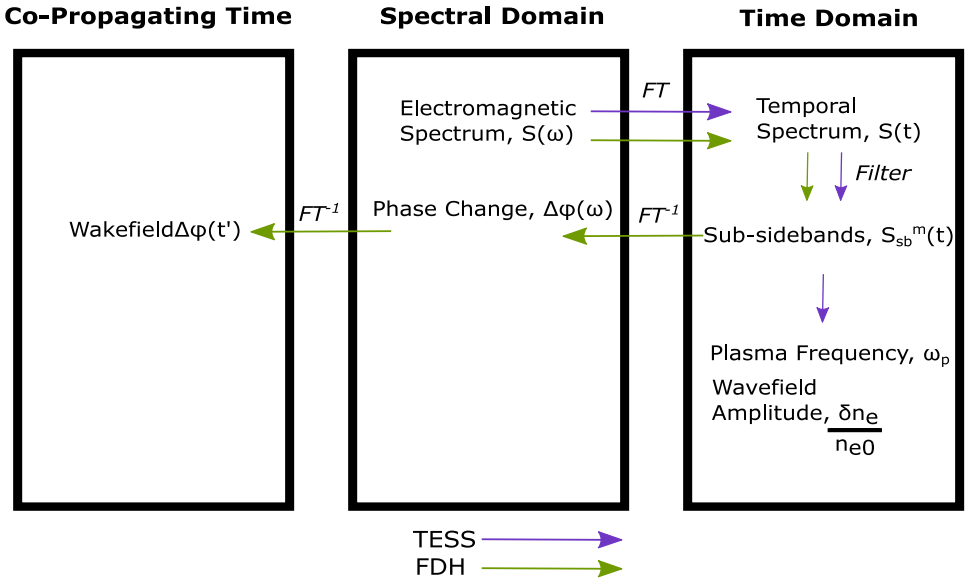


Figure 4.8: shows the key steps and results in the different transformations of the raw spectral data into the different domains.

4.3.2 Temporarily Encoded Spectral Shifting (TESS)

In TESS, the information about the wakefield is obtained from the time domain described in the previous section. Here, a mathematical description of the TESS method is given, starting with the consideration of the electric field of the probe and reference. The electrical fields of the two pulses in the frequency domain are given by,

$$E_{ref}(\omega) = \sqrt{S_{ref}(\omega)}\exp i\phi_{ch}(\omega) \tag{4.3}$$

$$E_{probe}(\omega) = \sqrt{S_{probe}(\omega)}\exp i[\phi_{ch}(\omega) + \omega\Delta t + \Delta\phi_{wakefield}] \tag{4.4}$$

where $S_{ref}(\omega)$ and $S_{probe}(\omega)$ represent the spectral intensities of the pulses, both pulses are chirped, represented by the spectral phase $\phi_{ch}(\omega)$, the phase difference between the two pulses caused by a separation in time Δt is $\omega\Delta t$, and finally the

additional phase caused by the wakefield is given by $\Delta\phi_{wakefield}$. It is assumed that the chirp of the probe and reference are the same, which should be a good approximation since the only difference between the two pulses is that the probe pulse passed through the Michelson beam splitter three times compared to once for the reference pulse. The additional path in material propagated by the probe pulse is four percent compared to that imposed by the glass stretcher block. When these two electric fields are recorded on a spectrometer, an interference pattern is seen resulting in a spectrum of the form,

$$I_s(\omega) = |E_{ref}(\omega) + E_{probe}(\omega)|^2 \tag{4.5}$$

$$= S_{ref} + S_{probe} + 2\sqrt{S_{ref}S_{probe}}\cos[\Delta t\omega + \Delta\phi_{wakefield}] \tag{4.6}$$

This gives the simple sum of the spectra and a fringe pattern. By taking the Fourier transform of equation 4.6, the phase shift of the fringe pattern can be determined,

$$\begin{aligned}\mathcal{F}[I_s(\omega)] = &\underbrace{\mathcal{F}[S_{ref}] + \mathcal{F}[S_{probe}]}_{\text{DC term}} + \\ &\underbrace{\mathcal{F}[\sqrt{S_{ref}S_{probe}}e^{i\Delta\phi_{plasma}(\omega)}](t-\Delta t)}_{\text{sideband}} + \\ &\underbrace{\mathcal{F}[\sqrt{S_{ref}S_{probe}}e^{-i\Delta\phi_{plasma}(\omega)}](t+\Delta t)}_{\text{sideband}}\end{aligned} \tag{4.7}$$

The Fourier transform, denoted by $\mathcal{F}$, then breaks the pattern down into a DC term and two sidebands, centred at $t = \pm\Delta t$. Either side of this sideband is the sub-sideband represented by $\Delta\phi_{wake}$, and defined as,

$$\Delta\phi_{wake} = \underbrace{\frac{\omega_{p0}^2}{2\omega_{probe}}\frac{l}{c}\frac{\delta n_e}{n_{e0}}}_{\Delta\phi_p} sin(k_{p0}\zeta + \theta) \tag{4.8}$$

where $\frac{\delta n_e}{n_{e0}}$ is the relative wakefield amplitude, l is the interaction length with the plasma and $\zeta = l - ct'$ which physically represents distance in the coordinates of the probe. For the TESS analysis, it is assumed that the wakefield is sinusoidal, a reasonable assumption since a very low amplitude wakefield is being driven. The sub-sideband distance, $\Delta\tau$, from the sideband can be measured to determine the plasma frequency of the wakefield, determined by,

$$\omega_p = \frac{\Delta\tau}{\phi_{GDD}} \tag{4.9}$$

where ϕ_{GDD} is the spectral second-order phase which has to be determined experimentally, as is shown in section 4.4.1. The relative height of the sub-sideband provides information about the phase shift caused by the wakefield and so can be used to determine the wakefield amplitude, the equation of the phases is given by,

$$\Delta\phi_p = J_1^{-1}\left[\frac{h}{F(\omega_{p0})}\right] \tag{4.10}$$

where h is the relative peak height, F is the form factor [62] and J_1^{-1} the inverse of the first Bessel function.

4.3.3 Frequency Domain Holography (FDH)

In FDH, further analysis on the data has to be undertaken in order to retrieve a phase map of the wakefield. This is achieved by firstly isolating the sideband and sub-sideband, by placing a band pass filter on the data. In this work the filter used was in the time domain and was formed of a square central region centred around the sideband, with a half Gaussian edge either side to avoid sharp discontinuities, that might add a ringing modulation to the data; an example of the masked sideband can be seen in figure 4.9. The sideband and sub-sideband are then shifted to zero frequency before an inverse FT is performed; this isolates one of the functions at Δt from equation 4.7 to give,

$$I_s(\omega) = \sqrt{S_{ref} S_{probe}} \exp\left[i\Delta\phi_{plasma}(\omega)\right] \tag{4.11}$$

Dividing by a reference spectrum removes all the terms due to the probe and reference pulses and leaves the phase difference caused by wakefield $\Delta\phi_{plasma}(\omega)$.

However, this is in the spectral domain and not in the co-propagating time domain of the wakefield. Unfortunately, when subtracting the reference spectrum from the data, the second-order spectral phase $\phi_{GDD}(\omega)$ is removed. The spectral phase $\phi_{GDD}(\omega)$ was artificially added back to the data so that the correct mapping between the spectral and time domain could be achieved. The spectral phase $\phi_{GDD}(\omega)$ was calculated using the measured value of group delay dispersion (GDD) taken in the experiment, as detailed in section 4.4.1. Having added the

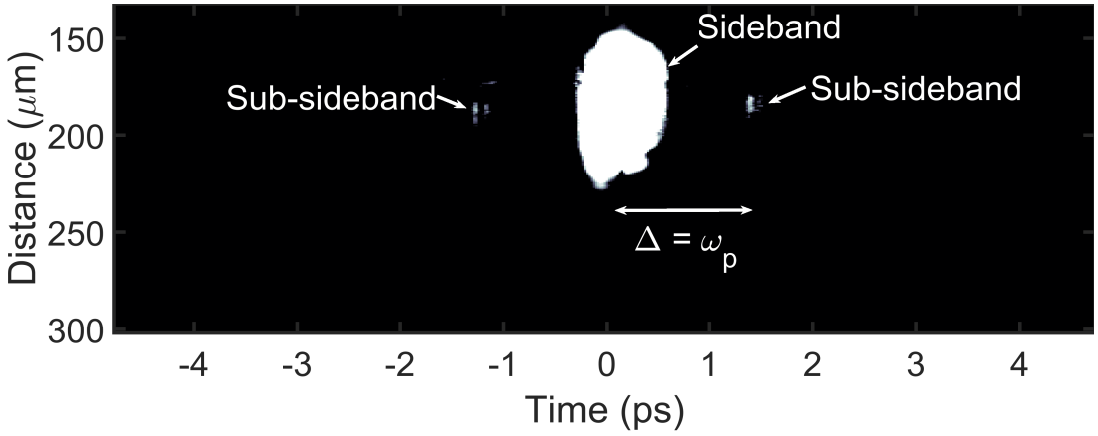


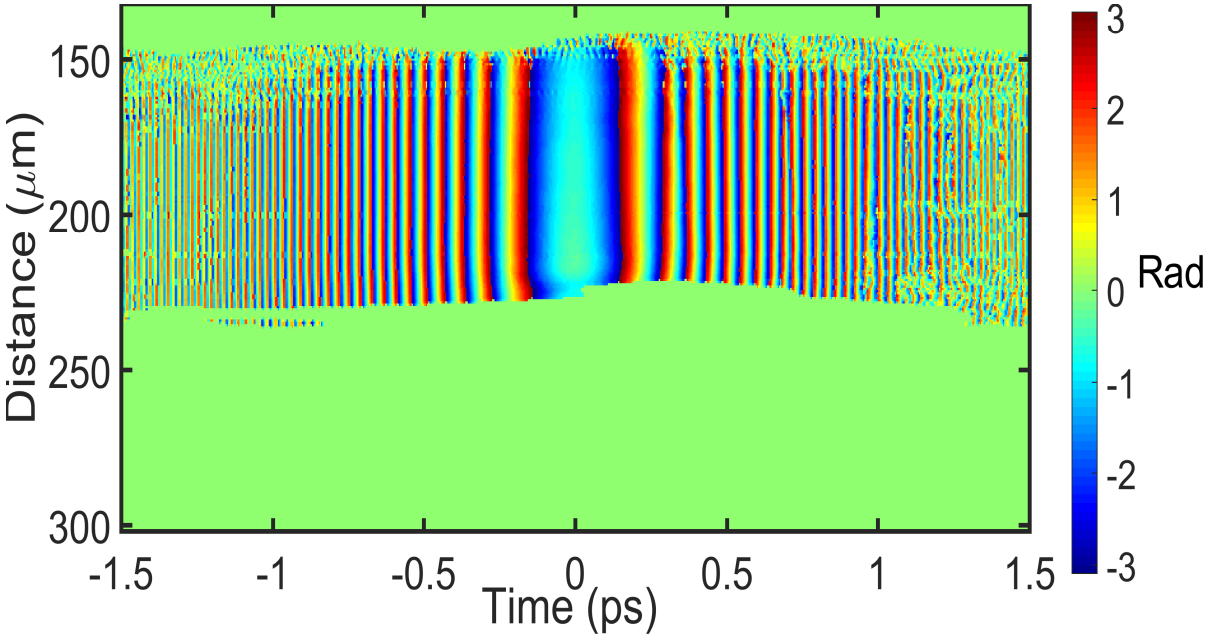
Figure 4.9: shows the isolated sideband and sub-sideband. This was achieved by isolating around the sideband with a mask. All other data outside of the mask is then set to zero. The sideband, along with the sub-sideband, is then shifted to the center of the image and is then located at 0 ps.

second-order spectral phases, an Inverse Fourier Transform (IFT) is taken,

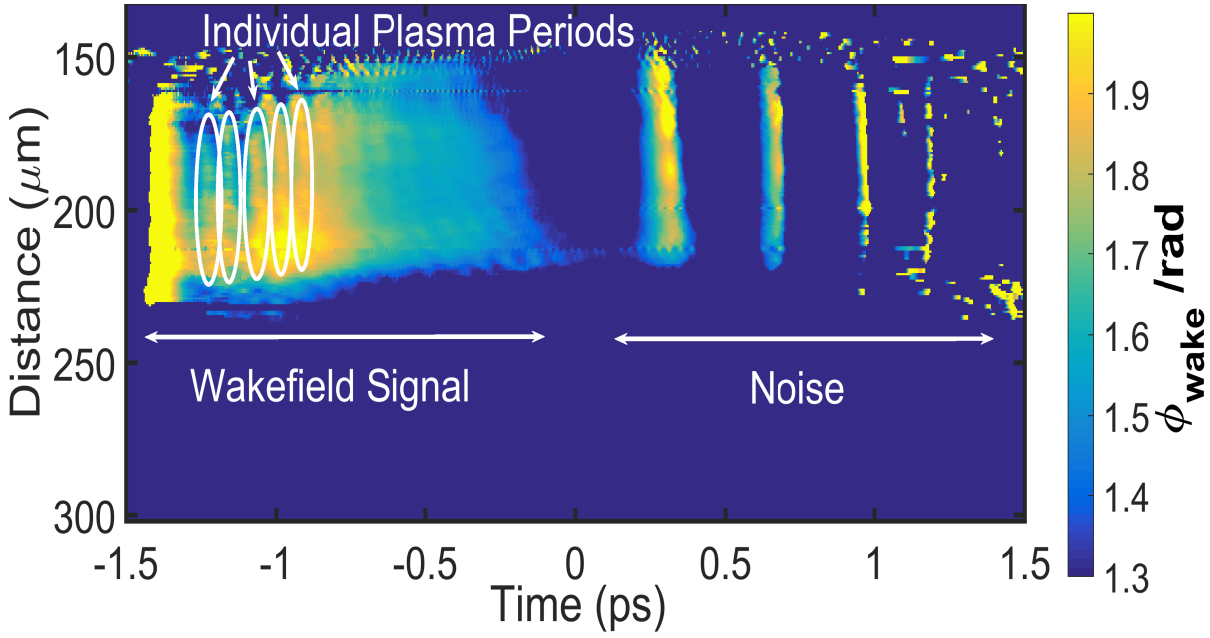
$$I_s(t) = \mathcal{F}^{-1}\{\sqrt{S_{probe}}\exp i\left[\Delta\phi_{plasma}(\omega) + \phi_{GDD}(\omega)\right]\} \tag{4.12}$$

$$= A\exp\{i[\Delta\phi_{plasma}(t) + \phi_{GDD}(t)]\} \tag{4.13}$$

An image of the temporal space in the frame of the wakefield is seen in figure 4.10a. As can be seen from the figure a fast varying value between $-\pi$ and π is present in the image. This is the second-order temporal phase term (which comes from the second-order spectral phase added before the image was IFT) which dominates the wakefield signal, and was expected to be small. The second-order temporal phase term had to be removed. This was most simply achieved by fitting a quadratic curve to the data, and using this value to determine the $\phi_{GDD}(t)$ and then subtracting it from the data.



(a)



(b)

Figure 4.10: 4.10a shows the IFT of the probe spectrum having undergone a background subtracted and the addition of $\phi_{GDD}(\omega)$. 4.10b shows the recovered FDH phase map. The features at 0 ps to 1.5 ps is noise, the feature from -1.5 ps up to 0 ps is the region where the wakefield signal is present. Within the wakefield feature you can see the oscillations in the phase which maps to the plasma frequency.

Finally, the extra padding that was added to the initial image was removed. This gives a phase map in the frame of the wakefield and is the analysis referred to as FDH. An example of the phase map is shown in figure 4.10b. By directly measuring the oscillations in the phase, a value for the plasma frequency of the wakefield can be calculated and cross-checked against the TESS method.

4.4 Results from ASTRA Experiment

4.4.1 Measurement of Probe and Reference GDD

In order to determine the second-order spectral phase (GDD) of the probe pulse, used in the TESS and FDH analysis to find the plasma frequency, a separate measurement had to be made. This was achieved by co-propagating the probe (reference) pulse with a short drive pulse. The drive pulse rapidly ionised the hydrogen gas, causing the spectrum of the probe (reference) pulse to be modulated. The local frequency of the probe (reference) pulse could then be measured by adjusting the delay between the probe (reference) pulse and the drive pulse, and tracking the frequency at which the spectral modulation was centred. Figure 4.11 shows an example of the probe spectrum recorded in the presence of the short-pulse drive. It can be seen that the spectrum is strongly modulated to give a set of non-uniform fringes, with a spacing which decreases either side of a wide dark fringe. As the delay between the probe (reference) and drive pulse was changed, the wavelength at which the central dark fringe was observed moved; this feature was taken to be the instantaneous wavelength of the probe (refer-

ence) pulse at the position of the drive beam. Hence changing the delay between the probe (reference) and drive pulse allowed the wavelength $\lambda(t)$ of the probe (reference) pulse to be measured as a function of time t. Using this information, equation 4.15 shows how to relate these values to spectral GDD, when there is a large chirp on the pulse.

$$\psi^2(\omega) = -\frac{1}{\phi^2(t)} \tag{4.14}$$

$$\psi^2(\omega) = \frac{1}{\frac{d\omega}{dt}} \tag{4.15}$$

Code was written by the author to analyse the data set from the ASTRA experiment to determine a value of $\psi^2(\omega)$ (GDD) of the probe (reference) pulse. The first step was to load the image from the spectrometer into MATLAB and convert the pixel numbers on the x-axis into wavelengths,

$$\lambda(nm) = 0.006N + 385.8 \tag{4.16}$$

where λ is the wavelength and N the pixel number. This formula is derived from a calibration using a mercury argon lamp in which specific wavelengths were already known. The modulated spectrum was averaged over 200 rows located vertically about the centre of the spectrum. On a plot of the averaged spectrum, the user would select the position of the central dark fringe; the code would then search in the horizontal direction over ± 100 pixels to find the lowest normalised pixel intensity and therefore the minimum value in that region. An example of such a modulated feature and its corresponding lineout can be seen in figure 4.11.

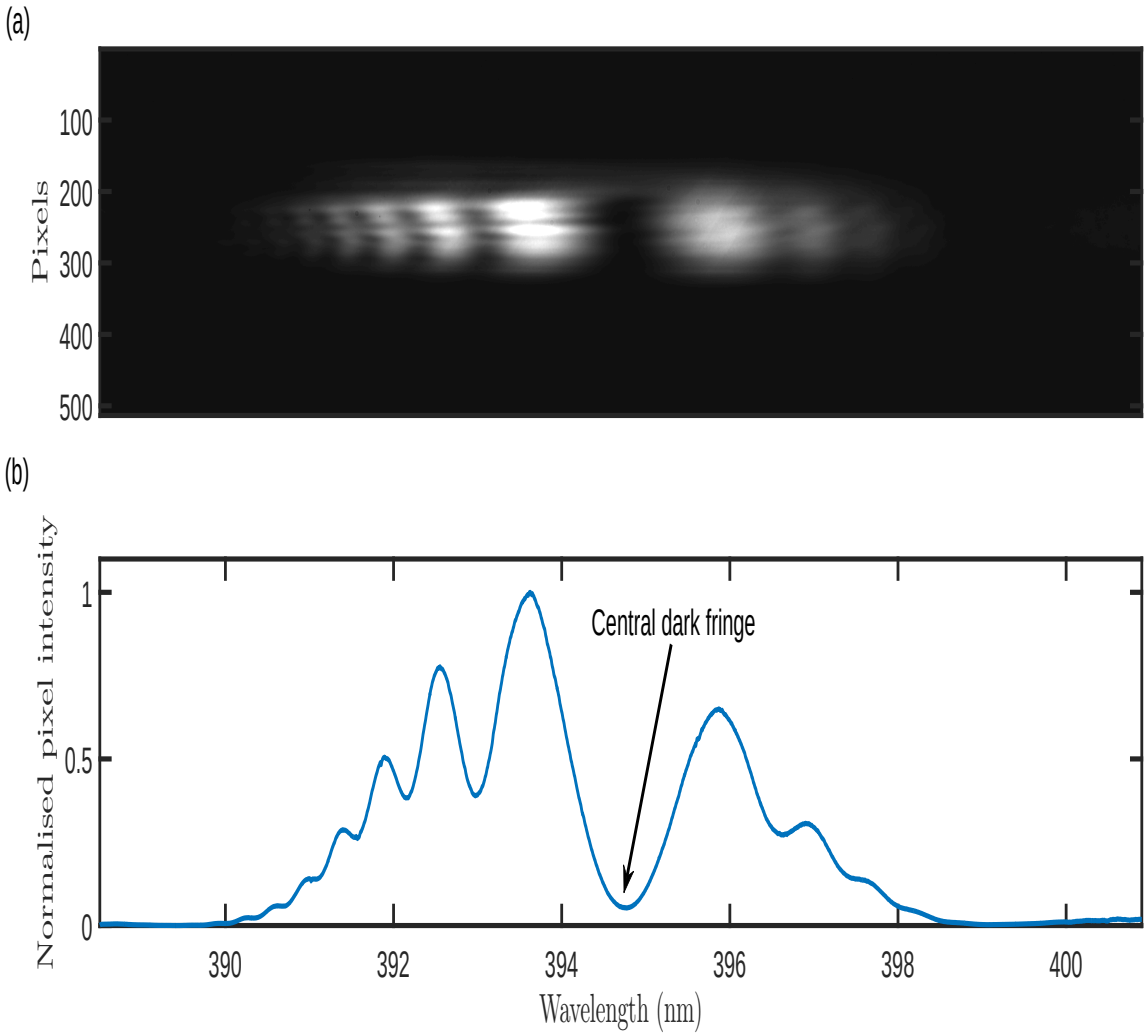


Figure 4.11: Determination of the probe GDD. (a) Raw spectrum of the probe pulse in the presence of a short drive pulse. This causes a spectral modulation in the recorded probe pulse on the spectrometer. (b) A lineout of the modulated probe pulse spectrum. The line out is taken by averaging in the vertical direction of the modulated spectrum by a 100 pixels. The central dark fringe is the feature that is tracked across multiple spectrum to relate drive beam/probe interaction with respect to a wavelength.

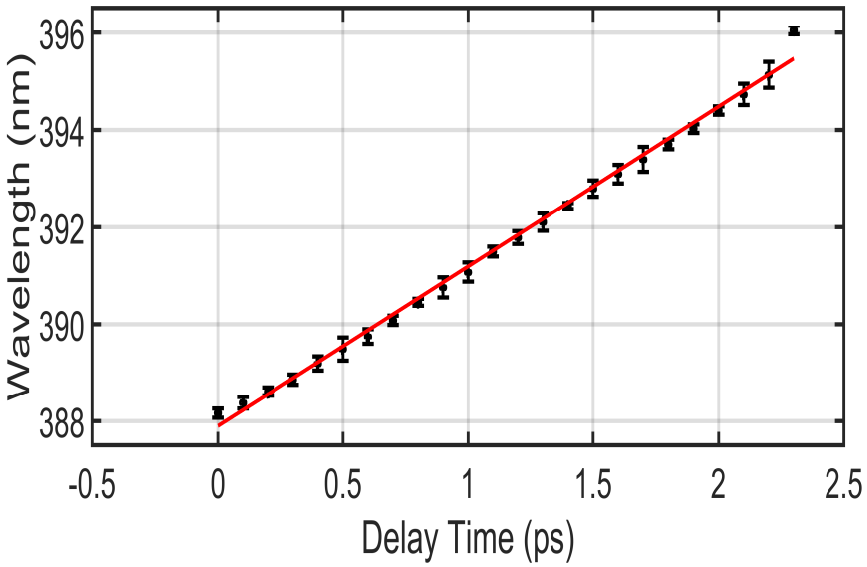


Figure 4.12: A linear fitted solid red line applied to the multiple data points taken by tracking the wavelength against drive pulse and probe separation this gives the value of $\frac{d\omega}{dt}$.

The wavelength point selected was then mapped against the time separation of the probe/reference and drive pulse. The values of the wavelengths were converted to angular frequency and a linear fitted curve was applied to the data, to reduce any irregularities. An example of this can be seen in figure 4.12. From this fitted curve the gradient was found and hence the GDD.

Two different values of the GDD were used in the analysis, as the value of the GDD is dependant upon the alignment through the glass block and this changes over time. For the single pulse analysis, the reference GDD was found to be (22 600 $\pm$ 600) fs^2 and for the probe to be (20 900 $\pm$ 300) fs^2, the difference in the value of GDD is (1700 $\pm$ 700) fs^2. For the pulse train and double pulse

data, the GDD for the reference was found to be (23 900 $fs^2 \pm 100$) fs^2 and for the probe to be (25 300 $fs^2 \pm 100$) fs^2, the difference in the value of GDD is (1400 $\pm$ 200) fs^2. The measured difference in the probe and reference GDD was caused by the fact that the probe/reference pulses travelled through different thickness of beam splitter, causing them to pick up a slight difference in GDD. For the thickness of beam splitter at a 45° angle, a difference in the GDD of the two beams is calculated to be 1400 fs^2, which is within the margin error of the measured difference of GDD for the probe and reference for all cases. However, the error on the measurements are large enough that this measurement technique is clearly not sensitive enough to accurately account for the difference in the GDD caused by the beam splitter and so fails to determine at exactly what angle the beam splitter was orientated.

4.4.2 Results of TESS Analysis

The TESS analysis of the data was performed by group member Christopher Arran. However, for completeness - and to enable a comparison with the FDH analysis - these results are also reported here. The first part of the ASTRA experiment used one arm of the drive Michelson but with a fully compressed 55 fs pulse to generate a linear wakefield. This was undertaken for two reasons. Firstly it provided a benchmark for the wakefields that could be generated with half the energy of the ASTRA system on target, making it comparable to the energy in the pulse trains. Secondly, it was assumed that generating a wakefield in any other way would be less efficient and so likely to generate a wakefield that was harder to detect using the TESS/FDH method. It was thus important that

the single pulse wakefield could be measured before trying more difficult wakefield generating techniques.

Figure 4.13a shows the plasma period measured from the sub-sideband separation against plasma period expected for the fill pressure. The expected plasma period is calculated from the ideal plasma frequency determined by equation,

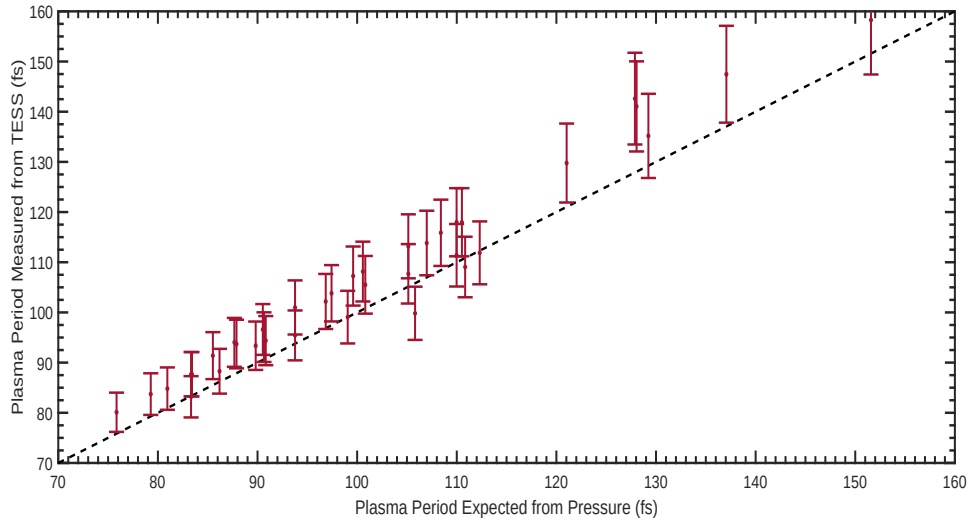
$$\omega_p = \sqrt{\frac{200P[mbar]}{k_B T}\frac{e^2}{m_e \varepsilon_0}} \tag{4.17}$$

The trend of the data follows the theory very closely and is a convincing result that a wakefield is being measured as the wakefield signature moves with pressure exactly as predicted. Figure 4.13b shows the relative wakefield amplitude deduced from a TESS analysis as a function of the hydrogen gas fill pressure by the single pulse set-up. The theory fit is given as,

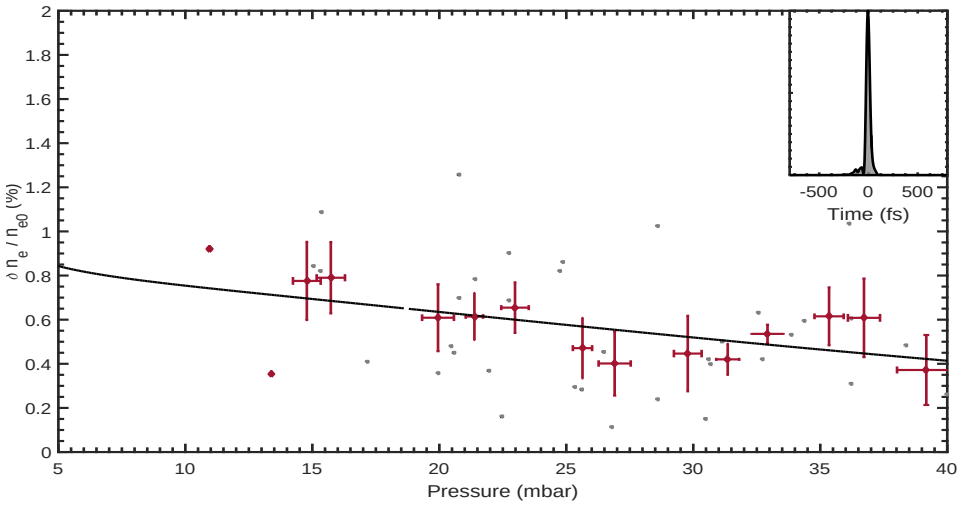
$$\frac{\delta n}{n_{e0}} = A(\omega_{p0}\tau_0)exp\left[-\frac{(\omega_{p0}\tau_0)^2}{16ln2}\right]\left[1+\left(\frac{2\sqrt{2}c}{\omega_{p0}W_0}\right)^2\right] \tag{4.18}$$

where τ_0 is the FWHM pulse duration and A the wakefield amplitude were used as free parameters to fit to the data. W_0 is the diameter of the focal spot which was set to 30 µm. This was adapted from Chen [69] and exhibits a weak resonance when $\omega_{p0}\tau_0 = 2\sqrt{2ln2}$.

After measuring the generation of a wakefield using a single pulse, the next step was to measure the generation of a wakefield using a pulse train. The pulse train that was decided upon was seven pulses, ignoring the pulses in the wings. The pulse wings are defined as below the point where the normalised intensity



(a)



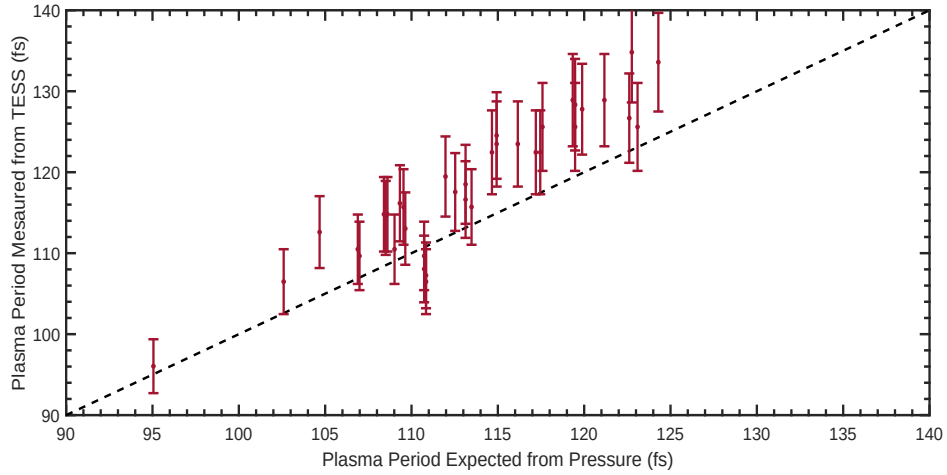
(b)

Images courtesy of Chris Arran

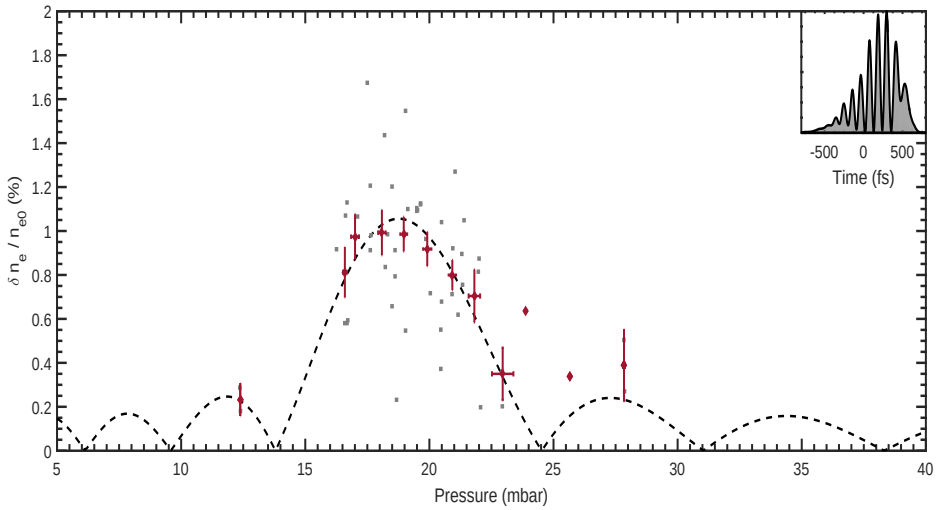
Figure 4.13: Determination of the wakefield generated by the single pulse set-up seen in table 4.2. Figure 4.13a measured the plasma period from the peak separation as a function of the expected plasma period for the cell pressure. The red circles are the data and the dashed black line is the theoretical ideal. Figure 4.13b measured relative wake amplitude as a function of cell pressure. The red diamonds are the binned data, taken over pressure bins of 4 mbar, and the error bars are standard errors. The gray dots are the raw data, while the black dashed line represents the predicted wakefield amplitudes for this driving pulse as given by equation 4.18. The inset in the top right hand corner is a reconstruction of the temporal intensity profile of the driving pulse, as determined by the SSA measurement and the compressor settings.

had dropped below $1/e$. The pulse train was optimised by changing the ASTRA compressor grating separation to give a pulse train duration of $\sim$ 1 ps. Then the drive Michelson arm separation was adjusted, while observing the output of the SSA. The spectrum of the drive pulse was monitored on shot using a spectrometer; each pulse in the train gives rise to a spectral peak, and this diagnostic could be used to monitor the number of pulses in the train. This spectrum can be cross-checked against the SSA measurement. The depth of modulation of the SSA output was maximised by adjusting an AOPDF (FASTLITE Dazzler) at the start of the laser chain, to change the third and fourth order of the drive pulse, achieving a fine tuning optimisation. Once the pulse train had been optimised and characterised, the plasma wakefield was measured as a function of the cell pressure. This was achieved by taking three shots at discrete pressures separated by 1 mbar and allowing a couple of minutes for the hydrogen gas flow to stabilise at each new pressure.

Figure 4.14b shows the plasma period retrieved from measuring the sub-sideband distance in the TESS analysis against the expected plasma period for the fill pressure of the gas target. These data points fit well against the theory trend, showing that the correct feature in the TESS analysis is being identified. Figure 4.14b shows the measured relative wake amplitude as a function of cell pressure. It can be seen that the wake amplitude shows a strong resonance at around 19



(a)



(b)

Images courtesy of Chris Arran

Figure 4.14: Determination of the wakefield generated by the pulse train set-up seen in table 4.2. Figure 4.14a shows the measured the plasma period from the peak separation as a function of the expected plasma period for the cell pressure. The red circles are the data and the dashed black line is the theoretical ideal. Figure 4.14b shows the measured relative wake amplitude as a function of cell pressure. The red diamonds are the binned data, taken over pressure bins of 2 mbar, and the error bars are standard errors. The gray dots are the raw data, while the black dashed line represents the predicted wakefield amplitudes for this driving pulse as given by equation 4.18. The inset in the top right hand corner is a reconstruction of the temporal intensity profile of the driving pulse, as determined by the SSA measurement and the compressor settings.

mbar, corresponding to a plasma period of 115 fs. A theoretical fit of the form is,

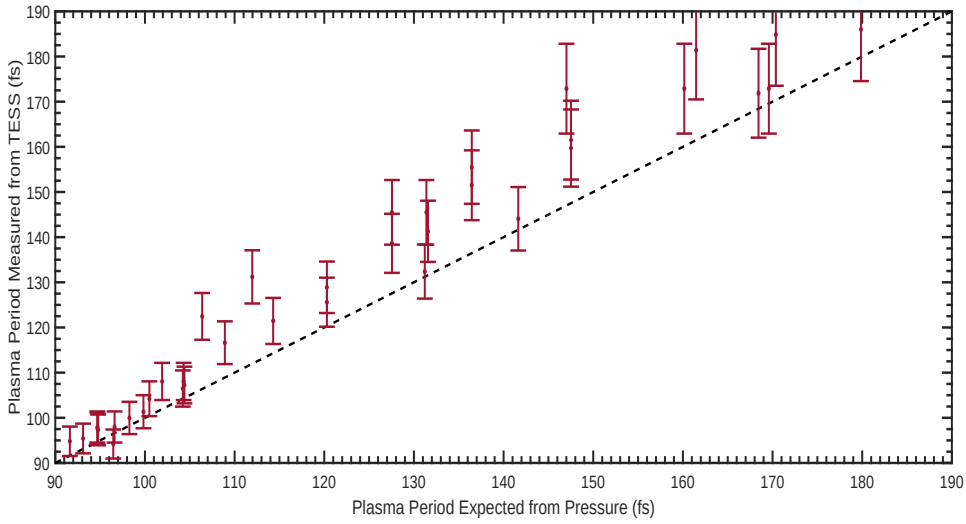
$$\frac{\delta n}{n_{e0\,N}} = \left[\frac{sin(\frac{1}{2}N\omega_{p0}\delta\tau)}{sin(\frac{1}{2}\omega_{p0}\delta\tau)}\right]\left[\frac{\delta n}{n_{e0}}\right]_{SinglePulse} \tag{4.19}$$

where N is the number of pulses, in this case seven, and $\delta\tau$ is the pulse spacing which shows a resonance when matched with the plasma period. This fit matched the data well, as is shown in figure 4.14b. At pressures above the resonant pressure, the plasma period is shorter than the pulse spacing; in this case adjacent pulses can excite wakefields spaced by more than one period, and can therefore still add in phase. At pressures below the resonant pressure, then, the plasma period is longer than the pulse separation; now two (or more) pulses can excite wakes separated by less than the plasma period. Finally, it is seen that the peak wakefield amplitude is around 0.9 $\pm$ 0.06 %, higher than the single pulse experiment which had a peak amplitude of 0.7 $\pm$ 0.07 %. The pulse energy for the single pulse case was 210 mJ but the energy of the pulse train was 300 mJ on target. This occurs because in the single pulse experiment the polarising beam splitters that were used to control the ASTRA beam's energy output were still in the beam line. After many data runs, in which it was difficult to detect the wakefield generated by the pulse train, and in order to give the best possibility to see a wakefield signal, these beam splitters were removed thus increasing the energy on target by around 30 %; this actually led to driving slightly more intense wakefields.

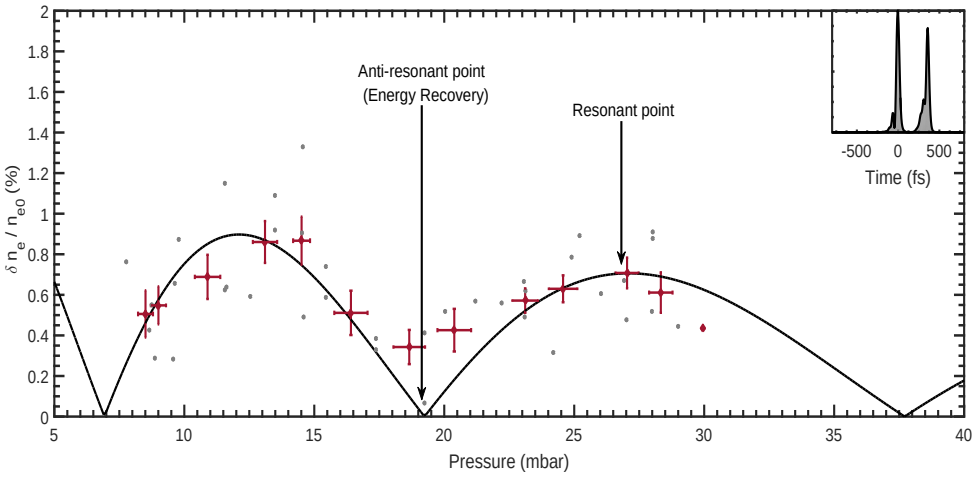
In figure 4.14b there is a discrepancy between the data and the theoretical ideal, though the trend of the data fits well to the theoretical ideal. The difference between the data and the theoretical ideal is because of the measured GDD, this has a relatively large margin of error and causes the data to be offset from the theoretical ideal.

The generation of the double pulse was achieved by first blocking one arm of the Michelson and using the SSA to optimally compress the pulse. The second arm of the Michelson was then unblocked and the separation between the two pulses was set to (400 ± 17) fs.

Figure 4.15a shows how the plasma period from the TESS analysis of the sub-sideband moved with the plasma period for the gas target fill pressure; this again fits very well against the theory line. Figure 4.15b shows the relative wake amplitude deduced from a TESS analysis as a function of the gas fill pressure by the double pulse set-up, where the theory fit is determined by equation 4.19, setting N to two. For a pulse separation of 360 fs the resonance pressure is ∼1.9 mbar but secondary resonances can be seen at 11 mbar and 25 mbar. These secondary resonances show the driving of a wakefield using two distinctly separate pulses that are combined in the plasma to drive a wakefield. What is even more interesting is that because two pulses were used, the anti-resonant points, where a wakefield is not measured, such as at 18 mbar, are actually caused by the wakefield generated by one pulse being damped by the second pulse.



(a)



(b)

Images courtesy of Chris Arran

Figure 4.15: Determination of the wakefield generated by the double pulse set-up seen in table 4.2. Figure 4.15a shows the measured the plasma period from the peak separation as a function of the expected plasma period for the cell pressure. The red circles are the data and the dashed black line is the theoretical ideal. Figure 4.15b shows the measured relative wake amplitude as a function of cell pressure. The red diamonds are the binned data, taken over pressure bins of 4 mbar, and the error bars are standard errors. The gray dots are the raw data, while the black dashed line represents the predicted wakefield amplitudes for this driving pulse as given by equation 4.18. The inset in the top right hand corner is a reconstruction of the temporal intensity profile of the driving pulse, as determined by the SSA measurement and the compressor settings.

4.4.3 Results of FDH Analysis

The author performed a full FDH analysis on the same data. Looking at the single pulse data set, a typical result is shown in figure 4.16. This clearly shows the plasma wave. The plasma period can be measured, which in this case averaged over four periods to be (126 ± 3.9) fs. This value can be compared against the plasma period which is expected for exciting a wakefield at a measured pressure of (18.22 ± 0.05) mbar which is 118 fs calculated from equation 4.17. To confirm this result, a different shot was examined at a pressure of (30.67 ± 0.08) mbar, measured to have a plasma period, averaged over four periods, of (88 ± 2.8) fs. This compares well against the theoretical plasma period, calculated from the measured pressure to be 91 fs. The changing plasma period with hydrogen gas

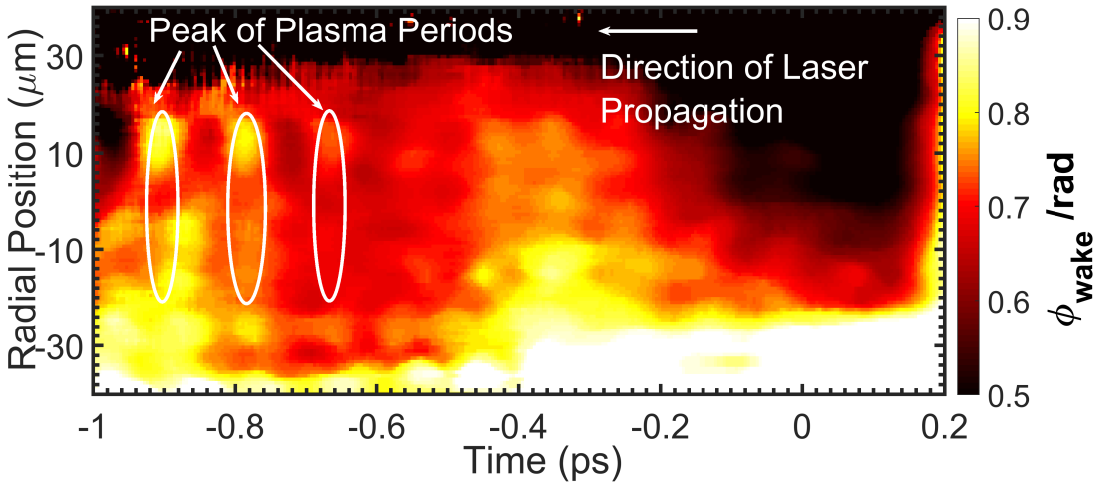


Figure 4.16: Reconstructed temporal phase of the wakefield generated using a single pulse. The data is a map of the density variation of the plasma, by looking at regions with high and lower variation in density the plasma period can be determined. On the left hand side of the image the peak in the plasma density has been highlighted. From an understanding of where these peaks are the plasma period can be found.

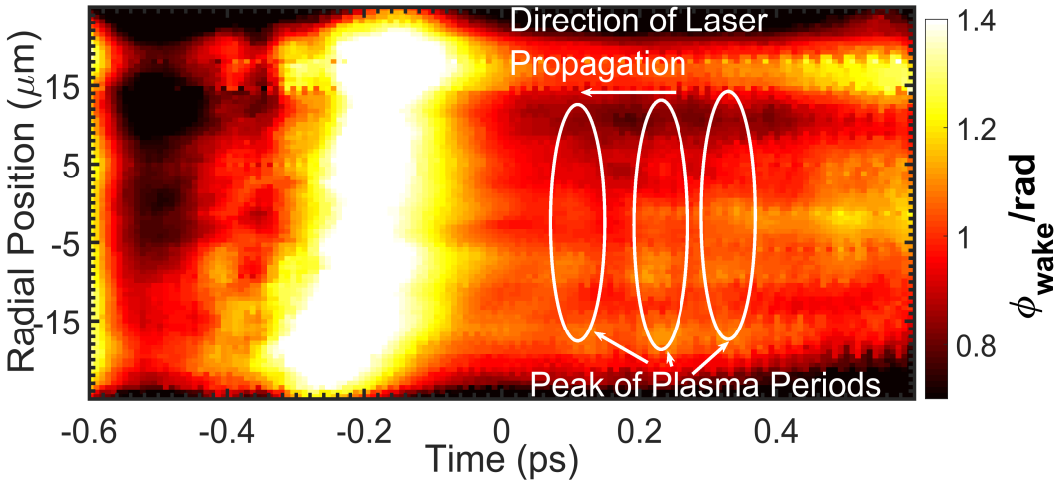


Figure 4.17: Reconstructed temporal phase of the wakefield generated using a pulse train.The data is a map of the density variation of the plasma, by looking at regions with high and lower variation in density the plasma period can be determined. On the right hand side of the image the peak in the plasma density has been highlighted. From an understanding of where these peaks are the plasma period can be found. On the left hand side is a white regional feature which is noise in the data.

pressure confirms that these oscillations are a measurement of a wakefield.

The same analysis technique was applied to the pulse train data. A typical example of the recovered phase map is shown in figure 4.17. In this data set it was much harder to recover the phase map and, as is shown in figure 4.17, only a small number of the plasma oscillations can be seen between 0 ps and 0.8 ps. The plasma period can be measured, by averaging over 3 plasma periods, and was found to be (132 $\pm$ 8.3) fs; this is compared to the measured pressure of (18.30 $\pm$ 0.05) mbar which gives a plasma period of 118 fs.

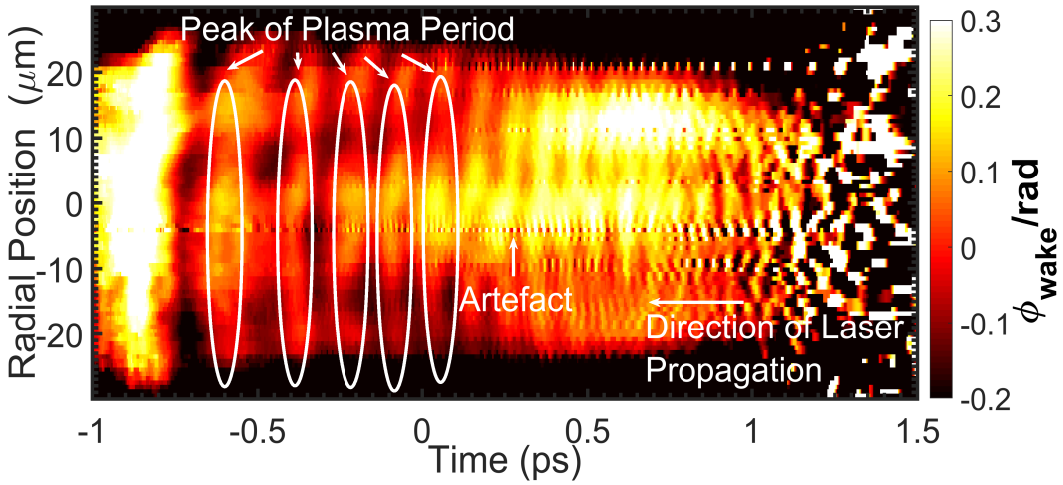


Figure 4.18: Reconstructed temporal phase of the wakefield generated using a double pulse. The data is a map of the density variation of the plasma, by looking at regions with high and lower variation in density the plasma period can be determined. This is seen particularly clearly for this data, the regions of high plasma density have been highlighted. There is some high frequency noise present in the data, an example has been labelled as an artefact.

The FDH analysis was then carried out on the wakefields generated using a double pulse. An example of the recovered phase map is shown in figure 4.18. The measured plasma period averaged over eight plasma periods was found to be (85.4 ± 1.3) fs compared to the predicted plasma period of 92 fs for a measured pressure of (29.86 ± 0.07) mbar. The recovered phase map clearly shows the plasma oscillation and so gives an insight into the structure of the wakefields that were generated.

Figure 4.19 of the double pulse is particularly interesting as it shows a distinct curvature of the wakefield with radial position. This is showing an edge effect of the wakefield structure, as the wakefield amplitude was larger near the laser axis, and hence the gamma of the oscillating electrons is greater; this means a

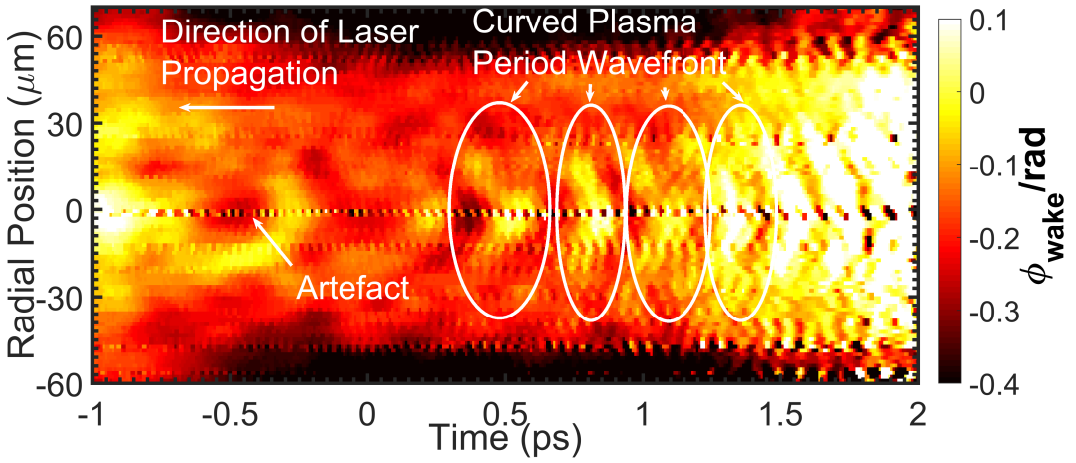


Figure 4.19: Reconstructed temporal phase of the wakefield generated using a double pulse. The data is a map of the density variation of the plasma, by looking at regions with high and lower variation in density the plasma period can be determined. There is a slight curvature in theses plasma periods, suggesting an edge effect.

relativistic increase in electron mass that causes the plasma period to be larger on-axis, resulting in a curved wave front. This is an extra piece of information that cannot otherwise be gained from the TESS analysis.

4.5 Conclusion

The ASTRA experiments demonstrate that plasma wakefields can be driven, and controlled, by trains of laser pulses. The pulse train method could be considered to be a generalisation of the beat-wave scheme, since the generation of multiple pulses was created by the superposition of two laser pulses of different local frequency. As far as the author is aware, the results presented here are the first demonstration of beat-wave excitation of a plasma wave with chirped laser pulses, as proposed by Deutsch *et al.* [70].

In the case of the double pulse regime, although using a low number of pulses to excite a wakefield, it can be considered to be a multi-pulse experiment as the method of generating the pulse train does not rely on the interference of the two pulses. This method also shows, for the first time, energy recovery from a wakefield. The energy is removed as laser photons (blue shift). However, no direct measurement of this effect was made. This work was published in Physical Review Letters and highlighted the achievement of energy recovery [71].

Both TESS and FDH have been used successfully to accurately measure very low amplitude wakefields. The use of TESS provided a conceptually simple way to diagnose a wakefield and determine the plasma frequency and the amplitude of this wakefield. The information gained assumes the wakefield to be sinusoidal; however, there are features such as the change of wavefront curvature with longitudinal position and the finite duration of the wake that cannot be assumed to be sinusoidal. Performing a full FDH analysis gives the amplitude of the wakefield as a function of time and in one transverse dimension. This was ultimately very useful, as an off line diagnostic of the wakefield to further develop understanding of how non sinusoidal features develop.

Chapter 5

Conclusion

In this final chapter, the work of all of the experiments is summarised in concluding statements and possible future work is explored.

5.1 Summary

In this thesis three main themes have been explored. The characterisation of plasma channels for use as a waveguide in chapter 2; the re-designing of the capillary waveguide housing and design of a gas cell in chapter 3; and the generation of pulse trains to be used in the driving of a wakefield, which was probed using frequency domain holography in chapter 4. The rest of this chapter will summarise the outcomes of each of these themes.

Chapter 2 focussed on understanding experimentally the formation of plasmas in capillary discharge waveguides to further understand how the initial starting condition affects the formation of the plasma channel and the guiding structure it creates. This was achieved with transverse interferometry using a Mach-Zehnder interferometer. Using this technique, a series of fringe patterns were recorded at different delays after the onset of the discharge current and analysed to show the

formation of a guiding channel with time. A baseline for comparison was established with a hydrogen-filled, square cross-section capillary of length 15 mm and sides of 200 µm; the driving circuit for this capillary was composed of a thyratron and capacitor. Each of the three elements of this capillary discharge waveguide (the gas, the driving circuit, and the capillary material) were changed to explore the effect this would have on the guiding channel and to give further insight into how improvements to this technique could be made.

Changing the discharge circuit from one based on thyratron to a Compact Marx Bank system was found to have many advantages over the previous system. These include a production of a smooth current profile and also provided a good guiding channel over a much longer time span of 200 ns, almost double that which was achieved before for these conditions. Changing the gas from hydrogen to helium showed very little difference from the baseline data in terms of the guiding channel produced but it is a much easier substance to handle. The sapphire channel was replaced with a diamond version, where thin diamond sheets of $15 \times 20 \times 0.5$ mm were added as an extra layer to the sapphire blocks and the sapphire spacer plates were replaced with diamond versions $9 \times 15 \times 0.3$ mm, forming a 15 mm long, 300 µm square capillary. While a direct measurement of the plasma channel formed was not possible owing to the poor quality fringes caused by the scattering of the probe beam on the diamond layers, the lifetime study showed encouraging evidence that the change of material would improve the capillary lifetime: after approximately 10 000 plasma discharges the surfaces of the diamond plates appeared to be unaffected. The same test carried out for the sapphire plate showed a removal of approximately 0.7 µm of material from the centre of the channel.

In chapter 3, modifications to the capillary discharge waveguide housing used in the Gemini 2014 experiment were reported. The outcomes of the experiment were not described in detail except to note that lessons learned on that experiment were applied to the capillary discharge waveguide housing. These lessons were the use of a gas target in parallel with a capillary waveguide; the acceptance of a very wide beam divergence; and improvements to help with the alignment of the capillary, relative to the laser axis and focus. The target was also modelled using the code OpenFOAM to understand the gas plumes that can have an effect on the interaction between the laser and the plasma guiding channel. This also gave an insight into the gas flow turbulence that needs to be avoided in the region between the capillary entrance and the gas feed. OpenFOAM was used to influence the experimental design of the ASTRA 2015 gas cell. By using OpenFOAM to model the gas cell, a minimisation of the effect of the gas plumes could be achieved. This was crucial, as density variations would affect the plasma period of the laser wakefield, making it impossible to use for a multi-pulse wakefield experiment. Fixing a flat density profile as a key parameter meant that other design considerations were then taken into account, such as target alignment and a quick method of changing the gas target length to change the laser interaction distance. This target was a key part of the successful ASTRA 2015 experiment.

Finally, chapter 4 described the generation of a pulse train used to excite a laser wakefield. This experiment successfully used both Temporarily Encoded Spectral Shifting(TESS) and Frequency Domain Holography (FDH) to diagnose the low amplitude wakefield generated. A Michelson set-up was used to generate the

pulse train in co-operation with the compressor. This set-up could be operated in two different ways: to either spectrally filter a stretched pulse to generate a pulse train or to generate two fully compressed (50 fs) pulses separated in time, referred to as, the double pulse regime. Using FDH/TESS, a measurement of the wakefield amplitude for a train of seven pulses was taken. A measurement of a wakefield amplitude was also taken for the double pulse set-up. The double pulse set-up also showed a demonstration of energy recovery, in which the first laser pulse was used to excite the wakefield and the second trailing pulse to dampen the wakefield. This is an important step for any high energy laser wakefield accelerator, observed here for the first time.

5.2 Future Improvements

Throughout this thesis a varied experimental programme has been undertaken to further understand and try to resolve some of the recurring issues experienced by the laser wakefield community. However, further experimental developments could be explored that would give greater insight in this field.

While the measurements taken in the interferometry lab were interesting, a lot of time was spent in the development of the analysis code and manually taking the data. Automating the collection of data would allow much quicker and more efficient collection of data runs. Further interferometric measurements of gas-filled capillary waveguides could be undertaken. Experiments on the electron density profile channel formation in hydrogen doped with noble gas-filled capillary discharges could be explored, as these are widely used in laser wakefield experiments with little understanding as to what effect the dopant has on the

electron density profile. The other major piece of work that could be explored is to combine some of these results, to see if a lower driving current can be used to create higher fraction ionisation plasma channel, by using the Compact Marx Bank in combination with helium gas, for example.

Improvements to the gas target or the capillary discharge waveguide housing are often driven by the experiment they are to be used in, therefore it is difficult to suggest practical improvements of the design that can be used more generally. However, one area that always needs to be carefully considered is trying to define the interaction point between the laser focus and the target. This is most easily achieved by imaging something on the target, such as a United States Air Force Resolution Grid, that is in a known position and using this knowledge to help find the laser focus to the target. A further consideration, is a method by which to align the gas target/capillary waveguide to the laser axis. This is not a trivial problem but requires a large amount of experimental time to resolve and so a robust solution to aligning the laser axis to the target is of great importance. An example method of how to do this would be to monitor the far-field pointing of the laser focus and the intensity of the laser, such that the target can be moved to optimise these parameters. Another method would be to define the laser axis to more than one point on the target and then use this information to reliably place the gas target/capillary waveguide on the laser axis.

The generation of a multi-pulse laser wakefield using the ASTRA laser was successful but in order to explore this idea further a higher energy beam would be required. This would allow for the excitation of a plasma wakefield using more

pulses, which would help to develop an understanding of how many pulses, and of what intensity could be used to drive a wakefield. Performing experiments which directly measure the energy recovery from the wakefield, would be an important step. This could be achieved by using a pair of orthogonally-polarized driving pulses so that they could be separated after the laser-plasma interaction. It would then be possible to look for changes in the energy and spectrum of the second driving pulse as the pulse separation (or plasma period) is varied. Finally, injecting electrons from an external source either by a conventional accelerator [72] or by a LWFA injector stage [73] into the wakefield structure and accelerating the electrons would be of interest to see if there are any unexpected consequences, such as ion motion, on the accelerated electron bunch.

Bibliography

[1] Thomas P. A. Ibbotson. *An investigation of laser-wakefield acceleration in the hydrogen-filled capillary discharge waveguide*. PhD thesis, Oriel College, University of Oxford, 2012. vi, 28, 34, 36

[2] Anthony J. Gonsalves. *Investigation of a hydrogen-filled capillary discharge waveguide for laser-driven plasma accelerators*. PhD thesis, Wolfson College, University of Oxford, 2006. vi, 17, 31, 33, 39, 40, 41, 42, 44, 46, 51

[3] A. W. Chao & W. Chou. Editorial Preface. Reviews of Accelerator Science and Technology. *Reviews of accelerator Ssience and technology*, 4, 2011. 1

[4] E. Tesemelis. Applications of accelerators. Graduate course Oxford University, October 2012. 1

[5] Wilhelm Konrad Ro. TECHNOLOGY. 103(9), 2015. 1

[6] George E. Smith. J. j. thomson and the electron: 1897–1899 an introduction. *The Chemical Educator*, 2(6):1–42, Dec 1997. 2

[7] W. Röntgen. über eine neue art von strahlen. *Physical-Medicine Society of Würzburg*, 64, 1895. 2

[8] W. C. Röntgen. Ueber eine neue art von strahlen. *Annalen der Physik*, 300(1):1–11, 1898. 2

[9] G. Ising. Arkiv for matekatik. 18, 1924. 2

[10] A. M. Sessler and E. J. N. Wilson. *Engines of Discovery: A Century of Particle Accelerators.* Ebook Central. Hackensack, NJ: World Scientific, 2007. 2

[11] Alexander Buck, Maria Nicolai, Karl Schmid, Chris M. S. Sears, Alexander Sävert, Julia M. Mikhailova, Ferenc Krausz, Malte C. Kaluza, and Laszlo Veisz. Real-time observation of laser-driven electron acceleration. *Nature Physics*, 7(7):543–548, 2011. 3

[12] T. Tajima and J. M. Dawson. Laser electron accelerator. *Physical Review Letters*, 43(4):267–270, jul 1979. 3, 4

[13] E. Esarey C. Schroeder & Leemans W. Physics of laser-driven plasma-based electron accelerators. *Reviews of Modern Physics*, 81:1229–1285, 2009. 3, 9, 11, 16

[14] M. Everett, A. Lal, D. Gordon, C. E. Clayton, K. A. Marsh, and C. Joshi. Trapped electron acceleration by a laser-driven relativistic plasma-wave. *Nature*, 368(6471):527–529, 1994. 4

[15] A. Dyson, A. E. Dangor, A. K. L. DymokeBradshaw, T. AshfarRad, P. Gibbon, A. R. Bell, C. N. Danson, C. B. Edwards, F. Amiranoff, G. Matthieusent, S. J. Karttunen, and R. R. E. Salomaa. Observations

of relativistic plasma waves excited by a 1.064 mu m and 1.053 mu m laser beat. *Plasma Physics and Controlled Fusion*, 38(4):505–525, 1996. 4

[16] F. Amiranoff, D. Bernard, B. Cros, F. Jacquet, G. Matthieussent, P. Miné, P. Mora, J. Morillo, F. Moulin, A. E. Specka, and C. Stenz. Electron acceleration in Nd-laser plasma beat-wave experiments. *Physical Review Letters*, 74(26):5220–5223, 1995. 4

[17] S. M. Hooker, R. Bartolini, S. P. D. Mangles, A. Tünnermann, L. Corner, J. Limpert, A. Seryi, and R. Walczak. Multi-pulse laser wakefield acceleration: a new route to efficient, high-repetition-rate plasma accelerators and high flux radiation sources. 234003. 4

[18] J. Daintith *et al.* *Oxford dictionary Of physics*. Oxford University Press, 5th edition, 2005. 5

[19] P. Gibbon. *Short pulse laser interactions with matter*. Imperial College Press, 1st edition, 2005. 6

[20] John M. Dawson. Nonlinear electron oscillations in a cold plasma. *Physical Review*, 113(2):383–387, 1959. 10

[21] F. F. Chen. *Inroduction to plasma physics and controlled fusion*. Plenum Press, 2nd edition, 1984. 10

[22] A. Heron G. Laval P. Mora, D. Pesme and N. Silvestre. Modulational Instability and Its Consequences for the Beat-Wave Accelerator. *Physical Review Letters*, 61(14):1611–1614, 1988. 10

[23] A. Pukhov & J. Meyer ter Vehn. Laser wakefield acceleration: the highly non-linear broken-wave regime. *Applied Physics B: Lasers and Optics*, 74, 2002. 11

[24] E. Esarey P. Sprangle J. Krall & A. Ting. Self-focusing and guiding of short laser pulses in ionizing gases and plasmas. *IEEE Journal of Quantum Electronics*, 33(11), 1997. 13

[25] W. Lu, M. Tzoufras, C. Joshi, F. Tsung, W. Mori, J. Vieira, R. Fonseca, and L. Silva. Generating multi-GeV electron bunches using single stage laser wakefield acceleration in a 3D nonlinear regime. *Physical Review Special Topics - Accelerators and Beams*, 10(6):061301, Jun 2007. 13

[26] D. F. Gordon, B. Hafizi, R. F. Hubbard, J. R. Peñano, P. Sprangle, and A. Ting. Asymmetric self-phase modulation and compression of short laser pulses in plasma channels. *Physical Review Letters*, 90(21):215001, 2003. 16

[27] S. Wilks, T. Katsouleas, J. M. Dawson, P. Chen, and J. J. Su. Beam loading in plasma waves. *IEEE Transactions on Plasma Science*, 15(2):210–217, 1987. 16

[28] S. Bajlekov. *Towards a Free-Electron Laser Driven by Electrons from a Laser-Wakefield Accelerator: Simulations and Bunch Diagnostics*. PhD thesis, Merton College, University of Oxford, 2011. 17, 19

[29] J. Lynch C. Durfree and H. Milchberg. Development of a plasma waveguide for high intensity laser pulses. *Physical Review E*, 51(3):2368–2387, 1995. 18

[30] P. Volfbeyn, E. Esarey, and W. P. Leemans. Guiding of laser pulses in plasma channels created by the ignitor-heater technique. *Physics Of Plasmas*, 6(5):2269–2277, 1998. 18

[31] C. G. R. Geddes, J. Van Tilborg, E. Esarey, C. B. Schroeder, D. Bruhwiler, C. Nieter, J. Cary, and W. P. Leemans. High-quality electron beams from a laser wakefield accelerator using plasma-channel guiding. 431(September), 2004. 18

[32] T. Kameshima, H. Kotaki, M. Kando, I. Daito, K. Kawase, Y. Fukuda, L. M. Chen, T. Homma, S. Kondo, T. Zh Esirkepov, N. A. Bobrova, P. V. Sasorov, and S. V. Bulanov. Laser pulse guiding and electron acceleration in the ablative capillary discharge plasma. *Physics of Plasmas*, 16(9), 2009. 18

[33] Rodolfo A. Bendoyro, Roxane I. Onofrei, João Sampaio, Rita Macedo, Gonçao Figueira, and Nelson C. Lopes. Plasma channels for electron accelerators using discharges in structured gas cells. *IEEE Transactions on Plasma Science*, 36(4 PART 4):1728–1733, 2008. 18

[34] Sergei Tochitsky and Manuel Hegelich. Summary report of working group 1: laser-plasma acceleration. *AIP Conference Proceedings*, 1507:231, 2012. 18

[35] D. J. Spence & S. M. Hooker. Investigation of a hydrogen plasma waveguide. *Physical Review E*, 63, 2001. 19

[36] A. Butler D. J. Spence & S. M. Hooker. Guiding of high-intensity laser pulses with a hydrogen-filled capillary discharge waveguide. *Physical Review Letters*, 89(18), 2002. 19, 22

[37] A. Gonsalves, T. Rowlands-Rees, B. Broks, J. van der Mullen, and S. Hooker. Transverse interferometry of a hydrogen-filled capillary discharge waveguide. *Physical Review Letters*, 98(2):025002, Jan 2007. 19

[38] A. Fridman & L. A. Kennedy. *Plasma physics and engineering*. CRC Press, 2nd edition, Feb 2011. 19, 20, 21

[39] S. Karsch. GeV-scale electron acceleration in a gas-filled capillary discharge waveguide. *New Journal Physics*, 9:415, 2007. 22

[40] T. P. A. Ibbotson, N. Bourgeois, T. P. Rowlands-Rees, L. S. Caballero, S. I. Bajlekov, P. A. Walker, S. Kneip, S. P D Mangles, S. R. Nagel, C. A. J. Palmer, N. Delerue, G. Doucas, D. Urner, O. Chekhlov, R. J. Clarke, E. Divall, K. Ertel, P. S. Foster, S. J. Hawkes, C. J. Hooker, B. Parry, P. P. Rajeev, M. J. V. Streeter, and S. M. Hooker. Laser-wakefield acceleration of electron beams in a low density plasma channel. *Physical Review Special Topics - Accelerators and Beams*, 13(3):8–11, 2010. 22

[41] B. H. P. Broks, K. Garloff, and J. J. A. M. van der Mullen. Nonlocal-thermal-equilibrium model of a pulsed capillary discharge waveguide. *Physical review. E, Statistical, nonlinear, and soft matter physics*, 71(1 Pt 2):016401, Jan 2005. 28, 47

[42] Mitsuo Takeda, Hideki Ina, and Seiji Kobayashi. Fourier-transform method of fringe-pattern analysis for computer-based topography and interferometry. *Journal of the Optical Society of America*, 72(1):156, jan 1982. 31, 32

[43] Richard M. Goldstein, Howard A. Zebker, and Charles L. Werner. Satellite radar interferometry: Two-dimensional phase unwrapping. *Radio Science*, 23(4):713–720, Jul 1988. 34

[44] Dennis C. Ghilglia and Mark D. Pritt. *Two-dimensional phase unwrapping. Theory, algorithums, and software.* John Wiley & sons, Inc., 1998. 34

[45] C. G. Durfee Iii, J. Lynch, and H. M. Milchberg. Mode properties of a plasma waveguide for intense laser pulses. *Optics Letters*, 19(23):1937–1939, 1994. 41

[46] A. E. Dyson, C. Thornton, and S. M. Hooker. A compact, low cost Marx bank for generating capillary discharge plasmas. *Review of Scientific Instruments*, pages 1–6, 2016. 53

[47] K. Kim, I. Alexeev, and H. Milchberg. Single-shot measurement of laser-induced double step ionization of helium. *Optics Express*, 10(26):1563–1572, 2002. 60

[48] K. Svensson, M. Hansson, F. Wojda, L. Senje, M. Burza, B. Aurand, G. Genoud, A. Persson, C.-G. Wahlström, and O. Lundh. Supersonic jets of hydrogen and helium for laser wakefield acceleration. *Physical Review Accelerators and Beams*, 19(5):051301, 2016. 61

[49] D. J. Spence, P. D. Burnett, and S. M. Hooker. Measurement of the electron-density profile in a discharge-ablated capillary waveguide. *Optics Letters*, 24(14):993–995, 1999. 64

[50] D. Spence and S. Hooker. Investigation of a hydrogen plasma waveguide. *Physical Review E*, 63(1):015401, dec 2000. 64

[51] S. M. Hooker, E. Brunetti, E. Esarey, J. G. Gallacher, C. G. R. Geddes, A. J. Gonsalves, D. A. Jaroszynski, C. Kamperidis, S. Kneip, K. Krushelnick, W. P. Leemans, S.P.D. Mangles, C. D. Murphy, B. Nagler, Z. Najmudin, K. Nakamura, P. A. Norreys, D. Panasenko, T. P. Rowlands-Rees, C. B. Schroeder, C. S. Toth, and R. Trines. GeV plasma accelerators driven in waveguides. *Plasma Physics and Controlled Fusion*, 49(12B):B403–B410, 2007. 64

[52] N. H. Matlis, A. J. Gonsalves, S. Steinke, J. Van Tilborg, E. H. Matlis, B. Shaw, D. E. Mittelberger, C. G R Geddes, and W. P. Leemans. Dynamics and density distributions in a capillary-discharge waveguide with an embedded supersonic jet. *Journal of Applied Physics*, 118(20), 2015. 64

[53] J. Daniels, J. van Tilborg, A. J. Gonsalves, C. B. Schroeder, C. Benedetti, E. Esarey, and W. P. Leemans. Plasma density diagnostic for capillary-discharge based plasma channels. *Physics of Plasmas*, 22(7):073112, 2015. 71

[54] Openfoam userguide version 2.2.1., June 2013. 72, 86, 87, 88

[55] Paul Andreas Walker. *Laser wakefield acceleration of electron to GeV energies and temporal laser pulse compression characterization in a capillary discharge waveguide*. PhD thesis, Merton College, University of Oxford, 2012. 73

[56] Jan-patrick Schwinkendorf. Sapphire capillaries for laser-driven wakefield acceleration in plasma. Master's thesis, Universitt Hamburg, 2012. 75

[57] Wolf Rittershofer. *Laser wakefield acceleration in tapered plasma channels. Theory, simulation and experiment.* PhD thesis, Merton College, University of Oxford, 2014. 85, 88, 90, 91

[58] Fang Yan. *Numerical Simulations of High Knudsen Number Gas Flows and Mi- crochannel Electrokinetic Liquid Flows.* PhD thesis, Drexel University, 2003. 86

[59] Luis F. Gutiérrez Marcantonia, José P. Tamagno, and Sergio A. Elaskar. High speed flow simulation using openFOAM. *Asociacion Argentina de Mecánica Computacional*, XXXI:2939–2959, 2012. 86

[60] *Fluid dynamics for physicsists.* Cambridge University Press, 1995. 87

[61] N. H. Matlis, S. Reed, S. S. Bulanov, V. Chvykov, G. Kalintchenko, T. Matsuoka, P. Rousseau, V. Yanovsky, A. Maksimchuk, S. Kalmykov, G. Shvets, and M. C. Downer. Snapshots of laser wakefields. *Nature Physics*, 2(11):749–753, 2006. 105, 125

[62] V. Yanovsky W. P. Leemans N. H. Matlis, A. Maksimchuk and M. C. Downer. Analysis of sinusoidally modulated chirped laser pulses by temporally encoded spectral shifting. pages 1–5, 2016. 105, 131

[63] T. Shuman, I. A. Walmsley, L. Waxer, M. Anderson, C. Iaconis, and J. Bromage. Real-time SPIDER: ultrashort pulse characterization at 20 Hz. *Optics Express*, 5(6):134–143, 1999. 110

[64] I.A. Walmsley and C. Dorrer. Characterization of ultrashort electromagnetic pulses. *Adv. Opt. Photon.*, 1:308–437, 2009. 112

[65] R. Trebino. *Frequency-resolved optical gating: The measurement of ultrashort laser pulses.* Kluwer Academic Publishers Group, Dordrecht, 2002. 113

[66] R. J. Shalloo, L. Corner, C. Arran, J. Cowley, G. Cheung, C. Thornton, R. Walczak, and S. M. Hooker. Generation of laser pulse trains for tests of multi-pulse laser wakefield acceleration. *Nuclear Instruments and Methods in Physics Research, Section A: Accelerators, Spectrometers, Detectors and Associated Equipment*, pages 1–3, 2015. 115, 116

[67] T. Robinson, K. O'Keeffe, M. Landreman, S. M. Hooker, M. Zepf, and B. Dromey. Simple technique for generating trains of ultrashort pulses. *Optics Letters*, 32(15):2203–2205, 2007. 115

[68] Simon Hooker and Colin Webb. *Laser Physics (Oxford Master Series in Physics).* Oxford University Press, USA, 210. 118

[69] S. Chen, M. Krishnan, A. Maksimchuk, and D. Umstadter. Acceleration of electrons in a self - modulated laser wakefield. *AIP Conference Proceedings*, 1(7):333–342, 1999. 140

[70] M. Deutsch, B. Meerson, and J. E. Golub. Strong plasma wave excitation by a 'chirped' laser beat wave. *Physics of Fluids B: Plasma Physics*, 3(7):1773, 1991. 150

[71] J. Cowley, C. Thornton, C. Arran, R. J. Shalloo, L. Corner, G. Cheung, C. D. Gregory, S. P. D. Mangles, N. H. Matlis, D. R. Symes, R. Walczak,

and S. M. Hooker. Excitation and control of plasma wakefields by multiple laser pulses. *Phys. Rev. Lett.*, 119:044802, Jul 2017. 151

[72] Benno Zeitler, Irene Dornmair, Tim Gehrke, Mikheil Titberidze, Andreas R. Maier, Bernhard Hidding, Klaus Flttmann, and Florian Grner. Merging conventional and laser wakefield accelerators. *Proc. SPIE*, 8779:877904–877904–7, 2013. 157

[73] K. Swanson, H. Tsai, S. Barber, R. Lehe, H. Mao, and S. Steinke. Electron Beam Control using Shock-Induced Density Downramp Injection. 040004, 2017. 157